

# Electromagnetic Response Design With Plasmonic Metamaterials

Author: Xueyuan Wu

Persistent link: <http://hdl.handle.net/2345/bc-ir:108293>

This work is posted on [eScholarship@BC](#),  
Boston College University Libraries.

---

Boston College Electronic Thesis or Dissertation, 2018

Copyright is held by the author, with all rights reserved, unless otherwise noted.

# ELECTROMAGNETIC RESPONSE DESIGN WITH PLASMONIC METAMATERIALS

Xueyuan Wu

A dissertation for PhD  
submitted to the Faculty of  
the department of Physics  
in partial fulfillment  
of the requirements for the degree of  
Doctor of Philosophy

Boston College  
Morrissey College of Arts and Sciences  
Graduate School

December 2018



# ELECTROMAGNETIC RESPONSE DESIGN WITH PLASMONIC METAMATERIALS

Xueyuan Wu

Advisor: Krzysztof Kempa, Ph.D.

## **Abstract**

Plasmons are quantized quasiparticles of the electron density waves. When coupled with photons, plasmons become another type of quasiparticles called plasmon polaritons. At the surface of a metal, surface plasmons can be formed. They have confined propagation on the surface, analogous to water waves in a pool. Plasmonic metamaterials manipulate the surface plasmon resonances, achieving a variety of unseen optical properties in nature. For the sake of fast emerging of nano fabrication and characterization techniques in recent years, plasmonic metamaterials have been applied in a wide range of fields, such as broadband absorption in solar cells, negative index materials for cloaking, subwavelength imaging, and wave modulations. One unique property of plasmonic metamaterial is offering remarkable flexibility in controlling effective dielectric properties of matter, depending on the composite design. In this thesis, several concepts of EM response manipulation using plasmonic metamaterials are proposed and studied. These studies include: (1) a scheme assuring topologically protected photonic edge states in the visible range utilizing epsilon-near-zero (ENZ) gyroelectric metamaterials; (2) engineering low frequency dielectric function with extremely subwavelength magnetic resonators; and (3) tailoring the electron-phonon interactions (including controlling superconductivity) by introducing plasmonic resonators into the phonon systems. These works may enable a broad range of applications in both photonic and phonon systems.

## **ACKNOWLEDGEMENTS**

It has been the most important period in my life. I personally feel that I have accomplished not only the PhD degree but the transition to become an adult. So many names appear in my mind who have supported and encouraged me. I cannot finish all of them in the page, but the gratitude will always keep in my heart.

First, my acknowledgment goes to my advisor Professor Kempa, without whose guidance, endless advices, passion to science and sense to the research topics, none of my research projects can be finished smoothly. I am particularly grateful to the help and support I have got from him when frustrations happened in the past years. I learned patience and persistency when facing those difficulties. I also benefit a lot from the personal interactions with Prof. Kempa who teaches me to be serious in science and easy-going in life.

I would also like to thank my committee members, Prof. Naughton, Prof. Broido and Prof. Bedell for beneficial discussions and suggestions not only in the process of finishing my thesis but also in the many cooperation in the past. I would especially like to thank prof. Naughton for the help in the experimental techniques and tons of support in those hard times in my life.

I would like to thank all my course teachers here at Boston College, including Prof. Bakshi, Prof. Karman, Prof. Uritam, Prof. Broido, and Prof. Ran. They helped me build the bases of my further study and research.

I would like to thank all the group members in the Kempa Group, Jiantao, Alex, Victoria and Tyler, with whom I have a lot of discussions and happy time to spend. I would like to thank all the graduate students and staffs who have shared my happiness during my time here.

Lastly I thank my parents and family members for their love, understanding and support during my PhD and throughout my life. In particular to my husband Dr. Fan Ye for his endless trust and encouragement. From him, I feel the unconditional support whenever life is in peace or tough. The warmth I got will always motivate me to move further in the future.

## TABLE OF CONTENTS

<b>Abstract</b> .....	<b>i</b>
<b>Acknowledgements</b> .....	<b>ii</b>
<b>Table of Contents</b> .....	<b>iv</b>
<b>List of Figures</b> .....	<b>vi</b>
<b>1.0 Introduction</b> .....	<b>1</b>
<b>1.1 Introduction to plasmonics and metamaterials</b> .....	<b>1</b>
<b>1.2 Basics of FDTD, FIT and FEM simulation methods</b> .....	<b>2</b>
<b>1.3 Retrieval of the effective dielectric function from the S-parameters</b> .....	<b>8</b>
<b>1.4 Summary and layout of this thesis</b> .....	<b>11</b>
<b>2.0 Topologically protected photonic edge states in the visible in plasmo-gyroelectric metamaterials</b> .....	<b>13</b>
<b>2.1 Background of photonic topological insulators</b> .....	<b>13</b>
2.1.1 Photonic counter part of integer quantum Hall effect .....	13
2.1.2 Photonic chiral materials mimicking quantum spin Hall effect.....	15
<b>2.2 Plasmo-gyroelectric metamaterials can stabilize topologically protected photonic band gap</b> .....	<b>16</b>
<b>2.3 Topologically nontrivial photonic band gaps of plasmo-gyroelectric metamaterials</b> .....	<b>21</b>
<b>2.4 Topologically protected photonic edge states in plasmo-gyroelectric metamaterials</b> .....	<b>25</b>
<b>2.5 Discussion and additional information</b> .....	<b>26</b>
2.5.1 Simulation of edge mode dispersion and propagation.....	27
2.5.2 Calculation of the Chern numbers .....	28
<b>3.0 Engineering low frequency dielectric function with metamaterial plasmonic structures</b> .....	<b>32</b>
<b>3.1 Introduction to high-k materials in TFT devices</b> .....	<b>32</b>
<b>3.2 Theory of effective permittivity with capacitive and inductive elements</b> .....	<b>32</b>
<b>3.3 Simulation results for structures with added inductive components</b> ..	<b>36</b>
<b>3.4 Optimized structure with mainly inductive components</b> .....	<b>43</b>
<b>3.5 Discussion</b> .....	<b>46</b>
<b>3.6 Summary</b> .....	<b>46</b>
<b>4.0 Engineering electron-phonon interaction with metamaterial plasmonic structures: reducing the electron-phonon scattering in semiconductors</b> .....	<b>49</b>

<b>4.1 Reducing the electron-phonon scattering in high mobility transistors.....</b>	<b>49</b>
4.1.1 Introduction.....	49
4.1.2 Electron-phonon interaction in semiconductors .....	51
4.1.3 Motivation for this work .....	51
<b>4.2 Effective dielectric function.....</b>	<b>52</b>
4.2.1 Effective dielectric function contribution from the plasmonic structure.....	52
4.2.2 FIT simulations of the plasmonic field screening .....	56
4.2.3 Extracting an effective dielectric response of plasmonic structures.....	59
<b>4.3 Carrier mobility calculations .....</b>	<b>60</b>
4.3.1 General formalism .....	60
4.3.2 Plasmonic mobility enhancement in GaAs and MoS <sub>2</sub> .....	61
<b>4.4 Summary .....</b>	<b>65</b>
<b>5.0 Summary .....</b>	<b>67</b>
<b>Appendix A. Topologically protected photonic edge states in the visible in plasmogyroelectric metamaterials (paper published) .....</b>	<b>68</b>
<b>Appendix B. Engineering low-frequency dielectric function with metamaterial plasmonic structures (paper published) .....</b>	<b>74</b>
<b>Appendix C. Tailoring the electron-phonon interaction with metallic plasmonic structures (manuscript under review) .....</b>	<b>80</b>
<b>Appendix D. Controlling superconductivity with plasmonic metamaterials.</b>	<b>103</b>
<b>D.1 Dielectric formulation of the BCS theory .....</b>	<b>103</b>
<b>D.2 Designing structures matching phonon spectra of BCS superconductors.</b>	<b>104</b>
D.2.1 MIM absorber structures for strong field enhancement.....	105
D.2.2 Babinet MIM structure designs.....	109
D.2.3 Experimental expectations .....	113
<b>Appendix E. Other EM response designs using plasmonic metamaterials.....</b>	<b>115</b>
<b>E.1 Realization of all optical states via electrical tuning of a two-element metasurface.....</b>	<b>115</b>
<b>E.2 Designed structures achieving 3-states modulation .....</b>	<b>117</b>
E.2.1 Modulation of responses of metasurfaces with varactor diodes.....	117
E.2.2 Structure of metasurfaces with varactor diodes and simulation results.....	118
E.2.3 Experimental results.....	124
<b>E.3 Discussion .....</b>	<b>127</b>
E.3.1 Extraction for effective impedance of the metasurface.....	127
E.3.2 Extraction for intrinsic LC properties of the metasurface.....	131
E.3.3 Two-state switch .....	132
<b>E.4 Conclusion.....</b>	<b>134</b>
<b>List of publications.....</b>	<b>136</b>

## LIST OF FIGURES

1-1 Yee's staggered grid for FDTD method.....	4
1-2 A two-port system defining the S-matrix .....	7
1-3 Retrieval of the effective dielectric function of an electric dipole and a magnetic dipole.....	10
2-1 Photonic topological insulator .....	19
2-2 PTI based on a square 2DPC immersed in a PGM.....	23
2-3 PTI based on a hexagonal 2DPC immersed in a PGM.....	24
2-4 Electric field amplitude of the excited edge mode when external magnetic field is off (zero off-diagonal terms).....	29
3-1 Schematics of the simple metamaterial .....	35
3-2 Spectra and corresponding effective dielectric function $\epsilon_{\text{eff}}$ for unit with spiral metallic insert.....	38
3-3 Comparing of metamaterial units and corresponding effective dielectric function....	39
3-4 Extremely low resonance frequency ( $\sim$ GHz) that coincides with device working frequency .....	41
3-5 Effect of spiral insert .....	42
3-6 Spiral structures for extremely low frequency, high-k applications.....	45
4-1 Envisioned structure and its dielectric response.....	54
4-2 The absolute amplitudes of the electric fields vs distance between the 2DEG and plasmonic metallic structure .....	58
4-3 Mobility enhancement in GaAs structure .....	62
4-4 Mobility enhancement in GaN structure.....	63
4-5 Mobility enhancement in MoS <sub>2</sub> structure .....	64

D-1 Design of an MIM plasmonic metamaterial structure with a well defined local resonance .....	107
D-2 MIM plasmonic metamaterial design matching the electron-phonon spectrum of Pb.....	108
D-3 Babinet MIM structure for matching Eliashberg spectrum of Pb.....	111
D-4 Babinet structure of thin connected frame .....	112
E-1 Design and fabrication of a tunable metasurface.....	121
E-2 Simulations and measurements of a 3-state “ART” tunable metasurface.....	122
E-3 Demonstration of achievement of all “ART” states at tuned voltage.....	123
E-4 Contour plot of the measured and simulated spectra of 3-state “ART” tunable metasurface .....	126
E-5 Effective permittivity and permeability extractions with spatial dispersion taken into account .....	129
E-6 Extracted permittivity, permeability and impedance when tuning applied voltage.....	130
E-7 Simulations of 2 two-states “ART” tunable metasurface.....	133

# Chapter 1. Introduction

## 1.1 Introduction to plasmonics and metamaterials

Plasmons are quantized quasiparticles of the electron density waves. These occur in plasmas in general, and in metals or doped semiconductors, in particular [1-3]. When coupled with photons, plasmons become another type of quasiparticles called plasmon polaritons. At the surface of a metal, or an interface between a metal and a dielectric, plasmons become surface plasmons, analogous to water waves in a pool. Thanks to the fast emerging fields of nano fabrication and characterization techniques in recent years, the field of plasmonics has been rapidly expanding.

Metamaterials are materials artificially engineered to have properties not found in nature [4-6]. Typically, these are extended periodic arrangements of various dielectric elements/structures, usually with these elements much smaller than the wavelength of the radiation employed, to assure the effective medium behavior. Properties of metamaterials derive from the structure of these elements and arrays, rather than from the properties of the materials employed. Even though the concept of metamaterials was introduced by Victor Veselago in 1968 [7], it was Sir John Pendry, who in 1999 was the first to propose a practical way to make metamaterials with an effective negative refractive index [8]. Typically, metamaterials should have large dielectric constant contrast between their elements, to ensure their proper functioning. Plasmonic metamaterials employ metal as a structure material, in combination with a dielectric. It is via the manipulation of surface plasmon resonances, that plasmonic metamaterials can achieve a variety of unseen optical properties in nature.

In this thesis, several concepts of EM response manipulation using plasmonic metamaterials are proposed and studied. These concepts include: a scheme which assures topologically protected photonic edge states in the visible range, engineering low frequency dielectric function, and tailoring the electron-phonon interactions (including controlling superconductivity). Due to inherent complexity, the quantitative understanding of the EM response of metamaterial plasmonic structures requires numerical methods. In the following section (1.2), we will introduce basics of numerical simulations methods used in this thesis. Based on the EM response obtained from simulations, an effective medium theory can be defined to represent a structure. This leads to an effective dielectric function of the plasmonic metamaterial. Section 1.3 presents an efficient scheme of retrieval of this effective dielectric function.

## **1.2 Basics of the FDTD, FIT and FEM simulation methods**

In this section, we present basics of the three simulation methods used in this thesis. The first is finite difference time domain (FDTD) scheme, a specialized numerical method for solving electromagnetic field problems. FDTD schemes for partial differential equations (PDE) solving, originate from early applications in the computational fluid dynamics in the 1920s [9]. In 1966 Yee proposed the staggered scheme, commonly used in most of the FDTD codes today [10]. In 1980s, Taflove coined the FDTD acronym [11]. Today, FDTD scheme is one of the most popular, with numerous codes commercially available. For a comprehensive review, see Ref. [12].

The FDTD method discretizes the Maxwell's curl PDEs in both space and time, following a staggered grid scheme proposed by Yee [10]. This scheme works as follows: in the space

domain, the electric and magnetic field components are displaced by half a unit cell, with directions orthogonal to each other, as shown in Figure 1-1; In the time domain, with the initial (at  $t = 0$ ) field values given, the magnetic field components at time  $t = i\Delta t$  ( $i = 1, 2, 3, \dots$ ) are obtained from the electric and magnetic field components at an earlier time  $t = (i-1)\Delta t$ . The electric field components at time  $t = (i+1)\Delta t$  are calculated based on the electric and magnetic field components at  $t = i\Delta t$ . The staggered calculation procedure is repeated until a steady-state solution is obtained. Yee's scheme gives a natural structural representation of the Maxwell's curl equations, and is well convergent.

Table 1-1. FDTD discretization of the space and time domains.

Maxwell's curl equations:	FDTD discretization:
$\nabla \times \mathbf{E} = -\frac{\partial \mathbf{B}}{\partial t}$	$\frac{\partial f}{\partial t} \approx \frac{f(t + \Delta t/2) - f(t - \Delta t/2)}{\Delta t}$
$\nabla \times \mathbf{H} = \mathbf{J}_f + \frac{\partial \mathbf{D}}{\partial t}$	$\frac{\partial f}{\partial x_i} \approx \frac{f(x_i + \Delta x_i/2) - f(x_i - \Delta x_i/2)}{\Delta x_i}, (x_i = x, y, z)$

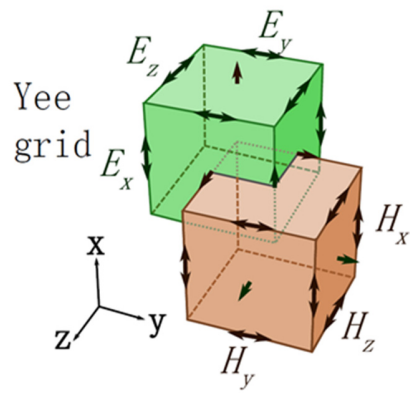


**Figure 1-1. Yee's staggered grid for FDTD method.** (Taken from: [https://en.wikipedia.org/wiki/Finite-difference\\_time-domain\\_method](https://en.wikipedia.org/wiki/Finite-difference_time-domain_method). Image source: By F Dominec – Own work, CC BY-SA 4.0)

A variation of the FDTD method is called the finite difference frequency domain (FDFD) method. FDFD keeps Yee's staggered grid scheme for spatial discretization, but solves the Fourier transformed Maxwell's equations in the frequency domain. Christ and Hartnagel presented an early version of the FDFD method in 1987 [13]. Since the FDFD method is in between the FDTD and finite element method, it is a less popular method nowadays.

The finite integration technique (FIT) scheme was proposed in 1977 by Thomas Weiland [14-15]. The discretization scheme of FIT is the same staggered grid in both space and time as the Yee's method, except that it uses integral form of the Maxwell's Equations, instead of the differential one. The advantage of the FIT method is its high flexibility in geometric modeling, and an ease in handling system boundaries. CST Microwave Studio [16] is a commercial simulation package based on FIT method. In most of the simulations done in this thesis, CST Microwave Studio is used.

The finite element method (FEM) approaches the PDE problem from an engineering point of view [17-19]. A complex system is intuitively divided (discretized) into a finite number of smaller space sub-domains that are called "elements". Each element is a simpler boundary value problem that obey the same PDE as the whole system. The boundary condition for each element is defined in such a way as to reflect the geometric relation between elements, and to satisfy the global boundary condition of the whole system. The solution of the whole system is obtained by assembling the solutions of all elements. The solution of an FEM is obtained by variational method (such as the Ritz-Galerkin method), or, in other words, following the least action principle. FEM originated from efforts of mechanical engineers to solve complex elastic continuum problems in aerospace engineering. Some pioneers include Hrennikoff and Courant, who in the early 1940s

introduced the “finite element” concept [17], and Argyris, Clough, Zienkiewicz in 1960s and 1970s [18-19], who developed the modern-day form of the method. The simulations in Chapter 2 are done using COMSOL Multiphysics [20], a commercial FEM package.



**Figure 1-2. A two-port system defining the S-matrix.**

### 1.3 Retrieval of the effective dielectric function from the S-parameters

Many popular codes provide solutions in terms of the S-parameters of the multi-port scattering theory. For a two-port system, the S-matrix is defined as follows

$$\begin{pmatrix} b_1 \\ b_2 \end{pmatrix} = \begin{pmatrix} S_{11} & S_{12} \\ S_{21} & S_{22} \end{pmatrix} \begin{pmatrix} a_1 \\ a_2 \end{pmatrix} \quad (1-1)$$

with  $a_i$  and  $b_i$  the incident and reflected complex wave amplitudes (“power waves”), respectively. Figure 1-2 shows schematic of a two-port system. In terms of the S-parameters, the reflection and transmission coefficients are  $S_{11}$  and  $S_{21}$ , respectively.

The core concept of the effective medium theory is that, if we replace a region with inhomogeneous internal structures by a properly chosen continuous homogeneous material filling the same region, we can achieve the exact same scattering properties (S-parameters). The macroscopic Maxwell’s equations are, in fact, the result of an effective medium theory. The electromagnetic parameters (i.e., permittivity and permeability functions) that define the constitutive relations of a material are indeed the effective medium parameters that fully describe the electromagnetic properties of that material. In this sense, the electromagnetic parameters retrieval method used in this work is merely an extension of the macroscopic Maxwell’s equations in the lower frequency region. Since both electromagnetic parameters (complex permittivity and permeability) and S-parameters (complex transmission and reflection coefficients) give a full description of a system, they are equivalent. Thus, there exists a rigorous way to obtain one set of parameters, given the other. The electromagnetic parameters retrieval method used in this thesis has been developed in several seminal works by Smith, et al. [21-23].

Assuming the effective material of thickness  $d$  can be described uniformly by the refractive index  $n$  and the impedance  $z$ , the analytic expressions relating  $n$  and  $z$  of this medium to its S parameters are as follows:

$$n = \frac{1}{kd} \cos^{-1} \left[ \frac{1}{2S_{21}} (1 - S_{11}^2 + S_{21}^2) \right] \quad (1-2)$$

$$z = \sqrt{\frac{(1+S_{11})^2 - S_{21}^2}{(1-S_{11})^2 - S_{21}^2}} \quad (1-3)$$

with  $n = \sqrt{\varepsilon\mu}$ ,  $z = \sqrt{\frac{\mu}{\varepsilon}}$ .  $\varepsilon$  and  $\mu$  are the effective permittivity and permeability of the medium. All these parameters are frequency dependent complex numbers. One example is illustrated in Figure 1-3, the retrieval results of electric dipole and magnetic dipole. A single unit cell of an electric resonator (a metal block) is shown in Figure 1-3a while a magnetic resonator (a metal ring) is in Figure1-3b. The retrieved permittivity for electric dipole (in Figure 1-3c) and permeability for magnetic dipole (in Figure 1-3d) confirm the expected Lorentz resonance of them respectively.

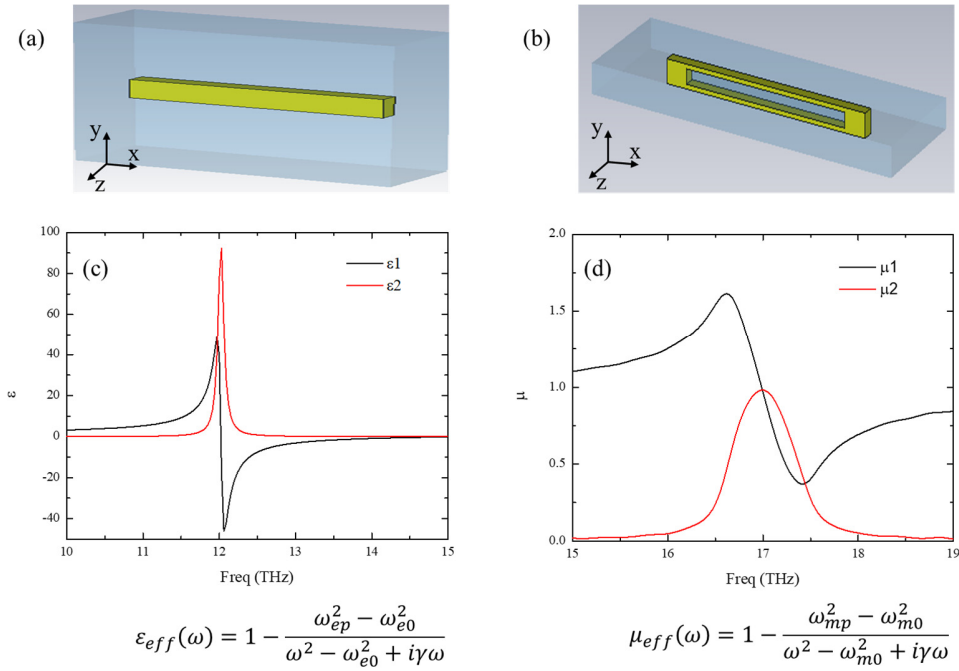


**Figure 1-3. Retrieval of the effective dielectric function of an electric dipole and a magnetic dipole.** (a) Schematic of a unit cell of an electric dipole with propagation direction into the plane (z direction). The structure is obtained by periodic extension of the unit in the x-y plane. (b) Schematic of a unit cell of a magnetic dipole with propagation direction in the x direction. The structure is obtained by periodic extension of the unit in the y-z plane. (c) The retrieved permittivity for the structure in (a) using the retrieval method described in Section 1.3. (d) The retrieved permeability for the structure in (b) using the same retrieval method as in (c).

#### **1.4 Summary and layout of this thesis**

In this chapter, we have introduced the basic concepts of plasmonic metamaterials, as well as several numerical methods (FDTD, FIT, and FEM) used in this thesis to study them. We have also introduced the electromagnetic parameters retrieval method from S-parameters by effective medium theory.

The layout of the remaining parts of this thesis is as follows. In Chapter 2, we show how plasmonic metamaterials can be integrated with gyroelectric materials to help achieve topologically protected photonic edge states in the visible range. In Chapter 3, we show how plasmonic metamaterials can be designed to engineer dielectric functions in the very low frequency regime. In Chapter 4, we study the possibility of controlling electron-phonon interactions with plasmonic metamaterials. In Appendices A, B, and C, we attach 3 of my first-author papers relating to Chapters 2, 3, and 4, respectively. In Appendix D, we give a brief introduction of the ongoing project of controlling superconductivity with plasmonic metamaterials. In Appendix E, we discuss other EM response designs using plasmonic metamaterials, with a special focus on the realization of all optical states via electrical tuning of a two-element metasurface.

## References:

- [1] W. L. Barnes, A. Dereux, T. W. Ebbesen, Surface plasmon subwavelength optics. *Nature* **424**, 824 (2003).
- [2] Z. Han, S. I. Bozhevolnyi, Radiation guiding with surface plasmon polariton. *Rep. Prog. Phys.* **76**, 016402 (2013).
- [3] R. H. Ritchie, Plasma losses by fast electrons in thin films. *Phys. Rev.* **106**, 874 (1957).
- [4] J. B. Pendry, A. J. Holden, D. J. Robbins, W. J. Stewart, Magnetism from conductors and enhanced nonlinear phenomena. *IEEE Trans. Microwave Theory Tech.* **47**, 2075 (1999).
- [5] D. R. Smith, W. J. Padilla, D. C. Vier, S. C. Nemat-Nasser, S. Schultz, Composite medium with simultaneously negative permeability and permittivity. *Phys. Rev. Lett.* **84**, 4184 (2000).
- [6] J. B. Pendry, D. Schurig, D. R. Smith, Controlling electromagnetic fields. *Science* **312**, 1780 (2006).
- [7] V. G. Veselago, The electrodynamics of substances with simultaneously negative values of  $\epsilon$  and  $\mu$ , *Sov. Phys. Usp.* **10**, 509 (1968).
- [8] J. B. Pendry, Negative refraction makes a perfect lens. *Phys. Rev. Lett.* **85**, 3966 (2000).
- [9] R. Courant, K. O. Friedrichs, H. Lewy, Über die partiellen Differenzgleichungen der mathematischen Physik, *Mathematische Annalen* (in German), **100**, 32 (1928).
- [10] K. Yee, Numerical solution of initial boundary value problems involving Maxwell's equations in isotropic media, *IEEE Transactions on Antennas and Propagation* **14**, 302 (1966).
- [11] T. G. Jurgens, A. Taflove, K. Umashankar, T. G. Moore, Finite-Difference Time-Domain Modeling of Curved Surfaces, *IEEE Transactions on antennas and propagation*, **14**, 4, (1992).
- [12] A. Taflove, S. C. Hagness, Computational electrodynamics the finite-difference time-domain method, U.S.A. Boston: Artech House (2005).
- [13] A. Christ, H. L. Hartnagel, Three-dimensional finite-difference method for the analysis of microwave-device embedding, *IEEE Transactions on microwave theory and techniques*, **35**, 8 (1987).
- [14] M. Clemens, T. Weiland, Discrete electromagnetism with the finite integration technique, *Progress in electromagnetics research*, **32**, 65 (2001).
- [15] T. Weiland, Finite integration method and discrete electromagnetism. In: Monk P., Carstensen C., Funken S., Hackbusch W., Hoppe R.H.W. (eds) Computational Electromagnetics. Lecture Notes in Computational Science and Engineering, vol 28. Germany Berlin: Springer, Heidelberg (2003).
- [16] <https://www.cst.com/>
- [17] R.V. Southwell, Relaxation methods in theoretical physics, 1<sup>st</sup> edition. U.K. Oxford: Clarendon Press (1946)
- [18] H. R.W. Clough, The finite element method in plane stress analysis. In Proc. 2nd ASCE Conf. on electronic computation (1960).
- [19] O. C. Zienkiewicz, K. Morgan, Finite element and approximation, Wiley (1983).
- [20] <https://www.comsol.com/>
- [21] D. R. Smith, D. C. Vier, Th. Koschny, C. M. Soukoulis, Electromagnetic parameter retrieval from inhomogeneous metamaterials, *Phys. Rev. E*, **71**, 036617 (2005).
- [22] D. R. Smith, Analytic expressions for the constitutive parameters of magnetoelectric metamaterials, *Phys. Rev. E*, **81**, 036605 (2010).
- [23] R. Liu, T. Cui, D. Huang, B. Zhao, D. R. Smith, Description and explanation of electromagnetic behaviors in artificial metamaterials based on effective medium theory, *Phys. Rev. E*, **76**, 026606 (2007).

## **Chapter 2. Topologically protected photonic edge states in the visible in plasmo-gyroelectric metamaterials**

### **2.1 Background of photonic topological insulators**

The results from this chapter have been published in Ref. [1]. Asymmetric propagation of light has been a field of great interest in recent years. Many works break the geometrical symmetry to alter coupling pathways between different photonic modes to generate asymmetric propagation of light traveling in opposite directions [2-4]. These works, however, cannot make optical isolators in the real sense, due to time-reversal symmetry remaining unbroken [5]. Non-reciprocal photonics, on the other hand, with time-reversal symmetry broken by external fields or internal interactions, promise the possibility of scattering-free and reflection-free one-way light propagation [6-11]. Among many non-reciprocal photonic systems, photonic topological insulators [10-13] have been proposed, and intensively studied in the past decade as the photonic counterpart of electronic topological insulators.

#### **2.1.1 Photonic counter part of integer quantum Hall effect**

The discovery of topological states in electronic systems started from the Integer Quantum Hall Effect (IQHE), where a 2D electron gas under low temperature and strong magnetic field yields quantized Hall conductance (integer multiples of  $e^2/h$ ) [14]. These integers are shown to be the Chern numbers (closely related to Berry's phase) associated with the topology of the electronic Hilbert space states. IQHE is thus successfully explained by Chern insulators (2D band insulators with nonvanishing Chern numbers) [15-16]. One key feature of the IQHE is the existence of topologically protected edge states that conduct in

one direction only, and are immune to back scattering. In 1988, Haldane pointed out that Landau-level quantization by the global magnetic field is not an essential requirement for IQHE, and that IQHE can be realized just with non-interacting Bloch electrons in a graphene (honeycomb) lattice with broken time-reversal symmetry [14]. This was an important step towards generalizing the electronic topological states to the photonic systems.

The first attempt to associate photonic crystals (PhCs) to electronic topological states was by Onoda et al in 2004, where they studied the Berry curvature in photonic crystals with broken spatial-inversion symmetry, and identified the “Hall effect of light” in that system [17]. Later, in 2008, Raghu and Haldane proposed the “analogs of quantum-Hall-effect edge states in photonic crystals”, by breaking the time-reversal symmetry of PhCs in a Faraday-effect (gyroelectric) media [15]. They pointed out that, although IQHE itself does not have photonic analog, as it follows from the Pauli principle of filling all one-particle states below the Fermi level, the existence of topologically protected edge states only relates to non-vanishing Chern number in a 2D Brillouin Zone, and can be generalized to Maxwell normal-mode eigenproblem in PhCs. They chose time averaged energy density of the electromagnetic radiation field as the Hamiltonian of the eigenproblem, and derived detailed ways to calculate Chern numbers in such a system, by integrating Berry connection over the path enclosing the 2D Brillouin Zone (or surface integral of Berry curvature over the entire Brillouin Zone surface). They pointed out that, only when time-reversal symmetry is broken, Chern numbers take non-zero values, that lead to topologically protected (one-way, scattering-free) edge states.

While Raghu and Haldane's proposal only focused on TE modes in PhC with a triangular lattice, as they were trying to reproduce the Dirac cone band structure for electrons in graphene, Wang et al pointed out in the same year (2008), that the existence of Dirac cone in the band structure is not a prerequisite for topologically protected edge states [18]. They showed that a degeneracy point lifted by time-reversal symmetry breaking can lead to non-zero Chern numbers, which ensures topologically protected edge states. By working with TM modes in a gyromagnetic PhC with square lattice, they also obtained reflection-free one-way edge modes.

### **2.1.2 Photonic chiral materials mimicking quantum spin Hall effect**

Haldane's graphene model of Chern insulators for IQHE intrinsically require broken of time-reversal symmetry (for non-vanishing Chern numbers). But it does not consider spin degree of freedom of electrons. Kane and Mele pointed out in 2005 that, if spin-orbital coupling is considered in Haldane's model, the resulting theory is simply two copies of the Haldane model with opposite signs of Hall conductance for up and down spins [19]. This does not violate time-reversal symmetry, since under electric field, electrons with up and down spins generate Hall currents that flow in opposite directions, resulting in zero Hall conductivity. However, spin Hall conductivity is now non-zero, and quantized. This is the Quantum Spin Hall Effect (QSHE). The QSH edge states have the important spin-momentum locking property that up spins propagate in one direction, while the down spins propagate in the other. This is drastically different from ordinary conductors, where both spins propagate in both directions. Ordinary conductors are fragile and susceptible to Anderson localizations, while QSH edge states cannot be scattered unless by time-reversal

symmetry breaking defects. QSHE thus describes time-reversal invariant two-dimensional insulators to host edge states with reflectionless propagation, without external magnetic field needed.

In 2015, Ma et al pointed out that, by fine tuning a triangular lattice of metal rods, TE and TM modes of the system can form doubly degenerate Dirac cones, which mimic the doubly degenerate Dirac cones in the Kane-Mele QSHE model [10]. They then open the gap by breaking inversion symmetry of the system, resembling the introduction of spin-orbital coupling to the Kane-Mele QSHE model. In such a PhC system, TE+TM and TE-TM modes resembles spin up and spin down state of an electron, respectively. They also demonstrated reflectionless propagation of TE+TM / TE-TM states at boundary.

In 2016, He et al showed a rigorous example of photonic topological insulator [11]. By using piezoelectric (PE) and piezomagnetic (PM) composites, they constructed a PhC with fermionic-like pseudo time-reversal symmetry. Instead of using TE+/-TM states, they used left/right circular polarization states (that have 90-degree phase difference between TE and TM modes) as the photonic counterparts of the spin up and down states of electrons. The broken time-reversal symmetry by the non-zero PE and PM terms serves as the spin-orbital coupling term in the Kane-Mele model. This is the first paper that obtained a fermionic-like time-reversal symmetry in a photonic system.

## **2.2 Plasmo-gyroelectric metamaterials can stabilize topologically protected photonic band gap**

Time reversal invariance (TRI) can be broken with gyromagnetic materials, but only at relatively low (microwave) frequencies. Gyroelectric materials, on the other hand, in the

presence of a magnetic field break TRI even at visible frequencies, albeit very weakly so (the ratio of the off-diagonal to diagonal (OTD) components of the dielectric permittivity tensor is only of the order of  $10^{-3}$ ) [20]. This results in very small gaps, making observation of the edge modes difficult. Nevertheless, a non-reciprocal lasing in topological cavities was recently demonstrated in a system which used the gyroelectric material yttrium iron garnet coupled to a multiple quantum well lasing cavity [21]. In this thesis, we propose a method to dramatically increase OTD tensor components in the gyroelectric systems: strong reduction of the diagonal components of the permittivity tensor, with a plasmo-gyroelectric metamaterial (PGM).

We first demonstrate, that it is the ratio of the OTD components of the permittivity tensor, not their absolute values, that controls the physics of TRI breaking in a PTI. For a nonmagnetic ( $\mu = 1$ ), source-free, nonconducting anisotropic medium with harmonic time dependence, Maxwell's equations reduce to

$$\nabla \times (\nabla \times E) = \frac{\omega^2}{c^2} \hat{\epsilon} E \quad (2-1)$$

where  $E$  is the electric field,  $c$  speed of light,  $\omega$  the mode frequency, and relative permittivity given by the tensor  $\hat{\epsilon} = \{\hat{\epsilon}_{ij}\}$  ( $i, j = x, y, z$ ). Clearly, by assuming that all tensor components are uniformly scaled, *i.e.*  $\hat{\epsilon} = \alpha \hat{\epsilon}'$ , where  $\alpha$  is a scaling constant, one can transform Equation 2-1 into an identical one, but with  $\hat{\epsilon}$  replaced with  $\hat{\epsilon}'$ , and  $\omega$  replaced with  $\omega\sqrt{\alpha}$ . Thus, the only consequence of such uniform scaling is the mode frequency change (renormalization). Then, only the ratios of the tensor components represent non-trivial physical effects, such as TRI breaking. Thus, increasing the off-diagonal components of the effective permittivity tensor, so that they are of the order of

the diagonal components, is equivalent to reducing the strength of the diagonal components relative to the off-diagonal components.

We propose here to achieve the desired suppression of the diagonal tensor components by employing a PGM structure made of a superlattice of alternating metallic and gyroelectric layers, with the response tuned to the near-zero diagonal tensor components condition. This composite structure will be used as a dielectric background of a 2D photonic crystal (2DPC) made of dielectric cylinders, as shown in Figure 2-1a. In the absence of magnetic field, this 2DPC will be designed to have photonic bands with degenerate points which, after application of a TRI-breaking external magnetic field, will open robust, topologically nontrivial gaps.

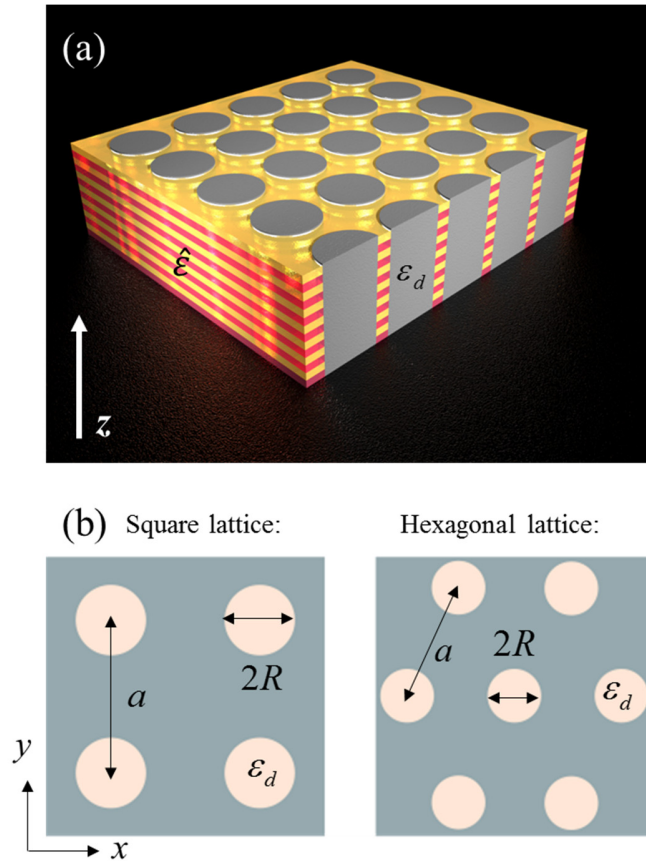


**Figure 2-1. Photonic topological insulator (PTI).** (a) the basic structure consists of a 2DPC made of dielectric rods, immersed in a metamaterial superlattice made of alternating metallic and gyroelectric films. Schematics of the unit cells of the square (b), and hexagonal (c) 2DPC. Taken from Ref. [1].

It has been shown [22] that the effective permittivity tensor components  $\epsilon_{ij}$  of the superlattice can be obtained from the tensor components of the constituent layers ( $i, j = x, y$ ):

$$\epsilon_{ij} = f_m \epsilon_{ij}^m + f_g \epsilon_{ij}^g, \quad (2-2)$$

$$\epsilon_{zz} = (f_m / \epsilon_{zz}^m + f_g / \epsilon_{zz}^g)^{-1}, \quad (2-3)$$

$$\epsilon_{xz} = \epsilon_{zx} = \epsilon_{yz} = \epsilon_{zy} = 0. \quad (2-4)$$

Here,  $m$  and  $g$  refer to the metal and gyroelectric layers and the  $f$ 's denote the thickness fill factors of the respective layers, which trivially obey the condition  $f_m + f_g = 1$ . For given  $\epsilon_{ij}^m$  and  $\epsilon_{ij}^g$ , one can choose  $f_m$  and  $\alpha$  to achieve a desired OTD ratio in the effective permittivity tensor. As an example, we use the following permittivity tensor for aluminum [23] (at operating frequency of  $\sim 2$  eV),

$$\hat{\epsilon}^m = \begin{bmatrix} -50 & 0 & 0 \\ 0 & -50 & 0 \\ 0 & 0 & -50 \end{bmatrix} \quad (2-5)$$

and the following tensor, for a gyroelectric layer made of  $\text{CuFe}_2\text{O}_4$ , operating at frequency of  $\sim 2$  eV and magnetic field given in [24],

$$\hat{\epsilon}^g = \begin{bmatrix} 4 & 0.01i & 0 \\ -0.01i & 4 & 0 \\ 0 & 0 & 4 \end{bmatrix} \quad (2-6)$$

We next parameterize Equations 2-2, 2-3, and 2-4 for materials (2-5) and (2-6) to engineer an OTD ratio of 5. By choosing  $f_m = 0.0741$  (which leads to  $f_g = 0.926$ ), the effective permittivity tensor of the composite superlattice in the presence of external magnetic field becomes:

$$\hat{\epsilon} = \begin{bmatrix} 0.001852 & 0.00926i & 0 \\ -0.00926i & 0.001852 & 0 \\ 0 & 0 & 4.347 \end{bmatrix} = \alpha \begin{bmatrix} 0.1 & \gamma i & 0 \\ -\gamma i & 0.1 & 0 \\ 0 & 0 & 234.71 \end{bmatrix}. \quad (2-7)$$

Here, the magnetic field strength is characterized by  $\gamma = 0.5$ , and the frequency renormalization scaling factor is  $\alpha = 0.01852$ . While the original gyroelectric OTD ratio in the presence of magnetic field was  $0.01/4 = 0.0025$ , for this PGM superlattice, it becomes 5 (note that in the absence of the magnetic field,  $\gamma = 0$ ). Note that the results in this work are independent of  $\epsilon_{zz}$ .

### 2.3 Topologically nontrivial photonic band gaps of plasmo-gyroelectric metamaterials

The next step is to use this effective medium with the permittivity tensor given by Equation 2-7 as a background dielectric for a 2DPC of dielectric cylinders, as shown in Figure 2-1a. We investigate two 2DPCs, based on a square (Figure 2-1b) and a hexagonal (Figure 2-1c) lattice of cylinders. We assume that the permittivity of the cylinders is  $\epsilon_d = 4$ . For the square lattice, the designed structure parameters (Figure 2-1b) are  $a = 1 \mu\text{m}$  and  $R = 0.45a$ . In the absence of external magnetic field, the band structure of the transverse electric (TE) modes for this 2DPC, calculated using COMSOL simulation software [25], is plotted in Figure 2-2a. Flat-band degeneracy occurs at the M point, and this can turn into a topologically non-trivial gap (as demonstrated by Wang et al [18]) when TRI is broken. This is achieved by turning on an external magnetic field, which activates the off-diagonal terms in the effective permittivity tensor (Equation 2-7). The resulting band structure

shown in Figure 2-2b demonstrates that a robust, absolute gap opens around the degeneracy point.

The topologically nontrivial bands are labeled in Figure 2-2b with the corresponding Chern numbers, calculated as follows. Due to the presence of electric anisotropy, we adopt the magnetic-field formulation of the Maxwell's equations [26]

$$\nabla \times (\hat{\epsilon}^{-1}(\mathbf{r}) \nabla \times \mathbf{H}) = \frac{\omega^2}{c^2} \mathbf{H} \quad (2-8)$$

With the following definition of the inner product  $\langle \mathbf{H}_1 | \mathbf{H}_2 \rangle = \int d^2r \mu_0 \mathbf{H}_1^* \cdot \mathbf{H}_2$ , the Chern number for the  $n$ -th band can be calculated from [18-19]

$$C_n = \frac{1}{2\pi} \int_{BZ} d^2k \left( \frac{\partial A_y^{nn}}{\partial k_x} - \frac{\partial A_x^{nn}}{\partial k_y} \right) = \frac{1}{2\pi} \oint_{BZ} d\mathbf{k} \cdot \mathbf{A}^{nn}, \quad (2-9)$$

where Berry connection  $\mathbf{A}^{nn}(\mathbf{k})$  is defined as [18-19]:

$$\mathbf{A}^{nn'}(\mathbf{k}) \equiv \frac{\langle \nabla_k \mathbf{H}_{n'} | \mathbf{H}_n \rangle - \langle \mathbf{H}_n | \nabla_k \mathbf{H}_{n'} \rangle}{2i \langle \mathbf{H}_n | \mathbf{H}_{n'} \rangle}. \quad (2-10)$$

A contour integral around the first Brillouin zone, or around an arbitrary contour surrounding the frequency degenerate points (some are indicated by red arrows in Figure 2-2a and Figure 2-3a) will give the corresponding Chern number. More calculation details are given in Section 2.5.

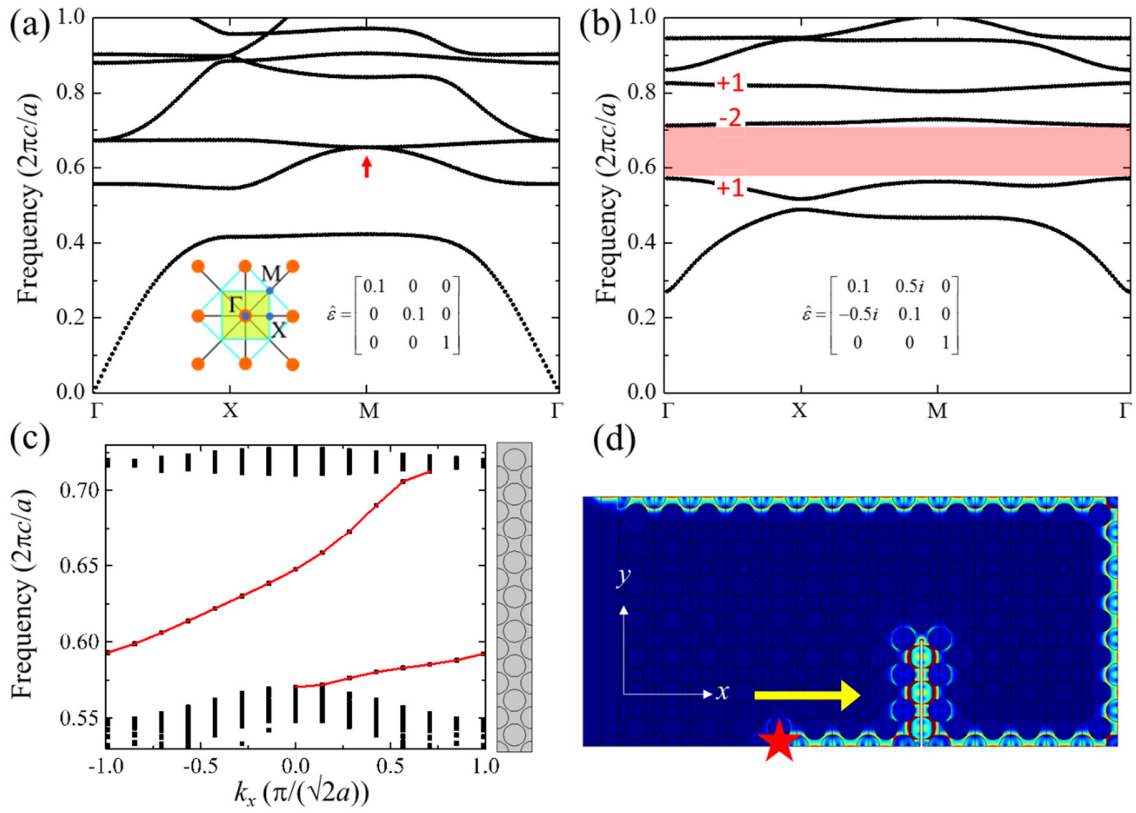


**Figure 2-2. PTI based on a square 2DPC immersed in a PGM.** Photonic band structure in the absence (a) and presence (b) of an external magnetic field. Corresponding Chern numbers are labeled on topologically non-trivial bands. Left inset in (a): fragment of the reciprocal lattice. Right insets in (a) and (b): dielectric permittivity tensor. (c) Edge mode dispersion (red line), and the bulk bands (black squares). Note, that the edge mode “peels off” the bulk states. (d) Electric field amplitude of the excited edge mode. The mode is excited with a point dipole (star), oscillating at the frequency of  $0.65 \, 2\pi c/a$ . The mode propagates only along the edge, and only in one (positive  $x$ ) direction. Backscattering is suppressed, even when encountering a large line obstacle made of a PEC boundary. The boundary on the left side is a perfectly matched layer; all other boundaries are PECs. Taken from Ref. [1].

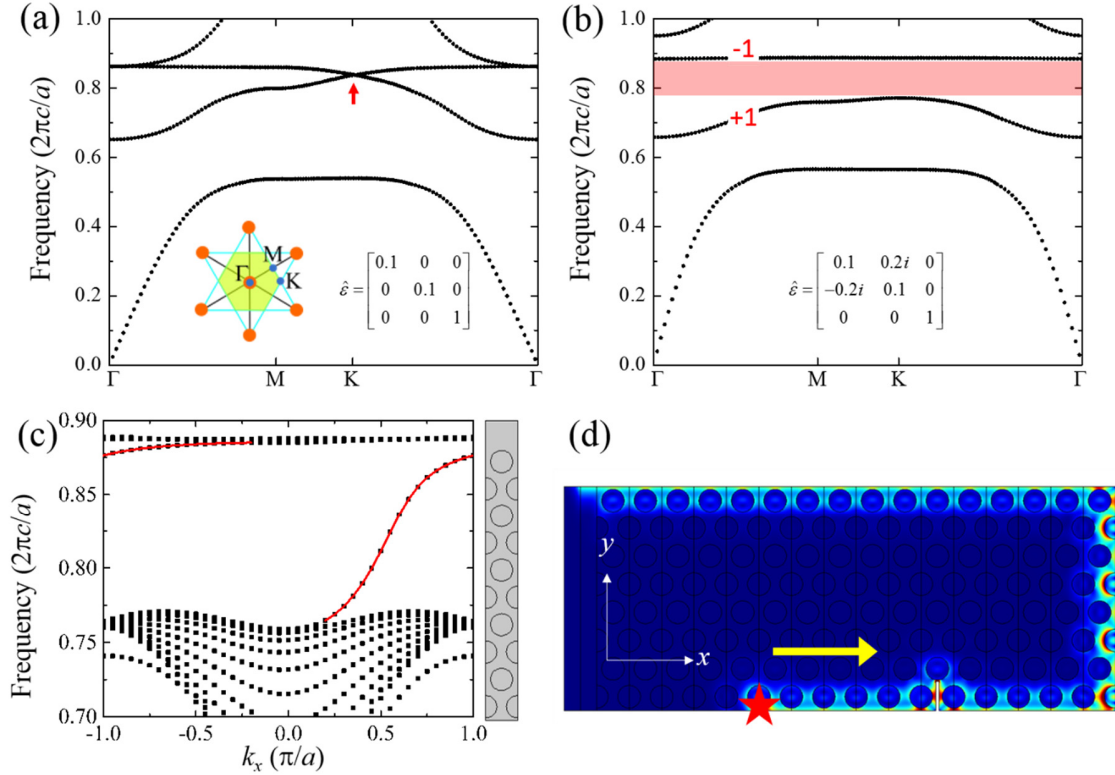


**Figure 2-3. PTI based on a hexagonal 2DPC immersed in a PGM.** Photonic band structure in the absence (a) and presence (b) of an external magnetic field, with corresponding dielectric permittivity tensors. Corresponding Chern numbers are labeled on topologically non-trivial bands. Left inset in (a): fragment of the reciprocal lattice. Right inset in (a) and (b): dielectric permittivity tensor. (c) Edge mode dispersion (red line), and the bulk bands (black squares). Note that the edge mode “peels off” the bulk states. (d) Electric field amplitude of an edge mode excited with a point dipole (star), oscillating at the frequency of  $0.85 \, 2\pi c/a$ . The mode propagates only along the edge, and only in one (positive  $x$ ) direction. Backscattering is suppressed, even when encountering a large line obstacle made of a PEC boundary. The boundary on the left side is a perfectly matched layer; all other boundaries are PECs. Taken from Ref. [1].

## 2.4 Topologically protected photonic edge states in plasmo-gyroelectric metamaterials

To show that this gap is topologically nontrivial, we truncate the 2DPC to create boundaries. The inset to the right of Figure 2-2c shows a top view of this truncated system unit cell: there are two boundaries of the structure, at top and bottom. The unit cell is periodically extended in the  $x$ - (horizontal) direction. Asymmetric, perfect electric conductor (PEC) configurations between the top and bottom boundaries are adopted to avoid duplication of the edge modes. As expected from the topological nature of the gap, an edge mode appears, which spans the gap. This mode has a positive slope (one direction of propagation). To show that the edge mode is protected against backscattering, we placed a point dipole source at the edge (marked as a star in Figure 2-2d), and excited it at the renormalized frequency  $\omega/(2\pi c/a) = 0.65$  (*i.e.* within the topological bandgap). In this case, we have added a boundary on the right edge of the window shown in Figure 2-2d. It is quite obvious that the mode propagates only along the edge, and only in one (positive) direction, and when encountering a large line obstacle made of a PEC boundary, no scattering or reflection of this mode occurs. Instead, the edge mode circumvents the obstacle to continue its net propagation in the positive  $x$ -direction.

An analogous effect occurs for a hexagonal 2DPC lattice, as suggested in Ref [14]. In this case, we chose  $a = 1 \mu\text{m}$  and  $R = 0.35a$ . The band structure for the TE modes without magnetic field is plotted in Figure 2-3a. A Dirac-like degeneracy occurs at the K point where, as for the square lattice under an external magnetic field ( $\varepsilon = 0.2$ ), a topologically non-trivial gap opens, Figure 2-3b. Chern numbers for the bands above and below the topologically non-trivial band gap are calculated to be +1 and -1, respectively, using the

above described method, in agreement with Ref [15]. This gap has a similar size to that in Figure 2-2b, even though a 2.5 times weaker magnetic field was applied. Figure 2-3c and d are analogs of Figure 2-2c and d, respectively. They demonstrate that this hexagonal 2DPC also supports an edge state, protected against backscattering.

Note that in both examples, at relatively small off-diagonal terms, due to the extensively reduced diagonal term value, a large gap size ( $\sim 10\%$ ) is achieved. This large gap size is robust against disorders, and prevents the topologically protected edge modes from radiative losses [18]. Although all calculations in the current work are done in non-dispersive scenarios, all conclusions can be readily extended to dispersive materials[13-15].

## **2.5 Conclusion and additional information**

In conclusion, we have demonstrated that two dimensional photonic crystals of dielectric microrods, immersed in a plasmogyroelectric metamaterial superlattice, can function as photonic topological insulators, supporting propagating edge states for which back scattering is suppressed. The PGM superlattice, which in the presence of an external magnetic field breaks time-reversal invariance, is designed to have a large ratio of off-diagonal to diagonal components of the dielectric permittivity tensor. This large ratio is obtained not by the conventional strategy of maximizing the off-diagonal components, but rather by suppressing the diagonal ones via the plasmonic (negative) response of the metallic films. Due to this large ratio, the band gaps are robust, even at optical frequencies. This work can pave the way for realization of topologically-protected edge states across a wide frequency range, including optical frequencies.

### **2.5.1 Simulation of edge mode dispersion and propagation**

Simulation configurations for edge mode dispersion diagram are plotted on the right insets of Figure 2-2c and 2-3c, respectively, for square and hcp periodicity scenarios. The top and bottom boundaries are both PEC; the left and right boundaries are periodic. Note that the arrangement of the lattice near the top and the bottom boundaries are deliberately chosen to be different to create asymmetric boundary modes to avoid the generation of duplicated boundary modes. Eigen-frequency solver is used in COMSOL to solve for mode near the selected frequency range. The frequency range is chosen to be near the nontrivial band gap of the corresponding PTI. Note that multiple (at least 5) unit cells should be chosen along the  $y$  direction for the existence of bulk modes. The more unit cells are chosen, the denser the bulk modes in Figure 2-2c and 2-3c will occur. But the number of unit cells repeated along  $y$  direction (as long as it is large enough) will not affect how the edge mode dispersion looks like.

To obtain the corresponding edge mode propagation simulation as shown in Figure 2-2d and 2-3d, a 2D array of the square (or hcp) unit cells are generated. This array is terminated in boundaries on top, bottom, and right sides with PEC conditions, and in boundary on left side with PML (perfectly matched layer) condition. The reason to leave the left-hand-side boundary open is to give a sink for the dipole point source, so as to avoid generation of local intensity singularities. The boundary termination details on the top, bottom and right sides can be different, as it will not affect the one-sided propagating edge mode. Obstacles are created on the bottom side on both Figure 2-2d and 2-3d. The details of the obstacles are again irrelevant, as it will not affect the one-way propagating edge mode. The dipole source is located at a place near the bottom boundary. Note that only when external field

is turned on (non-zero off-diagonal terms) EM waves propagate in a one-way scattering-free manner, as shown in Figure 2-2d and 2-3d. When external magnetic field is turned off (zero off-diagonal terms), the same dipole source generates EM waves that propagate in both directions, as shown in Figure 2-4.

### 2.5.2 Calculation of the Chern numbers

We follow the method in Ref. [18] to calculate the Berry connection:  $\mathbf{A}^{nn}(\mathbf{k})$ . We have exchanged all the following:  $\hat{\varepsilon} \Leftrightarrow \hat{\mu}$ ,  $\mathbf{E} \Leftrightarrow -\mathbf{H}$ , and swapped TE and TM modes in order to use the built-in Electromagnetic Waves, Frequency Domain (ewfd) COMSOL module. Then when calculating the contour integral of  $\mathbf{A}^{nn}(\mathbf{k})$ , we used the difference between field profiles simulated at  $\mathbf{k}$  and  $\mathbf{k}+d\mathbf{k}$  to obtain:  $\nabla_{\mathbf{k}}\mathbf{E}_n$ . We chose a circular path around M point for the calculation of Chern number for the 2<sup>nd</sup> band in Figure 2-2b. The -2 Chern number of the 3<sup>rd</sup> band in Figure 2-2b is composed of two contributions: one from M point, one from  $\Gamma$  point. The +1 Chern number of the 4<sup>th</sup> band comes from contribution at  $\Gamma$  point. Calculations for the hcp scenario are similar.

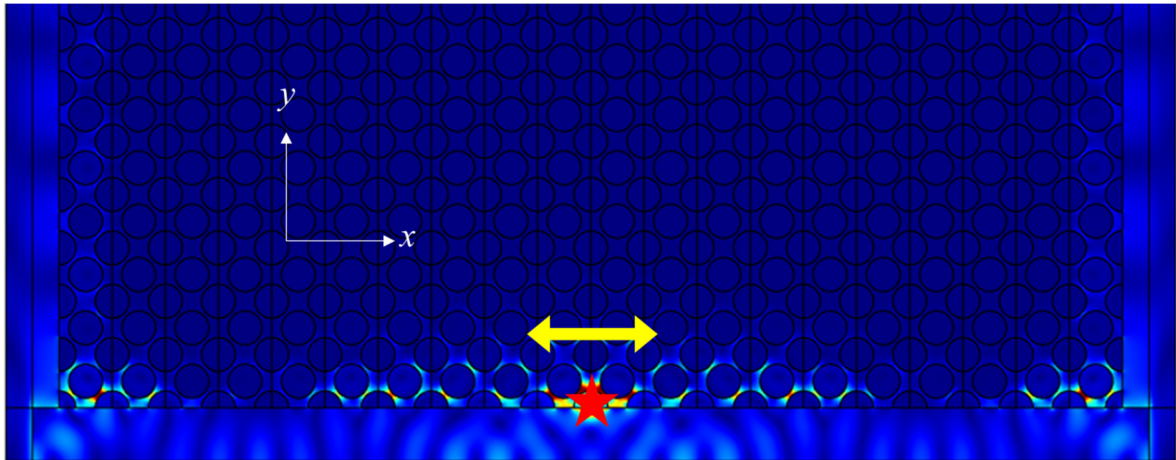


**Figure 2-4. Electric field amplitude of the excited edge mode when external magnetic field is off (zero off-diagonal terms).** The mode is excited with a point dipole (star), oscillating at the frequency of  $0.65 \ 2\pi c/a$ . The mode propagates along the edge, in both directions. The top and bottom boundary conditions are PEC, the left and right boundaries are both PML. Taken from Ref. [1].

## References:

- [1] X. Wu, F. Ye, J. M. Merlo, M. J. Naughton, and K. Kempa, Topologically Protected Photonic Edge States in the Visible in Plasmo-Gyroelectric Metamaterials, *Adv. Opt. Materials* **6**, 1800119 (2018).
- [2] V. A. Fedotov, P. L. Mladyonov, S. L. Prosvirnin, A. V. Rogacheva, Y. Chen, N. I. Zheludev, Asymmetric Propagation of Electromagnetic Waves through a Planar Chiral Structure, *Phys. Rev. Lett.* **97**, 167401 (2006).
- [3] C. Menzel, C. Helgert, C. Rockstuhl, E.-B. Kley, A. Tünnermann, T. Pertsch, F. Lederer, Asymmetric Transmission of Linearly Polarized Light at Optical Metamaterials, *Phys. Rev. Lett.* **104**, 253902 (2010).
- [4] F. Ye, M. J. Burns, M. J. Naughton, Symmetry-Broken Metamaterial Absorbers as Reflectionless Directional Couplers for Surface Plasmon Polaritons in the Visible Range, *Adv. Opt. Mater.* **2**, 957 (2014).
- [5] D. Jalas, A. Petrov, M. Eich, W. Freude, S. Fan, Z. Yu, R. Baets, M. Popović, A. Melloni, J. D. Joannopoulos, M. Vanwolleghem, C. R. Doerr, H. Renner, What is and what is not an optical isolator, *Nat. Photon.* **7**, 579 (2013).
- [6] Z. Wang, Y. Chong, J. D. Joannopoulos, M. Soljacic, Observation of unidirectional backscattering-immune topological electromagnetic states, *Nature* **461**, 772 (2009).
- [7] S. Manipatrani, J. T. Robinson, M. Lipson, Controlling the Carrier-Envelope Phase of Raman-Generated Periodic Waveforms, *Phys. Rev. Lett.* **102**, 213902 (2009).
- [8] H. Lira, Z. Yu, S. Fan, M. Lipson, Electrically Driven Nonreciprocity Induced by Interband Photonic Transition on a Silicon Chip, *Phys. Rev. Lett.* **109**, 033901 (2012).
- [9] A. R. Davoyan, A. M. Mahmoud, N. Engheta, Optical isolation with epsilon-near-zero metamaterials, *Opt. Express* **21**, 3279 (2013).
- [10] T. Ma, A. B. Khanikaev, S. H. Mousavi, G. Shvets, Guiding Electromagnetic Waves around Sharp Corners: Topologically Protected Photonic Transport in Metawaveguides, *Phys. Rev. Lett.* **114**, 127401 (2015).
- [11] C. He, X. Sun, X. Liu, M. Lu, Y. Chen, L. Feng, Y. He, Photonic topological insulator with broken time-reversal symmetry, *PNAS* **113**, 4924 (2016).
- [12] A. B. Khanikaev, G. Shvets, Two-dimensional topological photonics, *Nat. Photon* **11**, 763 (2017).
- [13] Y. Wu, C. Li, X. Hu, Y. Ao, Y. Zhao, Q. Gong, Applications of topological photonics in integrated photonic devices, *Adv. Optical Mater.* **5**, 1700357 (2017).
- [14] F. D. M. Haldane, Model for a quantum hall effect without landau levels: condensed-matter realization of the "parity anomaly", *Phys. Rev. Lett.* **61**, 2015 (1988).
- [15] F. D. M. Haldane, S. Raghu, Possible realization of directional optical waveguides in photonic crystals with broken time-reversal symmetry, *Phys. Rev. Lett.* **100**, 013904 (2008).
- [16] Y. Hatsugai, Chern number and edge states in the integer quantum Hall effect, *Phys. Rev. Lett.* **71**, 3697 (1993).
- [17] M. Onoda, S. Murakami, N. Nagaosa, Hall effect of light, *Phys. Rev. Lett.* **93**, 083901 (2004).
- [18] Z. Wang, Y. Chong, J. D. Joannopoulos, M. Soljacic, Reflection-free one-way edge modes in a gyromagnetic photonic crystal, *Phys. Rev. Lett.* **100**, 013905 (2008).
- [19] C. L. Kane, E. J. Mele, Quantum spin hall effect in graphene, *Phys. Rev. Lett.* **95**, 226801 (2005).
- [20] M. Zamani, M. Ghanaatshoar, Adjustable magneto-optical isolators with flat-top responses, *Opt. Express* **20**, 24524 (2012).
- [21] B. Bahari, A. Ndao, F. Vallini, A. E. Amili, Y. Fainman, B. Kanté, Nonreciprocal lasing in topological cavities of arbitrary geometries, *Science* **358**, 636 (2017).
- [22] D. J. Bergman, The dielectric constant of a composite material—A problem in classical physics, *Phys. Reports* **43**, 377 (1978).

- [23] M. A. Ordal, L. L. Long, R. J. Bell, S. E. Bell, R. R. Bell, R. W. Alexander, C. A. Ward, Optical properties of the metals Al, Co, Cu, Au, Fe, Pb, Ni, Pd, Pt, Ag, Ti, and W in the infrared and far infrared, *Applied Optics* **22**, 1099 (1983).
- [24] M. Veis, R. Antos, S. Visnovsky, P. D. Kulkarni, N. Venkataramani, S. Prasad, J. Mistrik, R. Krishnan, Complete permittivity tensor in sputtered cufe2o4 thin films at photon energies between 2 and 5 eV, *Materials* **6**, 4096 (2013).
- [25] COMSOL Multiphysics Modeling Software, <https://www.comsol.com>.
- [26] J.D. Joannopoulos, S.G. Johnson, J.N. Winn, R.D. Meade, *Photonic Crystals: Molding the flow of light* (2nd ed.), Princeton University Press, Princeton and Oxford (2008).

## **Chapter 3. Engineering low frequency dielectric function with metamaterial plasmonic structures**

### **3.1 Introduction to high-k materials in TFT devices**

The results from this chapter have been published in Ref. [1]. Making the thin film transistors (TFT) has been a widely established technology for the next generation of flat panel displays [2-6]. TFT is a field effect transistor (FET) [2], made of a stack of thin films, which include semiconductors, insulators and metallic contacts. Silicon dioxide ( $\text{SiO}_2$ ) has been commonly used as a gate oxide material. With decreasing device sizes, the thickness of the dielectric gate had to decrease to efficiently control the channel current via the capacitive coupling between the gate and the channel. Such thickness reduction, however, led to deleterious leakage currents, and so the increase of the dielectric constant (commonly called  $k$  in the engineering community, not  $\epsilon$ ) remained as an alternative; with large  $k$  the gate-channel capacitance increases, without increasing leakage. Hafnium oxide (HfO), with  $k = 25$ , has been proposed, and applied as the first-generation high- $k$  material [7-9]. The other promising materials in that class have been identified:  $\text{La}_2\text{O}_3$ , with  $k = 30$  [10-11], zirconium oxide, with  $k = 25$  [12-13], aluminum oxide, with  $k = 9$  [14-16], titanium dioxide, with  $k = 80$  [17-19], and  $\text{La}_2\text{Hf}_2\text{O}_7$ , with  $k = 30$  [20-21].

### **3.2 Theory of effective permittivity with capacitive and inductive elements**

The local dielectric function of a composite (of volume  $V_0$ ), made of metallic units (of volume  $V_m$ ), embedded in a dielectric matrix with dielectric constant  $\epsilon_\infty$ , is given in the long wavelength limit (LWL) by [22-23]:

$$\varepsilon(\omega, 0) \approx \varepsilon_\infty + \sum_{m=1}^M \frac{v_m \omega_p^2}{\omega_m^2 - \omega(\omega + i\gamma_m)}, \quad (3-1)$$

where  $v_m = V_m / V_0$ ,  $\omega_p = \sqrt{4\pi n e^2 / m}$ ,  $\omega_m$  is the renormalized unit resonance frequency of the corresponding order  $m$  and  $\gamma_m$  characterizes the damping of the composite medium. For vanishingly small frequency, Equation 3-1 yields

$$\varepsilon(0, 0) \approx \varepsilon_\infty + \omega_p^2 \sum_{m=1}^M \frac{v_m}{\omega_m^2} > \varepsilon_\infty. \quad (3-2)$$

Clearly, to maximize this composite dielectric function, a structure is needed with sufficiently small  $\omega_m$ , which can be achieved by metamaterial/plasmonic engineering. An important physical effect hidden in the universal Equation 3-1 is that each resonant (Lorentzian) term is a result of a capacitive-inductive coupled response. For example, below  $\omega_m$ , the response is first dominated by a capacitive character for frequencies much below the resonance ( $\omega \ll \omega_m$ ), but with increasing frequencies, the role of the inductive character increases, and dominates at the resonance. This can be illustrated by the following simple circuit analysis.

For a metallic resonator, the effective capacitance and inductance is denoted as:  $C$  and  $L$  respectively. Figure 3-1 shows schematic side views of two metamaterial capacitive units. Both units are defined by two horizontal electrodes (black solid bars) of width  $w'$  and length  $F$  in the  $z$ -direction. The blue color represents the dielectric filling. The unit shown in Figure 3-1a has a solid metallic insert (black square), and that in Figure 3-1b has an inductive metallic insert (spiral). Both inserts have the same outside dimensions  $h$ ,  $w$ , and  $l$  (in  $x$ ,  $y$  and  $z$  directions, respectively). We also assume that  $w' \approx w$ . Let  $C'$  be the capacitance of the unit in Figure 3-1a and assume that its inductance is negligible. The

reactance of the unit in Figure 3-1b is given approximately by  $X = -i \frac{1}{\omega C_{\text{eff}}} = i\omega L - i \frac{1}{\omega C'}$ ,

where  $C_{\text{eff}}$  is the effective capacitance of the unit in Figure 3-1b, and  $C' = C/2$  is the capacitance of the two (connected in a series), simple flat capacitors, defined by the gaps of size  $d$  above and below the inserts, in either unit.  $L$  is the inductance of the spiral metallic insert in the unit in Figure 3-1b. The unit in Figure 3-1b has the resonance frequency  $\omega_r = 1/\sqrt{LC'}$ , and therefore we get finally that the effective dielectric function  $\epsilon_{\text{eff}}$  of the effective medium made of the unit shown in Figure 3-1b, and periodically extended in  $y$  and  $z$  directions, is proportional to  $C_{\text{eff}}$  and therefore is given by

$$\epsilon_{\text{eff}} = \epsilon'_1 \frac{C_{\text{eff}}}{C'} = \frac{\epsilon'_1}{1 - (\omega/\omega_r)^2}, \quad (3-3)$$

where  $\epsilon'_1$  is the dielectric constant of the effective medium, made of the unit shown in Figure 3-1a, extended uniformly throughout  $y$ - $z$  space. The  $\epsilon_{\text{eff}}$  can be much larger than  $\epsilon'_1$ , and this effect is entirely due to the inductive contribution from the spiral metallic insert. It is also obvious that in the static limit ( $\omega \rightarrow 0$ ),  $\epsilon_{\text{eff}} = \epsilon'_1$ , and so the metamaterial dielectric function enhancement is possible only for nonzero frequencies. Conclusions of this simple circuit analysis hold in more rigorous treatments.

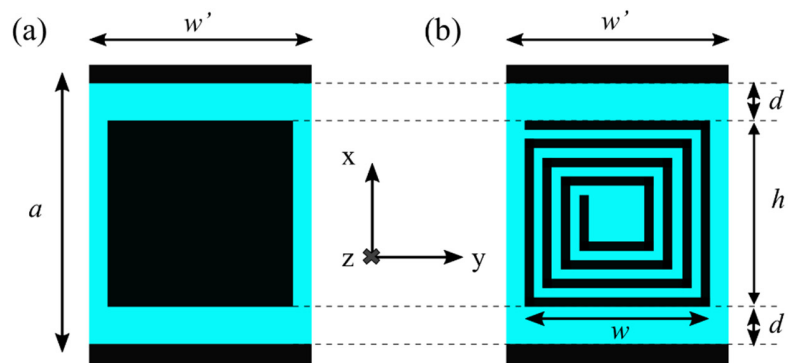


**Figure 3-1. Schematics of the simple metamaterial.** (a) Capacitor unit with solid metallic insert. (b) Unit with spiral metallic insert. Both units and inserts have the same outside dimensions, respectively. In the  $z$ -direction, both units have length  $F$ , and inserts length  $l$ . Taken from Ref. [1].

### 3.3 Simulation results for structures with added inductive components

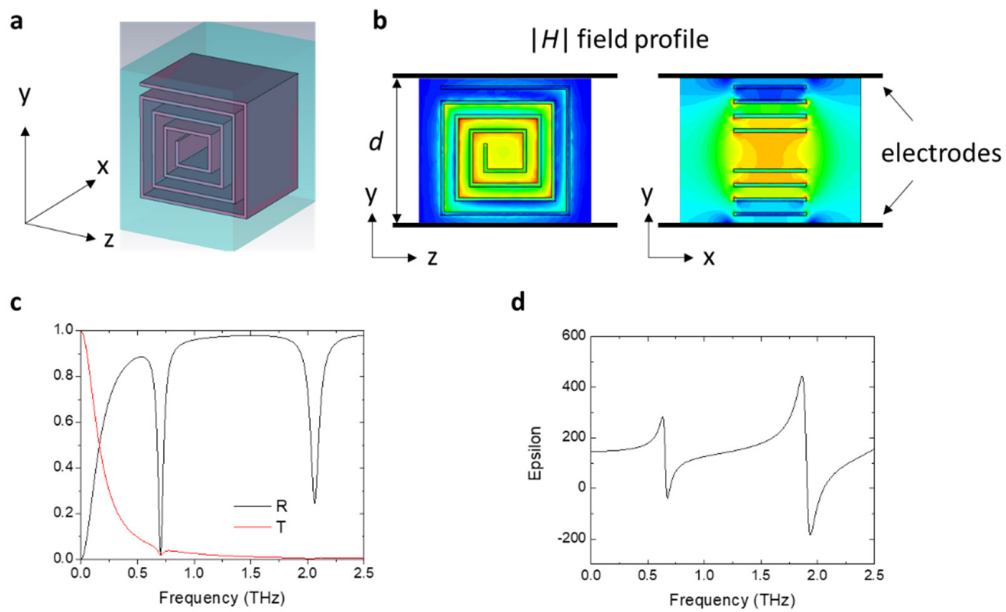
To demonstrate the above conclusion, we performed finite integration technique (FIT) simulations, using CST MW Studio software [24-25]. This numerically solves Maxwell's equations for a given distribution of local material parameters ( $\epsilon(\omega)$  and  $\mu(\omega)$ ) inside a given unit, at chosen grid points. Planar emission and absorption ports were defined at two opposing sides of a given unit, along the  $y$ -axis. The emitted source wave is linearly polarized, with the electric field directed along the  $x$ -axis, as required by, e.g., a TFT / high electron mobility transistor (HEMT) geometry. The FIT simulation provides the complex reflection and transmission coefficients  $r$  and  $t$  of an effective medium obtained by periodically extending (in the  $y$ - and  $z$ - directions) the chosen elementary units. Subsequently, we followed the method of reference [26-28] to extract  $\epsilon_{\text{eff}}$  and  $\mu_{\text{eff}}$  from  $r$  and  $t$ . This extraction method works best when the capacitor electrode separation  $a$  and unit cell width  $w'$  are much smaller than the wavelength of the radiation employed. This condition is satisfied for all structures used in this work.

Figure 3-2 is the result for a spiral structure as shown in Figure 3-1b. Dimensions were chosen to be  $a = 4 \mu\text{m}$  and  $d = 0.2 \mu\text{m}$ , and spirals were filled with Si ( $\epsilon = 12$ ), conforming again to the TFT/HEMT scenario. The number of turns in this example is set to be 4 with the metal thickness equals 50 nm. Figure 3-2c shows the em responses of the structure: reflectance ( $R$ ) and transmittance ( $T$ ) vs  $\omega$  in the frequency range from 0 to 3.5 THz. The  $\mathbf{H}$  field profiles (Figure 3-2b) at the resonance frequency prove that the magnetic oscillator is created by the spiral structures. The extracted effective dielectric function  $\epsilon_{\text{eff}}$  vs  $\omega$  for the effective medium structure is plotted in Figure 3-2d. The effective dielectric function

has a Lorentz form at 0.5 THz, corresponding to a wavelength of 600  $\mu\text{m}$ . The subwavelength ratio (wavelength/size) is as large as 150.

The above results are compared with the structures with the same unit cell, but smaller inductances. The red solid lines in Figure 3-3 show the extracted effective dielectric function  $\epsilon_{\text{eff}}$  vs  $\omega$  for an effective medium structure based on the above unit. The black line represents the case for a block with the same size as in Figure 3-1a. The blue line represents the result for a solid metallic insertion with identical metal volume to that of the spiral insert used to simulate the red solid lines, so that  $d = 1.5 \mu\text{m}$ . Multiple resonances are clearly visible, as predicted by Equation 3-1.

The curves in Figure 3-3c represent the enhancement of  $\epsilon_{\text{eff}}$  vs frequency. At the first resonance,  $\epsilon_{\text{eff}}$  strongly exceeds  $\epsilon'_1$  (by a factor of 2 for metallic insertion with the largest size and 20 for metallic insertion with the same metal filling), and for  $\omega \rightarrow 0$  the thick solid line and the red dashed lines converge ( $\epsilon_{\text{eff}} = \epsilon'_1$ ), in full agreement with Equation 3-3.



**Figure 3-2. Spectra and corresponding effective dielectric function  $\epsilon_{\text{eff}}$  for unit with spiral metallic insert.** (a) 3D perspective view of spiral structure. (b)  $\mathbf{H}$  field profiles from the front view and side view. (c) Reflectance (black solid curve) and transmittance (red solid curve) of the structure in THz. (d) Effective dielectric function  $\epsilon_{\text{eff}}$  vs. frequency  $\omega$ , for this effective media. Taken from Ref. [1].

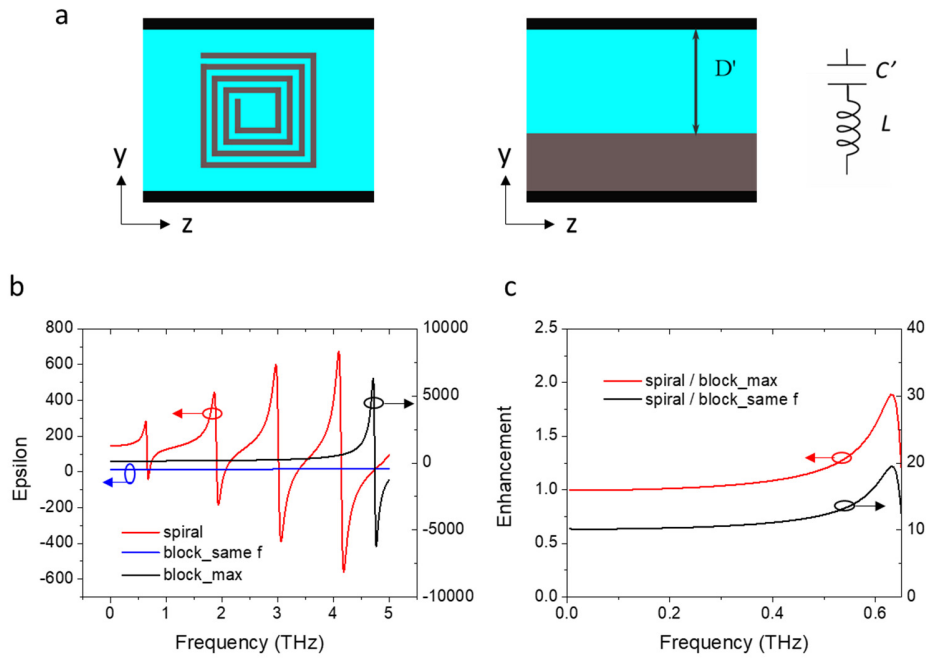


**Figure 3-3. Comparing of metamaterial units and corresponding effective dielectric function  $\epsilon_{\text{eff}}$ .** (a) Capacitor unit with spiral metallic insert. (b) Unit with solid metallic insert. Both units and inserts have the same outside dimensions, respectively. In the  $z$ -direction, both units have length  $F$ , and inserts length  $l$ . (c) Effective dielectric function  $\epsilon_{\text{eff}}$  vs. frequency  $\omega$ , for various simple effective media. Red solid line represents the real part of  $\epsilon_{\text{eff}}$  of the medium made of units shown in (a). The  $\text{Re}(\epsilon_{\text{eff}})$  of the medium made of units shown in (b) are represented by the black solid line. The blue solid line represents  $\text{Re}(\epsilon_{\text{eff}})$  for a medium made of units similar to (b), but with insert having the same volume as the volume of the spiral insert in (a). The enhancements of  $\epsilon_{\text{eff}}$  compared between the spiral structure and the block structure are plotted in (d). Taken from Ref. [1].

To benefit from the enhanced  $\epsilon_{\text{eff}}$ , one needs to engineer the resonance frequency  $\omega_r$  of the spiral inserts to be in the desired frequency range. Since we are guided here by the TFT/HEMT applications, we must lower this frequency to  $\omega_r/2\pi < 0.1$  THz (*i.e.* 100 GHz). A simple way to accomplish this frequency reduction, while still retaining the device dimension requirements, is to add more turns to the spiral insert. This is obviously subject to material and technological limitations. Another, more practical way is to “stretch” the spiral width  $w$  in the unit of Figure 3-1b, as shown in Figure 3-4a. Figure 3-4b is the reflection and transmission spectra of the square spiral. Figure 3-4c shows  $\epsilon_{\text{eff}}$  vs  $\omega$  extracted from the data in Figure 3-4b. Figure 3-5 studies the evolution of  $\text{Re}(\epsilon_{\text{eff}})$  vs  $\omega$  as a function of  $w$  (from 20  $\mu\text{m}$  to 60  $\mu\text{m}$ ) for such a structure. The corresponding color contour plot of the same dependence is shown in Figure 3-5c, and it demonstrates a linear dependence of resonance frequency  $\omega$  on  $1/w$ , in a large section of the plot (black dashed line). This linear dependence is expected from simple circuit model analysis: since both  $L$  and  $C'$  of the unit cell scale linearly with  $w$ , the resonance frequency  $\omega_r = 1/\sqrt{LC}$  must scale linearly with  $1/w$ . Note that there is no limit on the  $\omega_r$  reduction, and it can be made very small by simply increasing  $w$ . Guided by geometrical restrictions on typical TFT/HEMT devices, we have assumed  $w_{\text{max}} = 60$   $\mu\text{m}$ . Figure 3-5d to Figure 3-5f show the effect of changing  $l$ , the insert depth along the  $z$ -axis. Figure 3-5e shows the evolution of  $\text{Re}(\epsilon_{\text{eff}})$  as a function of  $l$ , with the corresponding color contour plot shown in Figure 3-5f. Clearly, while reducing  $l$  below  $l_{\text{max}} = 2$   $\mu\text{m}$  (full unit coverage in the  $z$ -direction) strongly affects the resonance strengths, the  $\omega_r$  dependence is slow.

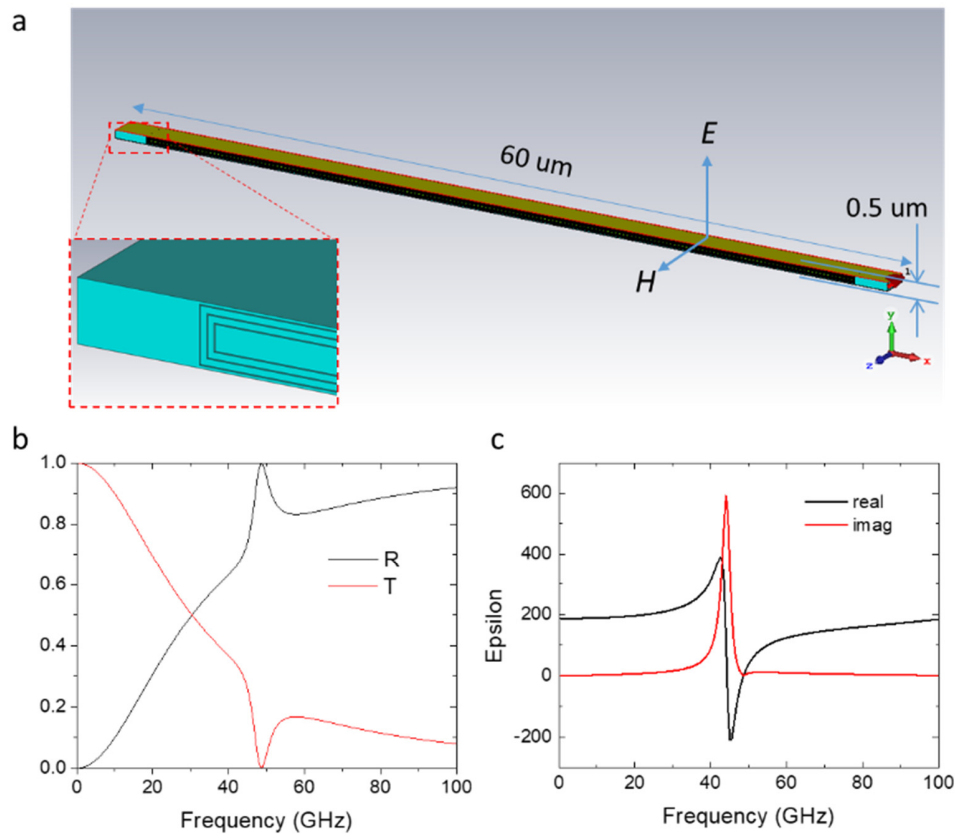


**Figure 3-4. Extremely low resonance frequency ( $\sim$ GHz) that coincides with device working frequency.** (a) dimension parameters of the squeezed structure. (b) Reflectance (black solid curve) and transmittance (red solid curve) of the structure in THz. (c) Effective dielectric function  $\epsilon_{\text{eff}}$  vs. frequency  $\omega$ , for this effective media. Taken from Ref. [1].

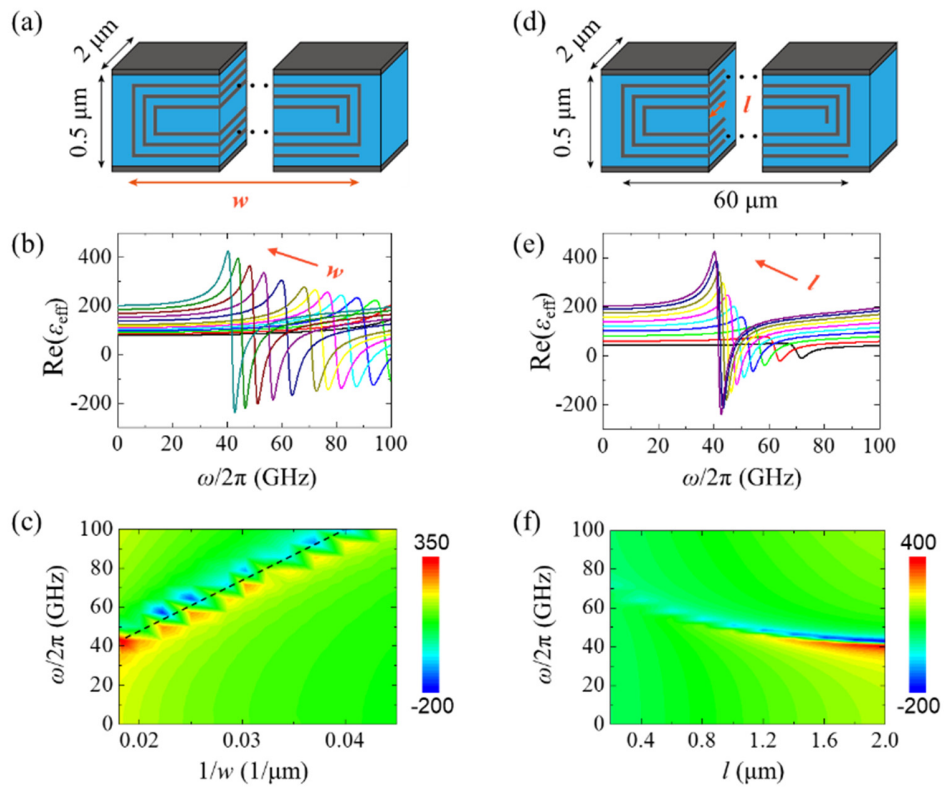


**Figure 3-5. Effect of spiral insert.** (a) Sketch of unit cell emphasizing the parameter  $w$ . (b) Evolution of  $\text{Re}(\epsilon_{\text{eff}})$  vs.  $\omega$  as a function of  $w$  (tuned from 20 to 60 μm). (c) Color contour plot of  $\text{Re}(\epsilon_{\text{eff}})$  vs.  $\omega$  and  $1/w$ . Dashed line is a guide to the eye. (d) Sketch of unit cell emphasizing the parameter  $l$ . (e) Evolution of  $\text{Re}(\epsilon_{\text{eff}})$  vs.  $\omega$  as a function of  $l$  (tuned from 0.2 to 2 μm). (f) Color contour plot of  $\text{Re}(\epsilon_{\text{eff}})$  vs.  $\omega$  and  $l$ . Taken from Ref. [1].

### 3.4 Optimized structure with mainly inductive components

An “optimized” structure, based on the above analysis, which takes into account some of the technological and material constraints, as well as dimensional restrictions of the TFT/HEMT structures, is sketched in Figure 3-6a. A unit of this structure has dimensions  $a = 0.5 \mu\text{m}$ ,  $w' = 62 \mu\text{m}$ ,  $F = 2 \mu\text{m}$ ,  $h = 0.45 \mu\text{m}$ ,  $w = 60 \mu\text{m}$ , and  $l = 1.9 \mu\text{m}$ . Figure 3-6b shows the spectrum of the extracted  $\epsilon_{\text{eff}}$  for this structure, which has  $\text{Re}(\epsilon_{\text{eff}}) > 180$  in the frequency range 0 to 40 GHz, with a practical maximum (with sufficiently small  $\text{Im}(\epsilon_{\text{eff}})$ ) as high as 390, at 40 GHz. The enhancement of  $\epsilon_{\text{eff}}$  above 190 is due to the inductive action of the spiral insert. Further enhancement of  $\epsilon_{\text{eff}}$  could be achieved, as discussed above by further increasing  $w$  (if allowed).

Since the enhancement in our structures is inductive, and as shown above quantitatively understandable with the simple circuit analysis, this suggest that further enhancement can be achieved by replacing the flat spiral insert in Figure 3-1b, with an elongated, multi-turn micro-solenoid as shown in Figure 3-6c. The inductance and capacitance of such a solenoid insert can be easily estimated (all parameters defined in Figure 3-1): the inductance is  $L \simeq \mu\mu_0\pi h^2 nN/4$ , with  $N$  the number of turns, and  $n = N/l$  the turn density. Similarly, the capacitance of the unit cell can be roughly estimated as  $C \simeq \epsilon\epsilon_0 w'F/2\bar{d}$ , where  $\bar{d} > d$  is the average (adjustable) electrode-insert distances, as defined in Figure 3-1. The resulting resonance frequency is given again by  $\omega_r = 1/\sqrt{LC} \sim 1/N$ . For example, with  $a = 0.5 \mu\text{m}$ ,  $w' = 0.5 \mu\text{m}$ ,  $h = 0.45 \mu\text{m}$ ,  $w = 0.45 \mu\text{m}$ ,  $l = 0.05N \mu\text{m}$  ( $N$  ranges from 12 to 40),  $F = l$ ,  $d = 25 \text{ nm}$ , a coil wire diameter of 20 nm, with  $\bar{d} = 65 \text{ nm}$ ,  $\epsilon = 12$  and  $\mu = 1$ , we obtain the red line in Figure 3-6d, which is in excellent agreement with the FIT simulations (shown as black square dots) for the physical situation. This excellent agreement allows us to predict

$\omega_r$  for much longer solenoid inserts. The inset in Figure 3-6d shows, that one can access the low GHz resonance frequency range with several thousands of solenoid turns, corresponding to  $F \simeq 100 \mu\text{m}$ . Realizations of such micro-solenoids with similar dimensions, and with metal or metal-dielectric wires, have been recently demonstrated using a focused ion beam deposition [29-31]. The composite spiral medium, with dielectric core shell nanohelix structures, provides one more degree of freedom to tune-up the dielectric function [31]. Then, based on Equation 3-1 and the corresponding theory [23], one could expect strong enhancement of  $\epsilon_{\text{eff}}$  for this composite medium.

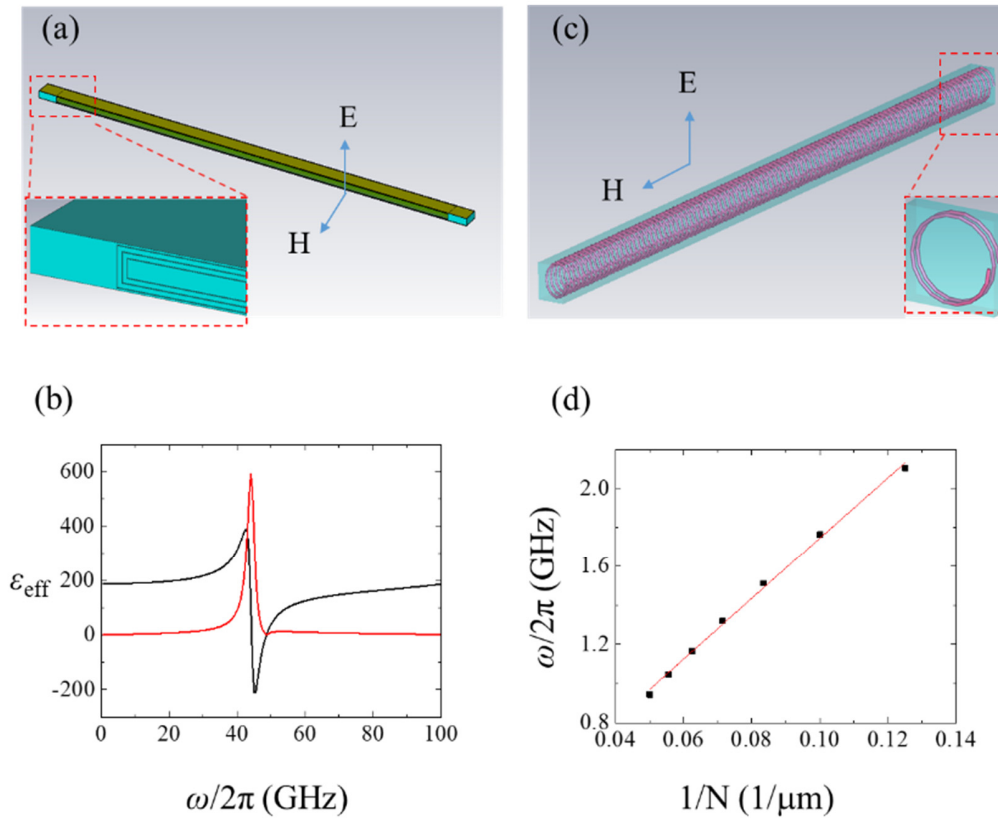


**Figure 3-6. Spiral structures for extremely low frequency, high-k applications.** (a) Schematic of a unit cell of a stretched rectangular spiral structure. The structure is obtained by periodic extension of the unit in the  $y$ - $z$  plane. (b) Corresponding dielectric function; black line for real, red line for imaginary parts of  $\epsilon_{\text{eff}}$ . (c) Schematic of a unit cell of a micro-solenoid structure, and (d) the corresponding plot of  $\omega_r$  vs.  $1/N$ . The squares are the FIT simulations, and the solid line is the result of the simple circuit analysis, with one adjustable parameter. The inset in (d) is a zoom-in of the low frequency regime, with both axes sharing the same units as the main figure. Taken from Ref. [1].

### 3.5 Discussion

The extreme reduction of the resonance frequency expected with the spiral structures opens up a new direction in  $\epsilon_{\text{eff}}$  enhancement. At such low frequencies, ferromagnetic/ferrite materials exist which could be used to further, significantly increase the medium inductance, and therefore  $\epsilon_{\text{eff}}$ . A new generation of high- $\mu$  materials [32,33]. could allow our scheme to yield effective high-k media with low-loss  $\epsilon_{\text{eff}}$  of many hundreds, in the low-frequency MHz range. Finally, we have confirmed that the choice of background dielectric material, as expected, does not affect the dielectric function enhancement due to the inductive inserts.

### 3.6 Summary

We have demonstrated engineering of a low frequency dielectric function with inductive metamaterial-plasmonic structures. To maximize the inductance, we focused on spiral microstructures in a strip, and solenoid configurations as inserts into units of the composite media. By employing FIT simulations, we have demonstrated that microstructures of our design can be used to make dielectric media with very large, low-loss, and low-frequency dielectric functions. The largest proposed unit insert is  $\sim 0.5 \mu\text{m}$  in height, and  $< 100 \mu\text{m}$  in length, and thus small enough for some high-k applications, such as TFT. Further improvements are possible with application of high- $\epsilon$  and high- $\mu$  materials; these could reduce the need for very long metallic inserts, and thus expand the parameter space for high-k applications.

## References:

- [1] X. Wu, M.J. Naughton, and K. Kempa, Engineering Low-Frequency Dielectric Function with Metamaterial Plasmonic Structures, *physica status solidi rrl* **12**, 1700291 (2018).
- [2] Y. Kuo, Thin Film Transistor Technology—Past, Present, and Future, *Electrochem. Soc. Interface* **22** [1], 55 (2013).
- [3] S. O. Kasap and J. A. Rowlands, Review X-ray photoconductors and stabilized a-Se for direct conversion digital flat-panel X-ray image-detectors, *J. Mater. Sci.: Mater. Electron.* **11**, 179 (2000).
- [4] J. P. Moy, Large area X-ray detectors based on amorphous silicon technology, *Thin Solid Films* **337**, 213 (1999).
- [5] Y. Kuo and H. Norminanda, Nonvolatile hydrogenated-amorphous-silicon thin-film-transistor memory devices, *Appl. Phys. Lett.* **89**, 173503 (2006).
- [6] P. Estrela and P. Migliorato, Chemical and biological sensors using polycrystalline silicon TFTs, *J. Mater. Chem.* **17**, 219 (2007).
- [7] B. H. Lee, L. Kang, R. Nieh, W. J. Qi, J. C. Lee, Thermal stability and electrical characteristics of ultrathin hafnium oxide gate dielectric reoxidized with rapid thermal annealing, *Appl. Phys. Lett.* **76**, 1926 (2000).
- [8] L. Kang; B. H. Lee, W. J. Qi, Y. Jeon, R. Nieh, S. Gopalan, K. Onishi, J. C. Lee, Electrical characteristics of highly reliable ultrathin hafnium oxide gate dielectric, *IEEE Electron Device Lett.* **21**, 4 (2000).
- [9] W. J. Zhu, T. P. Ma, T. Tamagawa, J. Kim, Y. Di, Current transport in metal/hafnium oxide/silicon structure, *IEEE Electron Device Lett.* **23**, 2 (2002).
- [10] S. Lim, S. Kriventsov, T. N. Jackson, J. H. Haeni, D. G. Schlom, Dielectric functions and optical bandgaps of high-K dielectrics for metal-oxide-semiconductor field-effect transistors by far ultraviolet spectroscopic ellipsometry, *Joul. Appl. Phys.* **91**, 4500 (2002).
- [11] T. Gougousi, M. J. Kelly, D. B. Terry, G. N. Parsons, Properties of La-silicate high-K dielectric films formed by oxidation of La on silicon, *Joul. Appl. Phys.* **93**, 1691 (2003).
- [12] D. Lee, H. Choi, H. Sim, D. Choi, H. Hwang, M. J. Lee, S. A. Seo, I. K. Yoo, Resistance switching of the nonstoichiometric zirconium oxide for nonvolatile memory applications, *IEEE Electron Device Lett.* **26**, 10 (2005).
- [13] J. H. Park, Y. B. Yoo, K. H. Lee, W. S. Jang, J. Y. Oh, S. S. Chae, H. K. Baik, Low-Temperature, High-Performance Solution-Processed Thin-Film Transistors with Peroxo-Zirconium Oxide Dielectric, *ACS Appl. Mater. Interfaces*, **5**, 410 (2013).
- [14] C. Avisa, J. Jang, High-performance solution processed oxide TFT with aluminum oxide gate dielectric fabricated by a sol-gel method, *J. Mater. Chem.*, **21**, 10649 (2011).
- [15] B. S. Lim, A. Rahtu, P. d. Rouffignac, R. G. Gordon, Atomic layer deposition of lanthanum aluminum oxide nano-laminates for electrical applications, *Appl. Phys. Lett.* **84**, 3957 (2004).
- [16] J. Kolodzey, E. A. Chowdhury, T. N. Adam, G. Qui, I. Rau, J. O. Olowolafe, J. S. Suehle, Y. Chen, Electrical conduction and dielectric breakdown in aluminum oxide insulators on silicon, *IEEE Transactions on Electron Devices*, **47**, 1 (2000).
- [17] S. A. Campbell, H. S. Kim, D. C. Gilmer, B. He, T. Ma, W. L. Gladfelter, Titanium dioxide (TiO<sub>2</sub>)-based gate insulators, *IBM Journal of Research and Development*, **43**, 3 (1999).
- [18] F. Carpi; D. D. Rossi, Improvement of electromechanical actuating performances of a silicone dielectric elastomer by dispersion of titanium dioxide powder, *IEEE Transactions on Dielectrics and Electrical Insulation* **12**, 4 (2005).
- [19] J. Qiu, L. Lan, H. Zhang, M. Gu, Effect of titanium dioxide on microwave absorption properties of barium ferrite, *Journal of Alloys and Compounds*, **453**, 261 (2008).
- [20] X. Cheng, Z. Qi, G. Zhang, Y. Chen, T. Li, G. Pan, M. Yin, The interface reaction of high-k La<sub>2</sub>Hf<sub>2</sub>O<sub>7</sub>/Si thin film grown by pulsed laser deposition, *Appl. Surface Science*, **256**, 838, (2009).
- [21] G. Apostolopoulos, G. Vellianitis, A. Dimoulas, Complex admittance analysis for La<sub>2</sub>Hf<sub>2</sub>O<sub>7</sub>/SiO<sub>2</sub> high-κ dielectric stacks, *Appl. Phys. Lett.* **84**, 260 (2004).

- [22] M. Y. Koledintseva, R. E. DuBroff, R. W. Schwartz, A Maxwell Garnett Model for Dielectric Mixtures Containing Conducting Particles at Optical Frequencies, *Progress In Electromagnetics Research, PIER*, **63**, 223 (2006).
- [23] K. Kempa, Dielectric function of media based on conductive particles, *Phys. Rev. B* **74**, 033411 (2006).
- [24] K. Yee, Numerical solution of initial boundary value problems involving maxwell's equations in isotropic media, *IEEE Trans. Antenn. Propag.* **14**, 302 (1966).
- [25] Computer simulation technology, <https://www.cst.com/>
- [26] D. R. Smith, D. C. Vier, Th. Koschny, C. M. Soukoulis, Electromagnetic parameter retrieval from inhomogeneous metamaterials, *Phys. Rev. E*, **71**, 036617 (2005).
- [27] D. R. Smith, Analytic expressions for the constitutive parameters of magnetoelectric metamaterials, *Phys. Rev. E*, **81**, 036605 (2010).
- [28] R. Liu, T. Cui, D. Huang, B. Zhao, D. R. Smith, Description and explanation of electromagnetic behaviors in artificial metamaterials based on effective medium theory, *Phys. Rev. E*, **76**, 026606 (2007).
- [29] M. Esposito, V. Tasco, F. Todisco, A. Benedetti, D. Sanvitto, A. Passaseo, Three Dimensional Chiral Metamaterial Nanospirals in the Visible Range by Vertically Compensated Focused Ion Beam Induced-Deposition, *Adv. Opt. Mater.* **2**, 154 (2014).
- [30] V. Tasco, M. Esposito, F. Todisco, A. Benedetti, M. Cuscunà, D. Sanvitto, A. Passaseo, Three-dimensional nanohelices for chiral photonics, *Appl. Phys. A* **122**, 280 (2016).
- [31] M. Esposito, V. Tasco, F. Todisco, M. Cuscunà, A. Benedetti, M. Scuderi, G. Nicotra, Programmable Extreme Chirality in the Visible by Helix-Shaped Metamaterial Platform, A. Passaseo, *Nano Lett.* **16**, 5823 (2016).
- [32] N. Matsushita, C. P. Chong, T. Mizutani, M. Abe, Granular composites containing “micro-ions,” permeability, and permittivity calculated for application to microwave absorbers, *J. Appl. Phys.* **91**, 7376 (2002).
- [33] J. Shim, J. Kim, S. H. Han, H. J. Kim, K. H. Kim, M. Yamaguchi, Nanocrystalline Fe-Co-Ni-B thin film with high permeability and high-frequency characteristics, *J. Magn. Magn. Mater.* **290-291**, 205-208 (2005).

## **Chapter 4. Engineering electron-phonon interaction with metamaterial plasmonic structures: reducing the electron-phonon scattering in semiconductors**

The results from this chapter have been published in Ref. [1]. Typically, plasmonic and metamaterial systems are designed for controlling photons, in the entire frequency range (from microwaves to visible), and this was the aim of research presented in the previous chapters. However, in general, one can consider engineering interaction of these structures with other quasi-particles, such as phonons. The reason is simply the fact, that these effects are also governed by a dynamic response of charges, with the effective dielectric functions controlling the strengths. This is the subject covered in this chapter, which will focus on the completed project: design of a plasmonic-metamaterial scheme to reduce electron-phonon scattering in semiconductors. A related topic investigating the possibility of controlling the electron-phonon interaction (Cooper pairing) in BCS superconductors is a subject of an ongoing, theory-experiment research effort, and therefore the preliminary results are presented in this thesis as an Appendix D.

### **4.1 Reducing the electron-phonon scattering in high mobility transistors**

#### **4.1.1 Introduction**

A High-electron-mobility transistor (HEMT) is a field-effect transistor based on heterojunctions formed between semiconductors (or insulators) with different band gaps [2]. It has been widely used in microwave devices thanks to the advantages of high gain,

high speed at high frequency [2-3]. At the junction of doped and undoped semiconductors, a quasi-triangle potential well forms as a result of the charge induced conduction, and/or valence band bending. In case of the n-type doping, the electrons transfer from the doped layer, and become trapped inside this quasi-triangular well on the undoped side, forming a pseudo two-dimensional electron gas (2DEG). This effect is known as remote, or modulation doping. The electron depleted, doped region works as an insulator between the biased gate and the conduction channel. Accumulation of charges can be controlled by the gate voltage. Free carriers can move much faster in the 2DEG than in a doped sample of the same material, since the scattering of the free carriers by the remote ionized impurities is strongly reduced. Also, the high carrier density in the 2DEG reduces the contact resistance. However, the electron-phonon scattering is unaffected by this modulation doping, and this overheating causing scattering presents significant challenge to the continued technological advancement in the microelectronics. The conventional way to deal with this challenge is to focus on the ways of dissipating the excess heat to the environment, such as cooling the substrate [4], using high thermal conductivity substrates (SiC or diamond) [5], and adding a heat-spreading layer close to the hot spot. However, this strategy is becoming less effective for large integrated circuits.

In this work, we follow an alternative approach: instead of improving the heat dissipation into the environment, we suggest a way to reduce its generation in the first place. The electron-phonon scattering affects heat generation in all semiconductors [6-7]. Since the electron-phonon scattering is mediated by a dynamic Coulomb interaction, changing the dielectric environment should in principle, and indeed does [8-9] affect it. We follow, and enhance this idea here, by showing that large reductions in the electron-phonon scattering

(in polar semiconductors) can be achieved by two-dimensional (2D) plasmonic arrays, embedded in an insulating layer adjacent to the 2D conducting channel of the HEMT configuration. These reductions arise from the strong, dynamic screening produced by these metallic resonators. By judicious design of the plasmonic layers, we find remarkably large enhancements of the simulated carrier mobilities and corresponding reductions in joule heating in the GaAs, GaN and MoS<sub>2</sub> structures.

#### **4.1.2 Electron-phonon interaction in semiconductors**

The interaction between electrons and phonons is ubiquitous in condensed matter physics [6]. For example, it governs the onset of conventional superconductivity, and it limits carrier and heat transport in metals and semiconductors. Since the electron-phonon interaction (EPI) is fixed by material-specific properties such as electron band structure, phonon dispersions, and dielectric properties, tailoring the strength of the EPI is challenging. One way to accomplish this is through screening. However, for the moderate carrier densities typically occurring in doped semiconductors, the EPI remains strong and is a dominant scattering mechanism limiting the mobility in technologically important semiconductors such as GaAs, GaN and MoS<sub>2</sub>. Strong screening of the EPI such as what occurs in metals is not possible in semiconductors since such high carrier densities are not achievable and would in any case destroy the functioning of electronic devices.

#### **4.1.3 Motivation for this work**

Recent work has pointed out the strategy of enhancing mobility in 2D conducting layers by changing the dielectric environment [8-9]. This was accomplished through insertion of

adjacent materials with high dielectric constants. However, enhancement is achieved only when carrier interactions with ionized impurities is the dominant scattering mechanism. For clean samples where transport is controlled by electron-phonon scattering, it was shown that insertion of high dielectrics actually reduces mobility [9]. For next-generation devices, where high-quality samples can be fabricated with low concentrations of charged defects, alternative schemes will be needed to improve device performance.

Here we propose a different approach based on the use of plasmonic metamaterial structures to significantly weaken the EPI in polar semiconductors. The idea is to achieve enhanced carrier screening by using a two-dimensional array of metallic plasmonic structures embedded in an insulating layer arranged near a region of current flow in a neighboring semiconductor material. The 2D plasmonic structures act as resonators whose resonant frequencies and oscillator strengths can be tuned by the geometry and arrangement of the structures. In conventional systems, the EPI is screened only by the background dielectric constant, since the free carrier screening is negligible as semiconductor carrier densities are very small (compared to metals). Introduction of the 2D plasmonic resonance provides the desired tunable screening in a nearby electron gas. While it also introduces additional scattering channels for carriers, the electron-plasmon scattering does not degrade an electric current thus leaving the mobility unaffected.

## **4.2 Effective dielectric function**

### **4.2.1 Effective dielectric function contribution from the plasmonic structure**

The 2D plasmonic resonators are metallic structures embedded in a dielectric substrate as shown in Figure 4-1(a). The left diagram shows schematics of an envisioned integrated

circuit and high mobility field effect transistor, with plasmonic metallic structures (pink) embedded in a dielectric substrate (yellow). A subsequent magnification (Figure 4-1(b)) shows the 2D homogeneity of the interaction region: electrons moving in the planar channel directly above the plasmonic structure experience essentially a constant dielectric environment, apart from the narrow gaps between the metal units. These gap regions can be minimized to increase the plasmonic shielding and improve the overall uniformity of the structure. The in-plane plasmonic structure uniformity allows for an effective medium dielectric treatment of the electron-phonon scattering process.

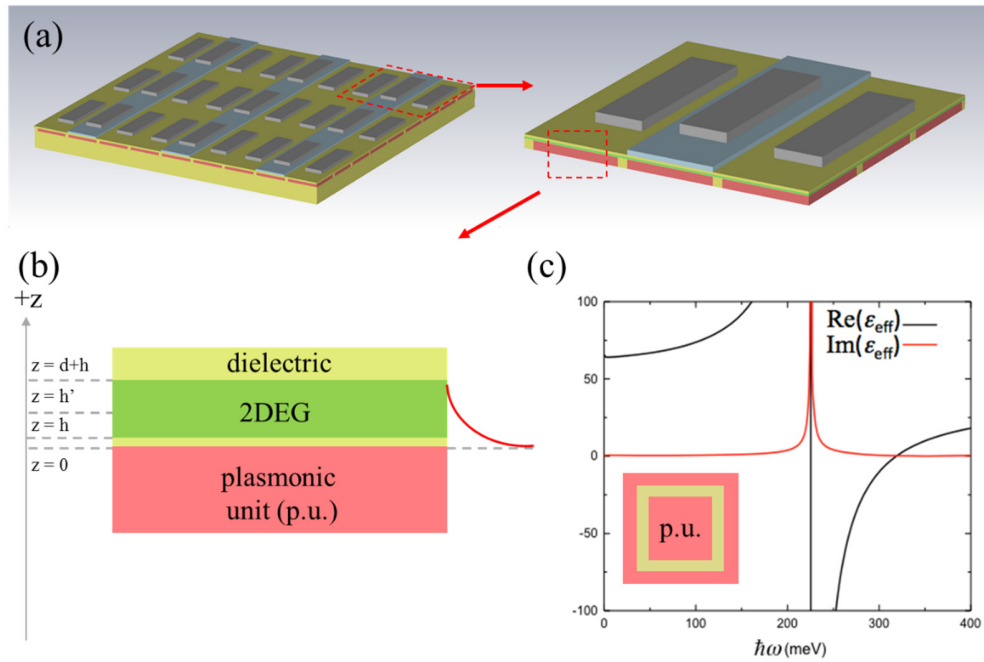


**Figure 4-1. Envisioned structure and its dielectric response.** (a) Schematic of an integrated circuit (top left) and field effect transistor (top right), with plasmonic metallic structure fragments (pink) shown embedded in the substrate dielectric (yellow), (b) The electron-phonon interaction region, as described in text. Green region represents the 2D electron gas separated from a unit in the plasmonic structure (p.u.) by a distance,  $h$ . Simulated electric field vs distance away from the p.u. is indicated by the red curve to the right; (c) The extracted real and imaginary parts of the dielectric function for a gold plasmonic structure with  $1 \mu\text{m}$  square-bar unit cell (labeled p.u.) using a GaN dielectric as the background material, modeled in FIT simulations. Taken from Ref. [1].

The basic physics can be described approximately as follows. The propagating phonon waves in a polar medium scatter electron in the channel. The scattering process is subject to screening effects as described by a dielectric response [10]. To calculate the dielectric function produced by the plasmonic structure, one could simply consider charges induced by a propagating phonon wave on the surface of the plasmonic structure. Using a Fresnel optics analysis, we show below that the field of the reflected wave from these induced interface charges at the 2DEG, which can be considered a polarization field produced by the plasmonic structure, has the approximate form [10]

$$\vec{P}(\vec{q}, h; \omega) \approx \vec{E}^{inc}(\vec{q}, \omega) \alpha'(\vec{q}^{ref}) e^{-iq_z^{ref} h} \approx \vec{E}^{inc}(\vec{q}, \omega) \alpha(Q) e^{-Qh'} \quad (4-1)$$

where  $\vec{E}^{inc}(\vec{q}, \omega)$  is the field of the incoming phonon wave impinging on the metal surface, and  $q_z^{ref} = \sqrt{\omega^2 n^2 / c^2 - Q^2} \approx iQ$ , where  $n$  is the refractive index of the plasmonic structure, and  $Q$  is the in-plane component of  $\vec{q}^{ref}$ . The distance,  $h' = h + d/2$  is that from the plasmonic structure to the center of the 2DEG of thickness,  $d$ , as shown in Figure 4-1. With the polarization field given by Equation 4-1, the effective dielectric function at the 2D electron gas shows an exponential form [11]:

$$\varepsilon_{eff}(Q, \omega) \approx \varepsilon_\infty + \alpha(Q) e^{-Qh} \approx \frac{1}{2} \left\{ \varepsilon_m(Q, \omega) e^{-Qh} + \varepsilon_\infty (2 - e^{-Qh}) \right\} \quad (4-2)$$

where  $\varepsilon_m(Q, \omega)$  is the dielectric function of the plasmonic structure and  $\varepsilon_\infty$  is that of the semiconductor/insulator dielectric medium. The quantity  $\alpha(Q)$  is chosen so that Equation 4-2 satisfies the required limit of a simple average of polarization contributions from neighboring regions:  $\varepsilon_{eff}(0, \omega) = \frac{1}{2} \left\{ \varepsilon_m(0, \omega) + \varepsilon_\infty \right\}$ . Equation 4-2 is quite general, and can

be derived by a variety of methods. The evanescent nature of the reflected field as given in Equation 4-1 is confirmed by the following FIT simulation.

#### 4.2.2 FIT simulations of the plasmonic field screening

In the scattering calculations we employed Equation 4-1 to obtain the effective dielectric function in the 2DEG from the plasmonic structure. The exponential behavior is expected from Fresnel optics, which considers any system as a collection of uniform regions, with fields properly matching at each interface. In this spirit, the electric field in the uniform region outside the metal-semiconductor interface has the following spatial dependency  $\vec{E}(\vec{q}, \omega) \sim e^{i\vec{q}\cdot\vec{r} - i\omega t} \sim e^{iq_z z}$ . Since typical values of the wave vectors assure that  $Q^2 \gg \omega^2 n / c^2$ , the evanescent behavior, as included in Equation 4-1, emerges, since then  $q_z = \sqrt{\omega^2 n / c^2 - Q^2} \approx iQ$ . We employ FIT simulations to confirm this evanescent field decay by commercial FIT software package made by CST (computer simulation technology) [12]. We simulated a response of the flat metal-dielectric interface to an oscillating dipole placed in the semiconductor (frequency = 10 THz, dipole of length  $l = 50$  nm, and diameter  $d = 11$  nm) a distance  $h = 10$  nm away from the interface (Figure 4-2). The metal (gold) was modeled by the Drude response with conductivity  $\sigma = 4 \times 10^7$  S/m [13], and the permittivity of the semiconductor (GaN) was set to 9.5 [14]. A plot of the absolute amplitudes of the electric fields plotted vs distance is shown below. In fact, the degree of the decay is exactly as expected. The dipole produces a wave with a wavelength roughly  $2\lambda = 100$  nm, and thus the e-fold reduction of the evanescent field occurs at  $1/Q = \lambda/\pi = 16$  nm, which indeed is roughly the case sketched in Figure 4-1b (red curve on the

semiconductor side). This confirms the form of Equation 4-1 in the main text. The exponential decay is general and holds for the larger  $Q_{\text{ave}}$  values given above.

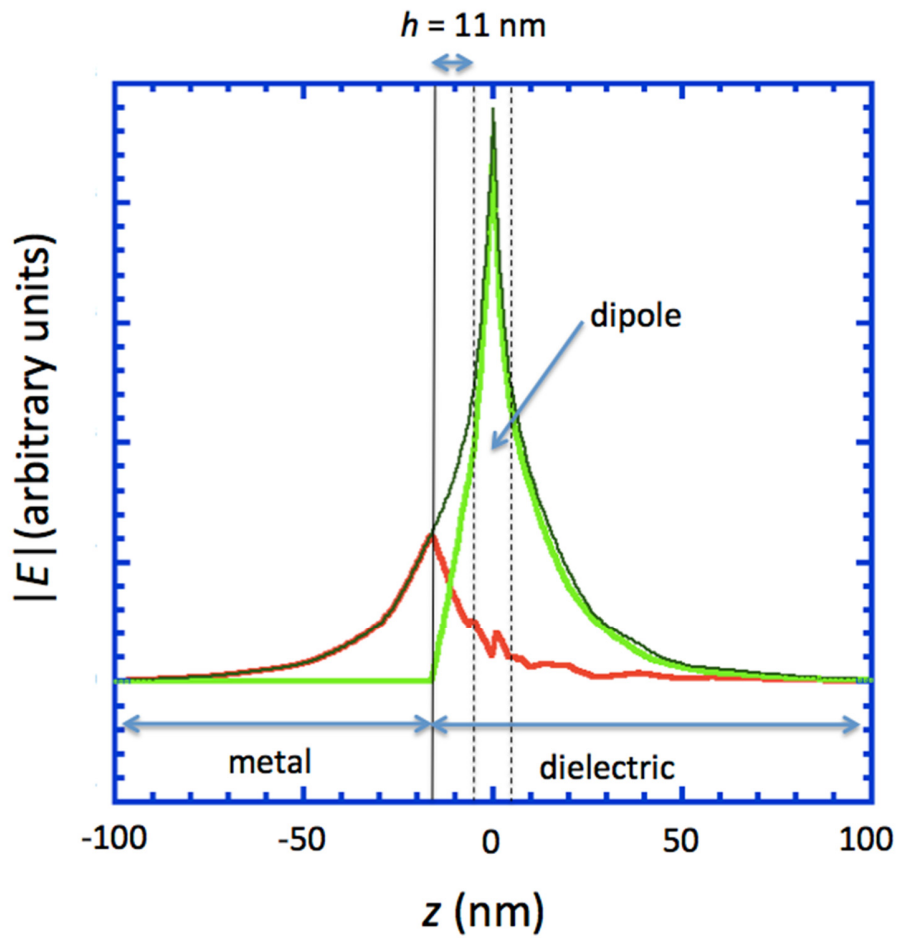


**Figure 4-2. The absolute amplitudes of the electric fields vs distance between the 2DEG and plasmonic metallic structure.** The black line is for the total dipole field in the absence of the metallic structure. The green line is for the total field in the presence of the structure, and the red line is for the extracted evanescent field of the charges induced on the metallic interface. Taken from Ref. [1].

### 4.2.3 Extracting an effective dielectric response of plasmonic structures

The extraction is achieved by comparing the Fresnel wave analysis with the simulated results. In principle,  $\varepsilon_m(0, \omega)$  can be analytically continued into the corresponding non-local form  $\varepsilon_m(Q, \omega)$ . This analytical continuation can be accomplished [15] by renormalization of  $\omega_0$  as follows

$$\varepsilon_m(q, \omega) = \varepsilon_b + \frac{\omega_p^2}{\omega_0^2 A(q) - \omega(\omega + i\gamma)} \quad (4-3)$$

where  $A(q) = 1 - aq + bq^2$ , where  $q$  is the isotropic wave vector amplitude. It was shown in Ref. 14, that for most plasmonic metals  $A(q)$  remains of order one, even for  $q$  approaching the Brillouin zone. Thus, to zero<sup>th</sup> order we can write

$$\varepsilon_{eff}(Q, \omega) \approx \varepsilon_m(0, \omega) = \varepsilon_b + \frac{\omega_p^2}{\omega_0^2 - \omega(\omega + i\gamma)} \quad (4-4)$$

where  $\omega_0$  is the plasmonic structure resonance,  $\omega_p$  is the corresponding strength of that resonance,  $\gamma$  is a broadening parameter, and  $\varepsilon_b$  is the background dielectric constant from the bound electrons in the metal. These parameters can be extracted by comparing the response (e.g. transmittance) obtained from a plane wave analysis (e.g. Fresnel), and the FIT simulations of the metallic structure in the retarded limit [16-17]. Typical form of the extracted, long wavelength complex dielectric function is shown in Figure 4-1(c). This dielectric function was calculated for a square-ring metallic structure made of gold, shown in an inset in Figure 4-1c. It was obtained employing the CST software [12]. The motivation for choosing this specific structure and dimensions was: large metal coverage,

low enough resonant frequency, and strong resonance. The extracted effective dielectric function is subsequently used in the transport calculations, described in detail in Ref. [11].

### 4.3 Carrier mobility calculations

#### 4.3.1 General formalism

The carrier transport, occurring in a thin conducting semiconducting channel as shown in Figure 4-1, has been described in detail in Ref. [10], attached to this thesis as Appendix A. Here we summarize the most important results from this collaborative work, focusing on the effects due to plasmonic structures. The carrier mobility is calculated by solving the Boltzmann transport equation. The relevant scattering due to EPI is given in the random phase approximation (RPA) by [10]

$$S^{el-ph}(\mathbf{k}, \mathbf{k}') = \frac{2\pi}{\hbar} \frac{|M_{el-ph}(\mathbf{k}, \mathbf{k}')|^2}{|\varepsilon_{el}(Q, \omega) + \varepsilon_{eff}(Q, \omega)|^2} \delta(\varepsilon_{\mathbf{k}'} - \varepsilon_{\mathbf{k}} \pm \hbar\omega_{\lambda}) \quad (4-5)$$

where  $\varepsilon_{\mathbf{k}}$  is the electron energy with wave vector  $\mathbf{k}$ ,  $\hbar\omega_{\lambda}$  is the phonon energy in mode  $\lambda$  and the  $\pm$  signs refer to phonon emission and absorption, respectively.  $M_{el-ph}(\mathbf{k}, \mathbf{k}')$  is the matrix element describing the EPI,  $\varepsilon_{el}(Q, \omega)$  is the dielectric function contribution from the 2D electron gas in the semiconducting channel, given by

$$\varepsilon_{el} = \varepsilon_{\infty} - v_Q P(Q, \omega), \quad (4-6)$$

where  $v_Q = 2\pi e^2 / Q$ , and  $P(Q, \omega)$  is the polarization. The Boltzmann Equation is solved for the non-equilibrium distribution function, from which an electron lifetime,  $\phi(\varepsilon_{\mathbf{k}})$ , is extracted. The mobility is subsequently given by

$$\mu = \frac{e}{3n} \int_0^{\infty} \left( -\frac{\partial f_0}{\partial \varepsilon} \right) v^2 g(\varepsilon) \phi(\varepsilon) d\varepsilon \quad (4-7)$$

where  $v = \hbar k / m^*$  is the carrier velocity,  $g(\varepsilon)$  is the density of states, and  $n$  is the electron density.

### 4.3.2 Plasmonic mobility enhancement in GaAs and MoS<sub>2</sub>

The calculated room temperature mobility,  $\mu_{meta}$ , for a 1 nm thick 2D GaAs layer near the plasmonic structures is shown in Figure 4-3 as a function of the distance from the center of the conducting layer to the metal ( $h'=h+d/2$ ) for an electron concentration of  $10^{11}$  cm<sup>-2</sup> and for different values of the plasmonic enhancement factor  $\chi = \omega_p^2 / \omega_0^2 \varepsilon_\infty$  (see Appendix A). This mobility is scaled by that for the 2D electron gas without the plasmonic structure,  $\mu_0$ , at the same electron density. As  $h'$  decreases, remarkably large mobility enhancements are achieved with increasing  $\chi$ . These large enhancements reflect the increasingly strong screening from the plasmonic structure as it approaches the GaAs layer. Increasing the carrier density from  $10^{11}$  cm<sup>-2</sup> to  $10^{12}$  cm<sup>-2</sup> reduces the relative enhancement, but this reflects mainly the increase in the mobility of the 2D layer without the plasmonic structure resulting from the free carrier screening: The absolute mobilities for small  $h$  and large  $\chi$  are relatively insensitive to the electron density. Also, there is little change in the mobility for the GaAs layer when the temperature is increased above 300K. Similar qualitative behavior is seen for a GaN structure (Figure 4-4) and for an MoS<sub>2</sub> monolayer (Figure 4-5), with mobility enhancements of over an order of magnitude found for small  $h$  and large  $\chi$ .

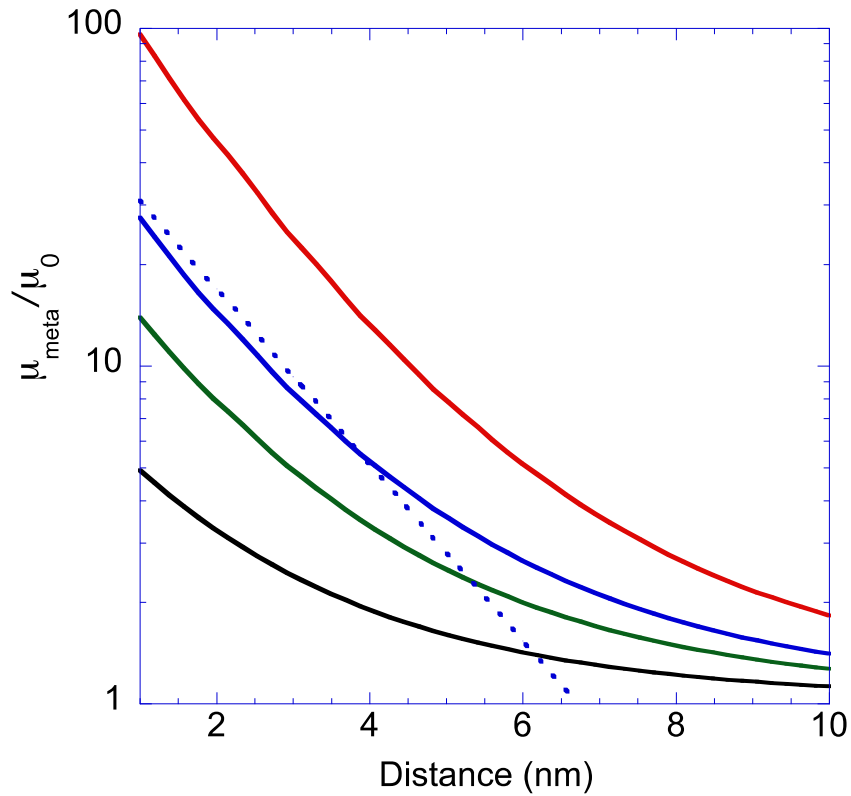


**Figure 4-3. Mobility enhancement in GaAs structure.** Mobility of a 1 nm thick GaAs layer,  $\mu_{meta}$ , with electron density of  $10^{11} \text{ cm}^{-2}$  at 300K near a 2D plasmonic structure as a function the distance from the center of the layer  $h'=h+d/2$ .  $\mu_0$  is the mobility calculated for the same GaAs layer but without the plasmonic structure. Results are shown for four different plasmonic enhancement factors:  $\chi = 5$  (black curve),  $\chi = 10$  (green curve),  $\chi = 15$  (blue curve) and  $\chi = 30$  (red curve), as defined in the text. Dotted blue curve is for the simple model described in the text with  $\chi = 15$  (see Ref.[9]). Taken from Ref. [1].

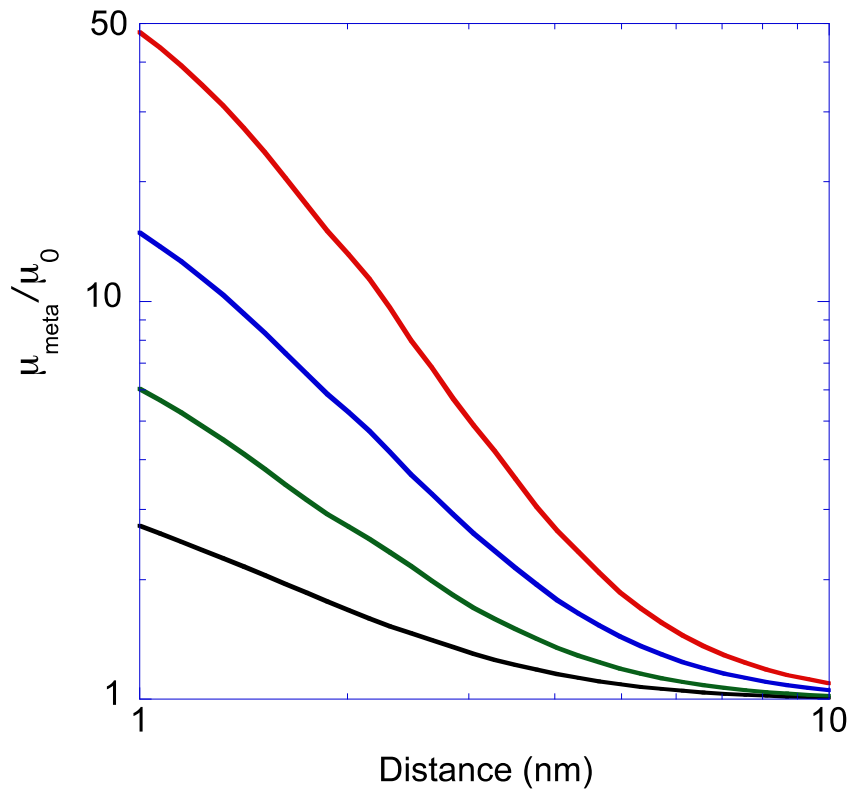


**Figure 4-4. Mobility enhancement in GaN structure.** Scaled room temperature mobility of a 1 nm thick GaN 2DEG layer with electron density of  $10^{11} \text{ cm}^{-2}$  as a function of the distance from a 2D plasmonic structure, as in Figure 4-2. Black, green, blue and red curves are for  $\chi=5, 10, 15$  and  $30$ , respectively. Taken from Ref. [1].

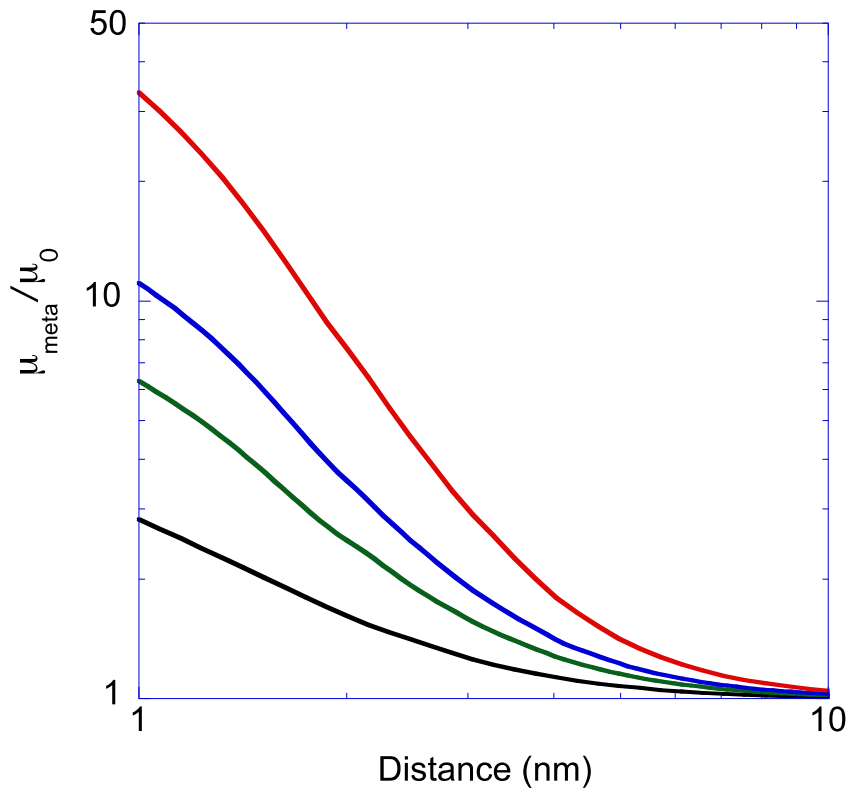


**Figure 4-5. Mobility enhancement in MoS<sub>2</sub> structure.** Scaled room temperature mobility of a monolayer of MoS<sub>2</sub> with electron density of  $10^{11} \text{ cm}^{-2}$  as a function of the distance away from a 2D plasmonic structure, as in Figure 4-2 and 3. Black, green, blue and red curves are for  $\chi=5, 10, 15$  and  $30$ . Taken from Ref. [1].

#### **4.4 Summary**

In conclusion, very strong mobility enhancement (by a factor of 30 to 100), and the corresponding reduction in Joule heating, is obtained at 1 nm distance between 2DEG and plasmonic structure for all cases. It is important to note, that such a small (1 nm) spacing is currently achievable with industrial processes. Also, in all cases this enhancement decays rapidly as the plasmonic structure is moved away from the 2DEG, with negligible effect beyond 10 nm. In all cases, the plasmonic resonance frequency is chosen to be well above the relevant phonon frequencies.

## References:

- [1] X. Wu, J. Kong, D. Broido, and K. Kempa, Tailoring the electron-phonon interaction with metallic plasmonic structures, Under review in *Materials Today Physics* (2018).
- [2] O. Ambacher, J. Smart, J. R. Shealy, N. G. Weimann, K. Chu, M. Murphy, W. J. Schaff, L. F. Eastman, Two-dimensional electron gases induced by spontaneous and piezoelectric polarization charges in N- and Ga-face AlGa<sub>N</sub>/Ga<sub>N</sub> heterostructures, *J. Appl. Phys.* **85**, 3222 (1999).
- [3] S. Oktyabrsky, P. Ye, *Fundamentals of III-V Semiconductor MOSFETs*, New York: Springer (2010).
- [4] A. Nigam<sup>1</sup>, T. N. Bhat, S. Rajamani, S. B. Dolmanan, S. Tripathy, M. Kumar, Effect of self-heating on electrical characteristics of AlGa<sub>N</sub>/ Ga<sub>N</sub> HEMT on Si (111) substrate, *AIP Advances*, **7**, 085015 (2017)
- [5] S. Arulkumar, T. Egawa, H. Ishikawa, T. Jimbo, High-temperature effects of AlGa<sub>N</sub>/Ga<sub>N</sub> high-electron-mobility transistors on sapphire and semi-insulating SiC substrates, *App. Phys. Lett.*, **80**, 2186 (2002).
- [6] J. M. Ziman, *Principles of the Theory of Solids*, 2nd ed., London: Cambridge University Press (1972).
- [7] N. W. Ashcroft, N. D. Mermin, *Solid State Physics*, 1st ed., New York: Holt, Rinehart and Winston (1976).
- [8] D. Jena, A. Konar, Enhancement of Carrier Mobility in Semiconductor Nanostructures by Dielectric Engineering, *Phys. Rev. Lett.* **98**, 136805 (2007).
- [9] N. Ma, D. Jena, Charge Scattering and Mobility in Atomically Thin Semiconductors, *Phys. Rev. X* **4**, 011043 (2014).
- [10] G. D. Mahan, *Many-Particle Physics*, 3rd ed., New York: Springer US (2000).
- [11] Thesis of J. Kong, Boston College, (2018).
- [12] [www.cst.com](http://www.cst.com)
- [13] R. A. Serway, *Principles of Physics*, 2nd ed., Texas: Fort Worth (1998).
- [14] D. D. Manchon, A. S. Barker, P. J. Dean, R. B. Zetterstrom, Optical studies of the phonons and electrons in gallium nitride, *Solid State Commun.* **8**, 1227 (1970).
- [15] A. J. Shvonski, J. Kong, K. Kempa, Nonlocal extensions of the electromagnetic response of plasmonic and metamaterial structures, *Phys. Rev. B* **95**, 045149 (2017).
- [16] D. R. Smith, S. Schultz, P. Markoš, C. M. Soukoulis, Determination of effective permittivity and permeability of metamaterials from reflection and transmission coefficients, *Phys. Rev. B* **65**, 195104 (2002).
- [17] D. R. Smith, B. Pendry, Homogenization of metamaterials by field averaging, *J. Opt. Soc. Am. B* **23**, 391 (2006).

## Chapter 5. Summary

In conclusion, we have presented studies on electromagnetic responses of plasmonic structures, including the following aspects: (1) enhanced topologically protected edge states of electromagnetic waves in the visible range in ENZ gyroelectric metamaterials; (2) high  $k$  composite materials in low frequency with plasmonic structures; and (3) engineering electron-phonon interactions with metamaterial plasmonic structures. These works show the broad range of applications of plasmonic metamaterials in both photonic and phonon systems. These concepts can potentially be applied to modify the  $T_c$  of BCS superconductors such as Al, Pd, or  $MgB_2$  via tailoring the electron-phonon interactions. Plasmonic structures can also create channels to utilize the hot electron energy in semiconductor solar cells. The multi-exciton generation effect, which is vanishingly small effect in bulk materials, can be significantly enhanced through plasmonic structures to make solar cells with efficiencies exceeding the Shockley-Queisser limit.

**Appendix A. Topologically protected photonic edge states in the visible in plasmo-gyroelectric metamaterials**

The following paper is published in *Advanced Optical Materials* on 09 May 2018.

Citation information:

Xueyuan Wu, Fan Ye, Juan M. Merlo, Michael J. Naughton, and Krzysztof Kempa, “Topologically Protected Photonic Edge States in the Visible in Plasmo - Gyroelectric Metamaterials”, *Advanced Optical Materials* **6**(15) 1800119 (2018).

<https://doi.org/10.1002/adom.201800119>



# Topologically Protected Photonic Edge States in the Visible in Plasmo-Gyroelectric Metamaterials

Xueyuan Wu, Fan Ye, Juan M. Merlo, Michael J. Naughton, and Krzysztof Kempa\*

Gyroelectric materials can be used to realize nontrivial photonic topological states. The usual strategy to maximize this effect is to increase the strength of the typically very small, off-diagonal dielectric permittivity tensor components. This is a very difficult task, in particular at high frequencies. Here, an alternative method is proposed: reducing the strength of the diagonal permittivity tensor components. It is shown that this can be achieved by employing a layered plasmo-gyroelectric metamaterial as the background medium of a 2D photonic crystal. It is demonstrated that by applying magnetic field, which breaks time reversal invariance, a topologically nontrivial photonic gap opens in the band structure of square and hexagonal photonic crystals. This is confirmed by detecting the presence of a topologically protected edge state at the boundary of this structure. This state is a photonic analog of the edge state in the conventional integer quantum Hall effect, also characterized by suppressed backscattering.

Asymmetric propagation of light has been a field of growing interest in recent years. Many works exploit breaking of geometrical symmetries to alter coupling pathways between different photonic modes, and to generate asymmetric propagation.<sup>[1–3]</sup> This cannot, however, yield true optical isolators (nonreciprocal photonic systems), since these require time-reversal invariance (TRI) to be broken.<sup>[4]</sup> On the other hand, nonreciprocal photonics, based on broken TRI induced by external fields or internal interactions, promises the possibility of scattering-free and reflection-free one-way light propagation.<sup>[5–10]</sup> In this context, photonic topological insulators (PTI) have been proposed and intensively studied.<sup>[9–12]</sup> These include analogs of the integer quantum Hall effect (IQHE), where Haldane has demonstrated that broken TRI is the most general requirement for the occurrence of the IQHE state.<sup>[13]</sup> He showed that

broken TRI, produced not by an external macroscopic magnetic field, but locally in a honeycomb lattice of magnetic atoms, leads to formation of a topologically nontrivial Landau-like gap, and consequently to a unidirectional edge current and quantized conductivity. Raghu and Haldane proposed a photonic analog of this effect in photonic crystals, with TRI broken by the Faraday (gyroelectric) effect.<sup>[14]</sup> They demonstrated that when TRI is broken in this way, the Chern numbers take nonzero values, which leads to topologically nontrivial photonic gaps and topologically protected (with suppressed backscattering) edge states. TRI can also be broken by gyromagnetic materials, but only at relatively low (microwave) frequencies. Gyroelectric materials, instead, break TRI in the presence of a magnetic field even at visible

frequencies, albeit very weakly so (the ratio of the off-diagonal to diagonal (OTD) components of the dielectric permittivity tensor is of the order of  $10^{-3}$ ).<sup>[15]</sup> This results in very small gaps, making observation of edge modes difficult. Nevertheless, nonreciprocal lasing in topological cavities was recently demonstrated in a system which used the gyroelectric material yttrium iron garnet coupled to a multiple quantum well lasing cavity.<sup>[16]</sup> In the present work, we propose an alternative strategy to dramatically increase the tensor component ratio in gyroelectric systems: strong reduction of the diagonal components with a plasmo-gyroelectric metamaterial (PGM).

We first demonstrate that it is the ratio of the OTD components of the permittivity tensor, not their absolute values, that controls the physics of TRI breaking in a PTI. For a nonmagnetic ( $\mu = 1$ ), source-free, nonconducting anisotropic medium with harmonic time dependence, Maxwell's equations reduce to

$$\nabla \times (\nabla \times E) = \frac{\omega^2}{c^2} \hat{\epsilon} E \quad (1)$$

where  $E$  is the electric field,  $c$  speed of light,  $\omega$  the mode frequency, and relative permittivity given by the tensor  $\hat{\epsilon} = \{\hat{\epsilon}_{ij}\}$  ( $i, j = x, y, z$ ). Clearly, by assuming that all tensor components are uniformly scaled, *i.e.*  $\hat{\epsilon} = \alpha \hat{\epsilon}'$ , where  $\alpha$  is a scaling constant, one can transform Equation (1) into an identical one, but with  $\hat{\epsilon}$  replaced with  $\hat{\epsilon}'$ , and  $\omega$  replaced with  $\omega\sqrt{\alpha}$ . Thus, the only consequence of such uniform scaling is the mode frequency change (renormalization). Then, only the ratios of the tensor components represent nontrivial physical effects, such as TRI breaking. As such, increasing the off-diagonal components of

X. Wu, Dr. J. M. Merlo, Prof. M. J. Naughton, Prof. K. Kempa  
Department of Physics  
Boston College  
Chestnut Hill, Massachusetts, MA 02467, USA  
E-mail: kempa@bc.edu

Dr. F. Ye  
Department of Physics  
LASSP  
Cornell University  
Ithaca, NY 14853, USA

Dr. F. Ye  
Howard Hughes Medical Institute  
Cornell University  
Ithaca, NY 14853, USA

DOI: 10.1002/adom.201800119

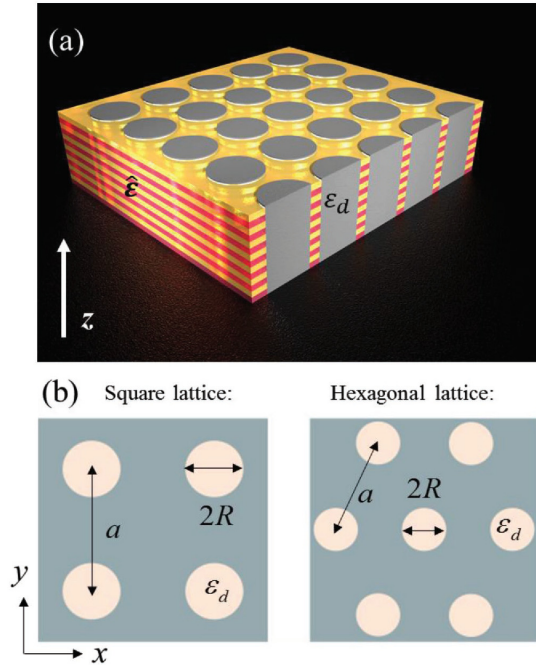


**Figure 1.** a) The basic structure of the PTI consists of a 2DPC made of dielectric rods, immersed in a metamaterial superlattice made of alternating metallic and gyroelectric films. b) Schematics of the unit cells of the square and hexagonal 2DPC.

the effective permittivity tensor, so that they are of the order of the diagonal components, is equivalent to reducing the strength of the diagonal components relative to the off-diagonal components. This is the key idea of this paper.

We propose here to achieve the desired suppression of the diagonal tensor components by employing a PGM structure made of a superlattice of alternating metallic and gyroelectric layers, with the response tuned to the near-zero diagonal tensor components condition. This composite structure will be used as a dielectric background of a 2D photonic crystal (2DPC) made of dielectric cylinders, as shown in Figure 1a. In the absence of magnetic field, this 2DPC will be designed to have photonic bands with degenerate points which, after application of a TRI-breaking external magnetic field, will open robust, topologically nontrivial gaps.

It has been shown<sup>[17]</sup> that the effective permittivity tensor components  $\epsilon_{ij}$  of the superlattice can be obtained from the tensor components of the constituent layers ( $i, j = x, y$ )

$$\epsilon_{ij} = f_m \epsilon_{ij}^m + f_g \epsilon_{ij}^g \quad (2)$$

$$\epsilon_{zz} = (f_m / \epsilon_{zz}^m + f_g / \epsilon_{zz}^g)^{-1} \quad (3)$$

$$\epsilon_{xz} = \epsilon_{zx} = \epsilon_{yz} = \epsilon_{zy} = 0 \quad (4)$$

Here,  $m$  and  $g$  refer to the metal and gyroelectric layers and the  $f$ 's denote the thickness fill factors of the respective layers, which trivially obey the condition  $f_m + f_g = 1$ . For given  $\epsilon_{ij}^m$  and  $\epsilon_{ij}^g$ , one can choose  $f_m$  and  $\alpha$  to achieve a desired OTD ratio in the effective permittivity tensor. As an example, we use the following permittivity tensor for aluminum<sup>[18]</sup> (at operating frequency of  $\approx 2$  eV)

$$\hat{\epsilon}^m = \begin{bmatrix} -50 & 0 & 0 \\ 0 & -50 & 0 \\ 0 & 0 & -50 \end{bmatrix} \quad (5)$$

and the following tensor, for a gyroelectric layer made of  $\text{CuFe}_2\text{O}_4$ , operating at frequency of  $\approx 2$  eV and magnetic field given in<sup>[19]</sup>

$$\hat{\epsilon}^g = \begin{bmatrix} 4 & 0.01i & 0 \\ -0.01i & 4 & 0 \\ 0 & 0 & 4 \end{bmatrix} \quad (6)$$

We next parameterize Equations (2)–(4) for materials (5) and (6) to engineer an OTD ratio of 5. By choosing  $f_m = 0.0741$  (which leads to  $f_g = 0.926$ ), the effective permittivity tensor of the composite superlattice in the presence of external magnetic field becomes

$$\hat{\epsilon} = \begin{bmatrix} 0.00185 & 0.00926i & 0 \\ -0.00926i & 0.00185 & 0 \\ 0 & 0 & 4.35 \end{bmatrix} = \alpha \begin{bmatrix} 0.1 & \gamma i & 0 \\ -\gamma i & 0.1 & 0 \\ 0 & 0 & 234.7 \end{bmatrix} \quad (7)$$

Here, the magnetic field strength is characterized by  $\gamma = 0.5$ , and the frequency renormalization scaling factor is  $\alpha = 0.0185$ . While the original gyroelectric OTD ratio in the presence of magnetic field was  $0.01/4 = 0.0025$ , for this PGM superlattice, it becomes 5 (note that in the absence of the magnetic field,  $\gamma = 0$ ). Note that the results in this work are independent of  $\epsilon_{zz}$ .

The next step is to use this effective medium with the permittivity tensor given by Equation (7) as a background dielectric for a 2DPC of dielectric cylinders, as shown in Figure 1a. We investigate two 2DPCs, based on a square and a hexagonal (Figure 1b) lattice of cylinders. We assume that the permittivity of the cylinders is  $\epsilon_d = 4$ . For the square lattice, the designed structure parameters (Figure 1b) are  $a = 1 \mu\text{m}$  and  $R = 0.45 a$ . In the absence of external magnetic field, the band structure of the transverse electric (TE) modes for this 2DPC, calculated using COMSOL simulation software,<sup>[20]</sup> is plotted in Figure 2a. Flat-band degeneracy occurs at the M point, and this can turn into a topologically nontrivial gap (as demonstrated by Wang et al.<sup>[13]</sup>) when TRI is broken. This is achieved by turning on an external magnetic field, which activates the off-diagonal terms in the effective permittivity tensor (Equation (7)). The resulting band structure shown in Figure 2b demonstrates that a robust, absolute gap opens around the degeneracy point. To show that this gap is topologically nontrivial, we truncate the 2DPC to create boundaries. The inset to the right of Figure 2c shows a top view of this truncated system unit cell: there are two boundaries of the structure, at top and bottom. The unit cell is periodically extended in the  $x$ - (horizontal) direction. Asymmetric, perfect

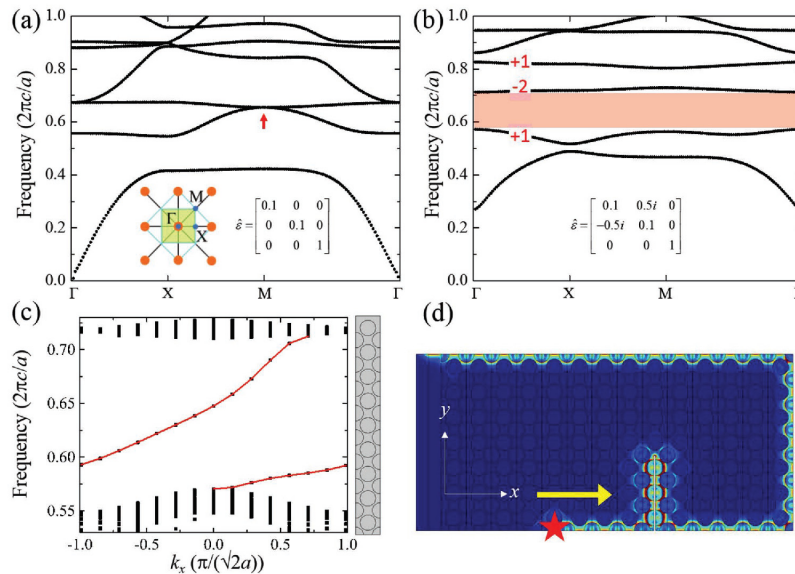


**Figure 2.** PTI based on a square 2DPC immersed in a PGM. Photonic band structure in the absence (a) and presence (b) of an external magnetic field. Corresponding Chern numbers are labeled on topologically nontrivial bands. Left inset in (a): fragment of the reciprocal lattice. Right insets in (a) and (b): dielectric permittivity tensor. c) Edge mode dispersion (red line), and the bulk bands (black squares). Note, that the edge mode “peels off” the bulk states. d) Electric field amplitude of the excited edge mode. The mode is excited with a point dipole (star), oscillating at the frequency of  $0.65 \, 2\pi c/a$ . The mode propagates only along the edge, and only in one (positive  $x$ ) direction. Backscattering is suppressed, even when encountering a large line obstacle made of a PEC boundary. The boundary on the left side is a perfectly matched layer; all other boundaries are PECs.

electric conductor (PEC) configurations at the top and bottom boundaries are adopted to avoid duplication of the edge modes. The calculated mode structure around the bandgap is shown in Figure 2c.

As expected from the topological nature of the gap, an edge mode appears, which spans the gap. This mode has a positive slope (one direction of propagation). To show that the edge mode is protected against backscattering, we placed a point dipole source at the edge (marked as a star in Figure 2d), and excited it at the renormalized frequency  $\omega/(2\pi c/a) = 0.65$  (i.e., within the topological bandgap). In this case, we have added a boundary on the right edge of the window shown in Figure 2d. It is quite obvious that the mode propagates only along the edge, and only in one (positive) direction, and when encountering a large line obstacle made of a PEC boundary, no scattering or reflection of this mode occurs. Instead, the edge mode circumvents the obstacle to continue its net propagation in the positive  $x$ -direction. The dynamics of this propagation can be seen in a video of the simulation shown in Section 2 in the Supporting Information. Also, to further demonstrate the robust nature of topological edge mode and the suppression of the backscattering, we performed further simulations on this square 2DPC with results given in Figure S1 in the Supporting Information Section 1.

The topologically nontrivial bands are labeled in Figure 2b with the corresponding Chern numbers, calculated as follows. Due to the presence of electric anisotropy, we adopt the magnetic-field formulation of the Maxwell’s equation:<sup>[15,21]</sup>

$$\nabla \times (\hat{\epsilon}^{-1}(\mathbf{r}) \nabla \times \mathbf{H}) = \frac{\omega^2}{c^2} \mathbf{H} \quad (8)$$

With the following definition of the inner product  $\langle \mathbf{H}_1 | \mathbf{H}_2 \rangle = \int d^2 r \mu_0 \mathbf{H}_1 \cdot \mathbf{H}_2$ , the Chern number for the  $n$ -th band can be calculated from<sup>[13,15]</sup>

$$C_n = \frac{1}{2\pi} \int_{\text{BZ}} d^2 k \left( \frac{\partial A_y^m}{\partial k_x} - \frac{\partial A_x^m}{\partial k_y} \right) = \frac{1}{2\pi} \oint_{\text{BZ}} d\mathbf{k} \cdot \mathbf{A}^m \quad (9)$$

where Berry connection  $\mathbf{A}^m(\mathbf{k})$  is defined as<sup>[13,14]</sup>

$$\mathbf{A}^m(\mathbf{k}) \equiv \frac{\langle \nabla_{\mathbf{k}} \mathbf{H}_n | \mathbf{H}_n \rangle - \langle \mathbf{H}_n | \nabla_{\mathbf{k}} \mathbf{H}_n \rangle}{2i \langle \mathbf{H}_n | \mathbf{H}_n \rangle} \quad (10)$$

A contour integral around the first Brillouin zone, or around an arbitrary contour surrounding the frequency degenerate points (some are indicated by red arrows in Figure 2a and Figure 3a) will give the corresponding Chern number. More calculational details are given in the Supporting Information.

An analogous effect occurs for a hexagonal 2DPC lattice, as suggested in ref. [14]. In this case, we chose  $a = 1 \, \mu\text{m}$  and  $R = 0.35 a$ . The band structure for the TE modes without magnetic field is plotted in Figure 3a. A Dirac-like degeneracy occurs at the K point where, as for the square lattice under an external magnetic field ( $\gamma = 0.2$ ), a topologically nontrivial gap opens (Figure 3b). Chern numbers for the bands above and

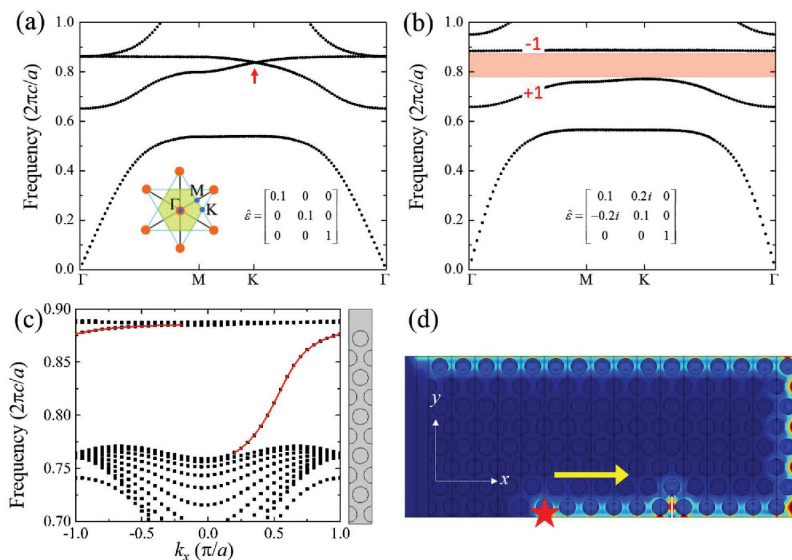


**Figure 3.** PTI based on a hexagonal 2DPC immersed in a PGM. Photonic band structure in the absence (a) and presence (b) of an external magnetic field, with corresponding dielectric permittivity tensors. Corresponding Chern numbers are labeled on topologically nontrivial bands. Left inset in (a): fragment of the reciprocal lattice. Right inset in (a) and (b): dielectric permittivity tensor. c) Edge mode dispersion (red line), and the bulk bands (black squares). Note that the edge mode “peels off” the bulk states. d) Electric field amplitude of an edge mode excited with a point dipole (star), oscillating at the frequency of  $0.85 \, 2\pi c/a$ . The mode propagates only along the edge, and only in one (positive  $x$ ) direction. Backscattering is suppressed, even when encountering a large line obstacle made of a PEC boundary. The boundary on the left side is a perfectly matched layer; all other boundaries are PECs.

below the topologically nontrivial bandgap are calculated to be +1 and -1, respectively, using the above described method, in agreement with ref. [14]. This gap has a similar size to that in Figure 2b, even though a 2.5 times weaker magnetic field was applied. Figure 3c,d shows analogs of Figure 2c,d, respectively. They demonstrate that this hexagonal 2DPC also supports an edge state, protected against backscattering. The dynamics of propagation of the edge mode in this case can also be seen in a simulation video in the Supporting Information Section 2.

Note that in both examples, at relatively small off-diagonal terms, due to the extensively reduced diagonal term value, a large gap size ( $\approx 10\%$ ) is achieved. This large gap size is robust against disorders, and prevents the topologically protected edge modes from radiative losses.<sup>[15]</sup> Although all calculations in the current work are done in nondispersive scenarios, all conclusions can be readily extended to dispersive materials.<sup>[13–15]</sup>

In conclusion, we have demonstrated that 2D photonic crystals of dielectric microrods, immersed in a PGM superlattice, can function as PTI, supporting propagating edge states for which backscattering is suppressed. The PGM superlattice, which in the presence of an external magnetic field breaks TRI, is designed to have a large ratio of off-diagonal to diagonal components of the dielectric permittivity tensor. This large ratio is obtained not by the conventional strategy of maximizing the off-diagonal components, but rather by suppressing the diagonal ones via the plasmonic (negative) response of the metallic films. Due to this large ratio, the bandgaps are robust, even at optical frequencies. This work can pave the way for realization

of topologically protected edge states across a wide frequency range, including optical frequencies.

### Supporting Information

Supporting Information is available from the Wiley Online Library or from the author.

### Conflict of Interest

The authors declare no conflict of interest.

### Keywords

gyroelectric materials, photonic topological insulators, plasmonic metamaterials

Received: January 30, 2018

Revised: March 26, 2018

Published online:

- [1] V. A. Fedotov, P. L. Mladyonov, S. L. Prosvirnin, A. V. Rogacheva, Y. Chen, N. I. Zheludev, *Phys. Rev. Lett.* **2006**, *97*, 167401.
- [2] C. Menzel, C. Helgert, C. Rockstuhl, E.-B. Kley, A. Tünnermann, T. Pertsch, F. Lederer, *Phys. Rev. Lett.* **2010**, *104*, 253902.
- [3] F. Ye, M. J. Burns, M. J. Naughton, *Adv. Opt. Mater.* **2014**, *2*, 957.

- [4] D. Jalas, A. Petrov, M. Eich, W. Freude, S. Fan, Z. Yu, R. Baets, M. Popović, A. Melloni, J. D. Joannopoulos, M. Vanwolleghem, C. R. Doerr, H. Renner, *Nat. Photonics* **2013**, *7*, 579.
- [5] Z. Wang, Y. Chong, J. D. Joannopoulos, M. Soljacic, *Nature* **2009**, *461*, 772.
- [6] S. Manipatrani, J. T. Robinson, M. Lipson, *Phys. Rev. Lett.* **2009**, *102*, 213903.
- [7] H. Lira, Z. Yu, S. Fan, M. Lipson, *Phys. Rev. Lett.* **2012**, *109*, 033901.
- [8] A. R. Davoyan, A. M. Mahmoud, N. Engheta, *Opt. Express* **2013**, *21*, 3279.
- [9] T. Ma, A. B. Khanikaev, S. H. Mousavi, G. Shvets, *Phys. Rev. Lett.* **2015**, *114*, 127401.
- [10] C. He, X. Sun, X. Liu, M. Lu, Y. Chen, L. Feng, Y. He, *Proc. Natl. Acad. Sci. USA* **2016**, *113*, 4924.
- [11] A. B. Khanikaev, G. Shvets, *Nat. Photonics* **2017**, *11*, 763.
- [12] Y. Wu, C. Li, X. Hu, Y. Ao, Y. Zhao, Q. Gong, *Adv. Opt. Mater.* **2017**, *5*, 1700357.
- [13] F. D. M. Haldane, *Phys. Rev. Lett.* **1988**, *61*, 2015.
- [14] F. D. M. Haldane, S. Raghu, *Phys. Rev. Lett.* **2008**, *100*, 013904.
- [15] Z. Wang, Y. Chong, J. D. Joannopoulos, M. Soljacic, *Phys. Rev. Lett.* **2008**, *100*, 013905.
- [16] B. Bahari, A. Ndao, F. Vallini, A. E. Amili, Y. Fainman, B. Kanté, *Science* **2017**, *358*, 636.
- [17] D. J. Bergman, *Phys. Rep.* **1978**, *43*, 377.
- [18] M. A. Ordal, L. L. Long, R. J. Bell, S. E. Bell, R. R. Bell, R. W. Alexander, C. A. Ward, *Appl. Opt.* **1983**, *22*, 1099.
- [19] M. Veis, R. Antos, S. Visnovsky, P. D. Kulkarni, N. Venkataramani, S. Prasad, J. Mistrik, R. Krishnan, *Materials* **2013**, *6*, 4096.
- [20] COMSOL Multiphysics v5.2, COMSOL AB, Stockholm, Sweden **2017**, www.comsol.com.
- [21] J. D. Joannopoulos, S. G. Johnson, J. N. Winn, R. D. Meade, *Photonic Crystals: Molding the Flow of Light* (2nd ed.), Princeton University Press, Princeton, Oxford **2008**.

**Appendix B. Engineering low-frequency dielectric function with metamaterial  
plasmonic structures**

The following paper is published in *physica status solidi (RRL)* on 17 January 2018.

Citation information:

Xueyuan Wu, Michael J. Naughton, and Krzysztof Kempa, “Engineering low-frequency dielectric function with metamaterial plasmonic structures”, *physica status solidi (RRL)* **12(3)** 1700291 (2018).

<https://doi.org/10.1002/pssr.201700291>

# Engineering Low-Frequency Dielectric Function with Metamaterial Plasmonic Structures

Xueyuan Wu, Michael J. Naughton,\* and Krzysztof Kempa\*

Metamaterial plasmonic composites offer remarkable flexibility in controlling effective dielectric properties of matter. These composites rely on trapped plasmonic resonances in metallic micro- or nano-structures. Such composites can have very large and/or small effective dielectric functions at various frequencies, depending on the composite design. In the electronics industry, there is a need for so-called high- $k$  materials, which have large (and largely real, to minimize losses) low frequency dielectric function. In this Letter, metamaterial plasmonic composites with inductive elements are demonstrated to function as effective high- $k$  materials, without heavy metal loading, confirming an earlier theoretical study. Moreover, embedding the high- $k$  structures in dielectric or semiconducting matrices can address the parallel need for low leakage current devices.

In macroscopic electrodynamics, the response of a material at radiation frequency  $\omega$  and wave vector  $q$  is described by its electric permittivity or dielectric function  $\epsilon(\omega, q)$  and its magnetic permeability  $\mu(\omega, q)$ . In many applications, materials are needed with large and essentially real  $\epsilon(\omega, q)$  at very low frequencies. These are usually called high- $k$  materials in the engineering literature. One application involves a new generation of thin film transistors (TFT),<sup>[1,2]</sup> which could benefit not only from lower operational gate voltages, but also from reduced carrier-phonon scattering due to large polarization shielding,<sup>[3]</sup> both of which scale to the lowest order with  $1/\epsilon$ .<sup>[3,4]</sup> It has been demonstrated that high- $k$  materials can dramatically increase mobility of charges in high electron mobility transistors (HEMT).<sup>[5,6]</sup>

In the realm of normal materials, there is limited control over  $\epsilon(\omega, q)$ . Metamaterials, on the other hand, offer exceptional flexibility in making composite media with very large or very small effective dielectric constants. Recently, such a metamaterial dielectric composite film, made of aluminum nanospheres, achieved a threefold increase in the superconducting critical temperature of Al as compared to the bulk.<sup>[7]</sup> In this case, the effective dielectric response was designed to have  $\epsilon(\omega, q) \approx 0$  in the frequency of interest (THz). A similar strategy employing metamaterials but aiming instead at large  $\epsilon(\omega, q)$  can be used to

control charge-phonon scattering in thermoelectrics.<sup>[8]</sup> In this paper, we demonstrate that simple, planar metamaterial structures can be designed to have a very large effective  $\epsilon(\omega, q)$  at very low (micro-wave) frequencies. This is achieved not by the usual heavy metal-loading, but rather by inductively lowering the first plasmonic resonance frequency of the effective  $\epsilon(\omega, q)$ .

It can be shown that the local dielectric function of a composite (of volume  $V_0$ ), made of metallic units (of volume  $V_m$ ), embedded in a dielectric matrix with dielectric constant  $\epsilon_\infty$ , is given by<sup>[9,10]</sup>:

$$\epsilon(\omega, 0) \approx \epsilon_\infty + \sum_{m=1}^M \frac{v_m \omega_p^2}{\omega_m^2 - \omega(\omega + i\gamma_m)}, \quad (1)$$

where  $v_m = V_m/V_0$ ,  $\omega_p = \sqrt{4\pi n e^2/m\epsilon}$ ,  $\omega_m$  is the renormalized unit resonance frequency of the corresponding order  $m$  and  $\gamma_m$  characterizes the damping of the composite medium. For vanishingly small frequency, Eq. (1) yields:

$$\epsilon(0, 0) \approx \epsilon_\infty + \omega_p^2 \sum_{m=1}^M \frac{v_m}{\omega_m^2} > \epsilon_\infty. \quad (2)$$

Clearly, to maximize this composite dielectric function, a structure is needed with sufficiently small  $\omega_m$ , which can be achieved by metamaterial/plasmonic engineering. An important physical effect hidden in the universal Eq. (1) is that each resonance (Lorentzian) term is a result of a capacitive-inductive coupled response. For example, below  $\omega_m$ , the response is first dominated by a capacitive character for frequencies much below the resonance ( $\omega \ll \omega_m$ ), but with increasing frequencies, the role of the inductive character increases, and dominates at the resonance. This can be illustrated by the following simple circuit analysis.

Figure 1 shows schematic side views of two metamaterial capacitive units. Both units are defined by two horizontal electrodes (black solid bars) of width  $w'$  and length  $F$  in the  $z$ -direction. The blue color represents the dielectric filling. The unit shown in Figure 1a has a solid metallic insert (black square), and that in Figure 1b has an inductive metallic insert (spiral). Both inserts have the same outside dimensions  $h$ ,  $w$ , and  $l$  (in  $x$ ,  $y$ , and  $z$  directions, respectively). We also assume that  $w' \approx w$ . Let  $C'$  be the capacitance of the unit in (a), and assume that its inductance is negligible. The reactance of the unit in (b) is given approximately by  $X = -i \frac{1}{\omega C_{\text{eff}}} = i\omega L - i \frac{1}{\omega C'}$ , where  $C_{\text{eff}}$  is the effective capacitance of the unit in (b), and  $C' = C/2$  is the

X. Wu, Prof. M. J. Naughton, Prof. K. Kempa  
Department of Physics  
Boston College  
Chestnut Hill, Massachusetts 02467, USA  
E-mail: naughton@bc.edu; kempa@bc.edu

DOI: 10.1002/pssr.201700291

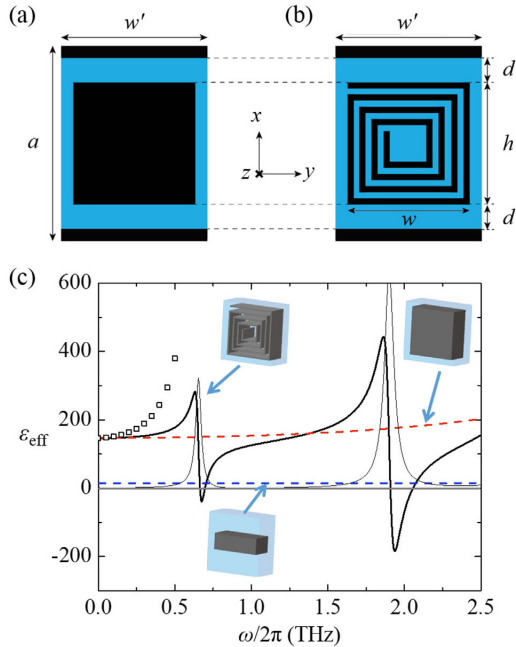


**Figure 1.** Schematics of the simple metamaterial units and corresponding effective dielectric function  $\epsilon_{\text{eff}}$ . a) Capacitor unit with solid metallic insert. b) Unit with spiral metallic insert. Both units and inserts have the same outside dimensions, respectively. In the  $z$ -direction, both units have length  $F$ , and inserts length  $l$ . c) Effective dielectric function  $\epsilon_{\text{eff}}$  versus frequency  $\omega$ , for various simple effective media. Thick solid line represents the real part of  $\epsilon_{\text{eff}}$  of the medium made of units shown in (b). The corresponding imaginary part is shown as the thin solid line. The  $\text{Re}(\epsilon_{\text{eff}})$  of the medium made of units shown in (a) are represented by the red dashed line. The blue dashed line represents  $\text{Re}(\epsilon_{\text{eff}})$  for a medium made of units similar to (a), but with insert having the same volume as the volume of the spiral insert in (b). Black squares represent  $\text{Re}(\epsilon_{\text{eff}})$  calculated from Eq. (3).

capacitance of the two (connected in a series), simple flat capacitors, defined by the gaps of size  $d$  above and below the inserts, in either unit.  $L$  is the inductance of the spiral metallic insert in the unit in (b). The unit in (b) has a resonance frequency  $\omega_r = 1/\sqrt{LC}$ , and we get finally that the effective dielectric function  $\epsilon_{\text{eff}}$  of the effective medium made of the unit shown in Figure 1b, and periodically extended in  $y$  and  $z$  directions, is proportional to  $C_{\text{eff}}$  and therefore is given by:

$$\epsilon_{\text{eff}} = \epsilon'_1 \frac{C_{\text{eff}}}{C} = \frac{\epsilon'_1}{1 - (\omega/\omega_r)^2}, \quad (3)$$

where  $\epsilon'_1$  is the dielectric constant of the effective medium, made of the unit shown in Figure 1a, extended uniformly throughout  $y$ - $z$  space. Note that  $\epsilon_{\text{eff}}$  can be much larger than  $\epsilon'_1$ , and that this effect is entirely due to the inductive contribution from the spiral metallic insert. It is also obvious that in the static limit ( $\omega \rightarrow 0$ ),  $\epsilon_{\text{eff}} = \epsilon'_1$ , and so the metamaterial dielectric function

enhancement is possible only for nonzero frequencies. Conclusions of this simple circuit analysis hold in more rigorous treatments.

To demonstrate the above, we performed finite difference time domain (FDTD) simulations, using CST MW Studio software.<sup>[11,12]</sup> This numerically solves Maxwell's equations for a given distribution of local material parameters  $\epsilon(\omega)$  and  $\mu(\omega)$  inside a given unit, at chosen grid points. Planar emission and absorption ports were defined at two opposing sides of a given unit, along the  $y$ -axis. The emitted source wave is linearly polarized, with the electric field directed along the  $x$ -axis, as required by, for example, a TFT/HEMT geometry. The FDTD simulation provides the complex reflection and transmission coefficients  $r$  and  $t$  of an effective medium obtained by periodically extending (in the  $y$ - and  $z$ -directions) the chosen elementary units. Subsequently, we followed the method of Ref. [13–15] to extract  $\epsilon_{\text{eff}}$  and  $\mu_{\text{eff}}$  from  $r$  and  $t$ . This extraction method works best when the capacitor electrode separation  $a$  and unit cell width  $w$  are much smaller than the wavelength of the radiation employed. This condition is satisfied for all structures used in this work.

The black solid lines in Figure 1c show the extracted effective dielectric function  $\epsilon_{\text{eff}}$  versus  $\omega$  for an effective medium structure based on the unit shown in Figure 1b (see also the corresponding inset in Figure 1c). The thin line represents  $\text{Im}(\epsilon_{\text{eff}})$  and the thick line  $\text{Re}(\epsilon_{\text{eff}})$ . Multiple resonances are clearly visible, as predicted by Eq. (1). The red dashed line represents  $\text{Re}(\epsilon_{\text{eff}})$  of an effective medium made the same way, but based on the unit shown in Figure 1a. For both units, dimensions were chosen to be  $a = 4 \mu\text{m}$  and  $d = 0.2 \mu\text{m}$ , and they were filled with Si ( $\epsilon = 12$ ), conforming again to the TFT/HEMT scenario. The blue dashed line shows  $\text{Re}(\epsilon_{\text{eff}})$  of a medium based on the unit shown in Figure 1a, but with the solid metallic insert much thinner in the  $x$ -direction, so that  $d = 1.5 \mu\text{m}$ . The insert volume in this case is identical to the metal volume of the spiral insert used to simulate the black solid lines.

The squares in Figure 1c represent the qualitative result from Eq. (3) for low frequency. Clearly, the simulated results agree with the simple circuit analysis above (note that the solid thick and the red dashed lines correspond to  $\epsilon_{\text{eff}}$  and  $\epsilon'_1$ , respectively, in the circuit analysis). In particular, at the first resonance,  $\epsilon_{\text{eff}}$  strongly exceeds  $\epsilon'_1$  (by a factor of 2), and for  $\omega \rightarrow 0$  the thick solid line and the red dashed lines converge ( $\epsilon_{\text{eff}} = \epsilon'_1$ ), in full agreement with Eq. (3).

To benefit from the enhanced  $\epsilon_{\text{eff}}$ , one needs to engineer the resonance frequency  $\omega_r$  of the spiral inserts to be in the desired frequency range. As we are guided here by the TFT/HEMT applications, we must lower this frequency to  $\omega_r/2\pi < 0.1 \text{ THz}$  (i.e., 100 GHz). A simple way to accomplish this frequency reduction, while still retaining the device dimension requirements, is to add more turns to the spiral insert. This is obviously subject to material and technological limitations. Another, more practical way is to "stretch" the spiral width  $w$  in the unit of Figure 1b, as shown in Figure 2a. Figure 2b shows the evolution of  $\text{Re}(\epsilon_{\text{eff}})$  versus  $\omega$  as a function of  $w$  (from 20 to 60  $\mu\text{m}$ ) for such a structure. The corresponding color contour plot of the same dependence is shown in Figure 2c, and it demonstrates a linear dependence of  $\omega$  on  $1/w$ , in a large section of the plot (black dashed line). This linear dependence is expected from simple circuit model analysis: since both  $L$  and

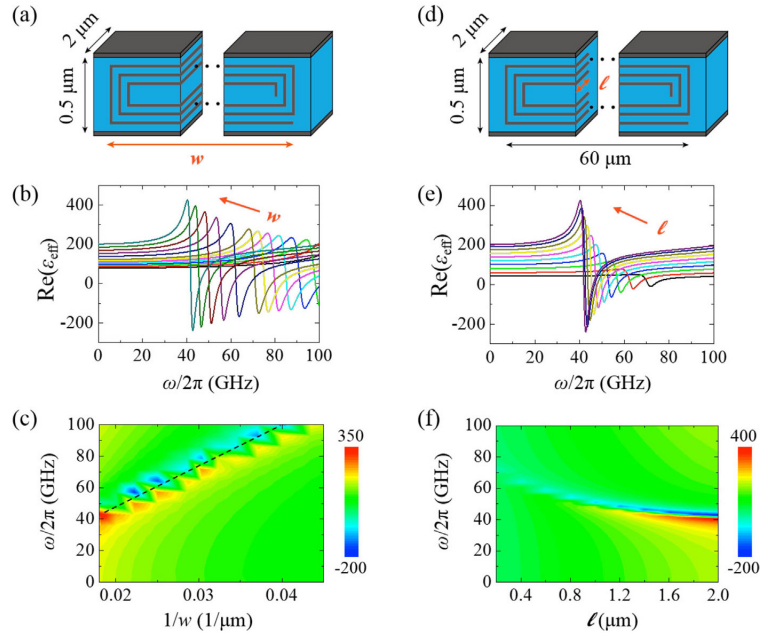


**Figure 2.** Effect of spiral insert. a) Sketch of unit cell emphasizing the parameter  $w$ . b) Evolution of  $\text{Re}(\epsilon_{\text{eff}})$  versus  $\omega$  as a function of  $w$  (tuned from 20 to 60  $\mu\text{m}$ ). c) Color contour plot of  $\text{Re}(\epsilon_{\text{eff}})$  versus  $\omega$  and  $1/w$ . Dashed line is a guide to the eye. d) Sketch of unit cell emphasizing the parameter  $\ell$ . e) Evolution of  $\text{Re}(\epsilon_{\text{eff}})$  versus  $\omega$  as a function of  $\ell$  (tuned from 0.2 to 2  $\mu\text{m}$ ). f) Color contour plot of  $\text{Re}(\epsilon_{\text{eff}})$  versus  $\omega$  and  $\ell$ .

$C'$  of the unit cell scale linearly with  $w$ , the resonance frequency  $\omega_r = 1/\sqrt{LC}$  must scale linearly with  $1/w$ . Note that there is no limit on the  $\omega_r$  reduction, and it can be made very small by simply increasing  $w$ . Guided by geometrical restrictions on typical TFT/HEMT devices, we have assumed  $w_{\text{max}} = 60 \mu\text{m}$ . Figure 2d–f show the effect of changing  $\ell$ , the insert depth along the  $z$ -axis. Figure 2e shows the evolution of  $\text{Re}(\epsilon_{\text{eff}})$  as a function of  $\ell$ , with the corresponding color contour plot shown in Figure 2f. Clearly, while reducing  $\ell$  below  $\ell_{\text{max}} = 2 \mu\text{m}$  (full unit coverage in the  $z$ -direction) strongly affects the resonance strengths, the  $\omega_r$  dependence is slow.

An “optimized” structure, based on the above analysis, which takes into account some of the technological and material constraints, as well as dimensional restrictions of the TFT/HEMT structures, is sketched in Figure 3a. A unit of this structure has dimensions  $a = 0.5 \mu\text{m}$ ,  $w' = 62 \mu\text{m}$ ,  $F = 2 \mu\text{m}$ ,  $h = 0.45 \mu\text{m}$ ,  $w = 60 \mu\text{m}$ , and  $\ell = 1.9 \mu\text{m}$ . Figure 3b shows the spectrum of the extracted  $\epsilon_{\text{eff}}$  for this structure, which has  $\text{Re}(\epsilon_{\text{eff}}) > 180$  in the frequency range 0–40 GHz, with a practical maximum (with sufficiently small  $\text{Im}(\epsilon_{\text{eff}})$ ) as high as 390, at 40 GHz. The enhancement of  $\epsilon_{\text{eff}}$  above 190 is due to the inductive action of the spiral insert. Further enhancement of  $\epsilon_{\text{eff}}$  could be achieved, as discussed above by further increasing  $w$  (if allowed).

Since the enhancement in our structures is inductive, and as shown above quantitatively understandable with the simple circuit analysis, this suggests that further enhancement can be achieved by replacing the flat spiral insert in Figure 1b, with an elongated, multi-turn micro-solenoid as shown in

Figure 3c. The inductance and capacitance of such a solenoid insert can be easily estimated (all parameters defined in Figure 1): the inductance is  $L \simeq \mu\mu_0\pi h^2 nN/4$ , with  $N$  the number of turns, and  $n = N/\ell$  the turn density. Similarly, the capacitance of the unit cell can be roughly estimated as  $C \simeq \epsilon\epsilon_0 w' F/2d$ , where  $d > d'$  is the average (adjustable) electrode-insert distances, as defined in Figure 1. The resulting resonance frequency is given again by  $\omega_r = 1/\sqrt{LC} \sim 1/N$ . For example, with  $a = 0.5 \mu\text{m}$ ,  $w' = 0.5 \mu\text{m}$ ,  $h = 0.45 \mu\text{m}$ ,  $w = 0.45 \mu\text{m}$ ,  $\ell = 0.05 N \mu\text{m}$  ( $N$  ranges from 12 to 40),  $F = \ell$ ,  $d = 25 \text{ nm}$ , a coil wire diameter of 20 nm, with  $d' = 65 \text{ nm}$ ,  $\epsilon = 12$ , and  $\mu = 1$ , we obtain the red line in Figure 3d, which is in excellent agreement with the FDTD simulations (shown as black square dots) for the physical situation. This excellent agreement allows us to predict  $\omega_r$  for much longer solenoid inserts. The inset in Figure 3d shows that one can access the low GHz resonance frequency range with several thousands of solenoid turns, corresponding to  $F \simeq 100 \mu\text{m}$ . Realizations of such micro-solenoids with similar dimensions, and with metal or metal-dielectric wires, have been recently demonstrated using focused ion beam deposition.<sup>[16–18]</sup> The composite spiral medium, with dielectric core shell nanohelix structures, provides one more degree of freedom to tune up the dielectric function.<sup>[18]</sup> Then, based on Eq. (1) and the corresponding theory,<sup>[10]</sup> one could expect strong enhancement of  $\epsilon_{\text{eff}}$  for this composite medium.

The extreme reduction of the resonance frequency expected with the spiral structures opens up a new direction in  $\epsilon_{\text{eff}}$

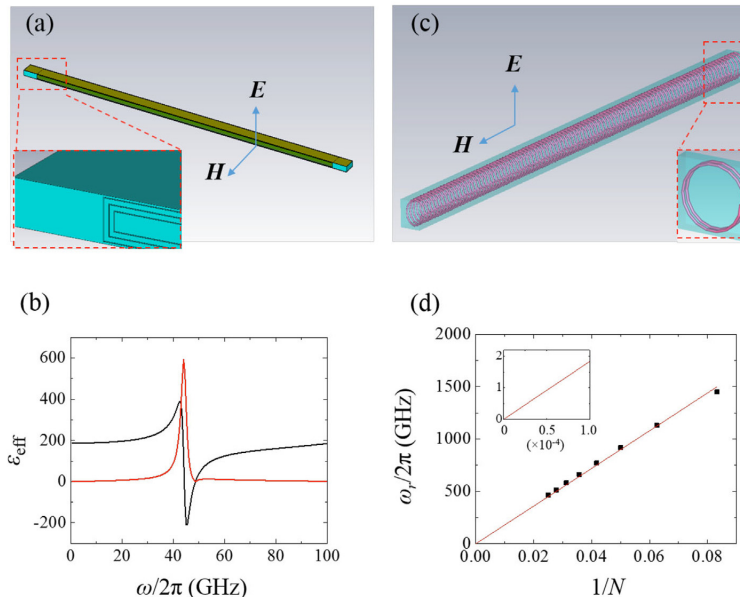


**Figure 3.** Spiral structures for extremely low frequency, high- $k$  applications. a) Schematic of a unit cell of a stretched rectangular spiral structure. The structure is obtained by periodic extension of the unit in the  $y$ - $z$  plane. b) Corresponding dielectric function; black line for real, red line for imaginary parts of  $\epsilon_{\text{eff}}$ . c) Schematic of a unit cell of a micro-solenoid structure, and d) the corresponding plot of  $\omega_r$  versus  $1/N$ . The squares are the FDTD simulations, and the solid line is the result of the simple circuit analysis, with one adjustable parameter. The inset in (d) is a zoom-in of the low frequency regime, with both axes sharing the same units as the main figure.

enhancement. At such low frequencies, ferromagnetic/ferrite materials exist which could be used to further, significantly increase the medium inductance, and therefore  $\epsilon_{\text{eff}}$ . A new generation of high- $\mu$  materials<sup>[19,20]</sup> could allow our scheme to yield effective high- $k$  media with low-loss  $\epsilon_{\text{eff}}$  of many hundreds, in the low-frequency MHz range. Finally, we have confirmed that the choice of background dielectric material, as expected, does not affect the dielectric function enhancement due to the inductive inserts.

In conclusion, we have demonstrated engineering of a low frequency dielectric function with inductive metamaterial-plasmonic structures. To maximize the inductance, we focused on spiral microstructures in a strip, and solenoid configurations as inserts into units of the composite medium. By employing FDTD simulations, we have demonstrated that microstructures of our design can be used to make dielectric media with very large, low-loss, and low-frequency dielectric functions. The largest proposed unit insert is  $\sim 0.5 \mu\text{m}$  in height, and  $< 100 \mu\text{m}$  in length, and thus small enough for some high- $k$  applications, such as TFT. Further improvements are possible with application of high- $\epsilon$  and high- $\mu$  materials; these could reduce the need for very long metallic inserts, and thus expand the parameter space for high- $k$  applications.

### Conflict of Interest

The authors declare no conflict of interest.

### Keywords

dielectric function, high- $k$  materials, inductive resonators, metamaterials, microstructures, plasmonics

Received: August 24, 2017

Revised: January 6, 2018

Published online: January 17, 2018

- [1] R. D. Clark, *Materials* **2014**, *7*, 2913.
- [2] D. Misra, H. Iwai, H. Wong, *Interface* **2005**, *14*, 30.
- [3] G. D. Mahan, *Many Particle Physics*, 3rd edn. Kluwer Academic/Plenum Publishers, New York, USA **2000**.
- [4] C. R. Newman, C. D. Frisbie, D. A. da Silva Filho, J.-L. Bredas, P. C. Ewbank, P. K. R. Mann, *Chem. Mater.* **2004**, *16*, 4436.
- [5] P. D. Ye, B. Yang, K. K. Ng, J. Bude, G. D. Wilk, S. Halder, J. C. M. Hwang, *Appl. Phys. Lett.* **2005**, *86*, 06350.
- [6] J. Du, N. Chen, P. Pan, Z. Bai, L. Li, J. Mo, Q. Yu, *Electron. Lett.* **2015**, *51*, 104.
- [7] V. N. Smolyaninova, K. Zander, T. Gresock, C. Jensen, J. C. Prestigiacomo, M. S. Osofsky, I. I. Smolyaninov, *Sci. Rep.* **2015**, *5*, 15777.
- [8] G. P. Srivastava, *Rep. Prog. Phys.* **2015**, *78*, 026501.
- [9] M. Y. Koledintseva, R. E. DuBroff, R. W. Schwartz, *Prog. Electromagn. Res. (PIER)* **2006**, *63*, 223.
- [10] K. Kempa, *Phys. Rev. B* **2006**, *74B*, 033411.
- [11] K. Yee, *IEEE Trans. Antennas Propag.* **1966**, *14*, 302.
- [12] Computer simulation technology, <https://www.cst.com/>

- [13] D. R. Smith, S. Schultz, P. Markos, C. M. Soukoulis, *Phys. Rev. B* **2002**, 65B, 195104.
- [14] D. R. Smith, J. B. Pendry, *J. Opt. Soc. Am. B* **2006**, 23B, 391.
- [15] D. R. Smith, *Phys. Rev. E* **2010**, 81E, 036605.
- [16] M. Esposito, V. Tasco, F. Todisco, A. Benedetti, D. Sanvitto, A. Passaseo, *Adv. Opt. Mater.* **2014**, 2, 154.
- [17] V. Tascol, M. Esposito, F. Todisco, A. Benedetti, M. Cuscunà, D. Sanvitto, A. Passaseo, *Appl. Phys. A* **2016**, 122A, 280.
- [18] M. Esposito, V. Tasco, F. Todisco, M. Cuscunà, A. Benedetti, M. Scuderi, G. Nicotra, A. Passaseo, *Nano Lett.* **2016**, 16, 5823.
- [19] N. Matsushita, C. P. Chong, T. Mizutani, M. Abe, *J. Appl. Phys.* **2002**, 91, 7376.
- [20] J. Shim, J. Kim, S. H. Han, H. J. Kim, K. H. Kim, M. Yamaguchi, *J. Magn. Magn. Mater.* **2005**, 290-291, 205.

**Appendix C. Tailoring the electron-phonon interaction with metallic plasmonic structures #**

*Xueyuan Wu<sup>‡</sup>, Jiantao Kong<sup>‡</sup>, David Broido, and Krzysztof Kempa<sup>\*</sup>*

Department of Physics, Boston College, Chestnut Hill, Massachusetts 02467, USA

<sup>‡</sup> These authors contributed equally to this work.

<sup>\*</sup> Corresponding author.

# This appendix is a manuscript currently under the review process in *Materials Today Physics*, as of 2019-02-07.

## **ABSTRACT**

The interaction between electrons and phonons governs the intrinsic current flow and resulting heat generation in semiconductors. Increasing power densities in ever-shrinking microelectronics present significant challenges to continued technological advancement. We show that large reductions in the strength of the interaction between electrons and phonons in polar semiconductors can be achieved by exploiting strong "off-resonance" screening from two-dimensional (2D) plasmonic arrays embedded in a nearby insulating layer. By judicious design of the plasmonic layers, remarkably large enhancements of the carrier mobilities and corresponding reductions in joule heating and operating voltage are possible. Examples for GaAs, GaN and MoS<sub>2</sub> based structures are given. Experimental verification of these predicted behaviors could lead to significant improvements in the performance of microelectronic devices.

**Keywords:** electron-phonon interaction, mobility, semiconductors, plasmonics, metamaterials, transport

## 1. Introduction

The interaction between electrons and phonons is ubiquitous in condensed matter physics [1, 2]. For example, it governs the onset of conventional superconductivity, and it limits carrier and heat transport in metals and semiconductors. Since the electron-phonon interaction (EPI) is fixed by material-specific properties such as electron band structure, phonon dispersions, and dielectric properties, tailoring the strength of the EPI is challenging. One way to accomplish this is through screening. However, for the moderate carrier densities typically occurring in doped semiconductors, the EPI remains strong and is a dominant scattering mechanism limiting the mobility in technologically important semiconductors such as GaAs, GaN MoS<sub>2</sub>. Strong screening of the EPI such as what occurs in metals is not possible in semiconductors since such high carrier densities are not achievable and would in any case destroy the functioning of electronic devices. At the same time, as device sizes shrink and device failure from increased thermal loads become an increasingly challenging problem to overcome, the ability to increase carrier mobilities and reduce Joule heating is highly desirable.

Recent work has pointed out the strategy of enhancing mobility in 2D conducting layers by changing the dielectric environment [3, 4]. This was accomplished through insertion of adjacent materials with high dielectric constants. However, enhancement is achieved only when carrier interactions with ionized impurities are the dominant scattering mechanism. For clean samples where transport is controlled by electron-phonon scattering, it was shown that insertion of high dielectrics actually reduces mobility [4]. For next-generation devices, where high-quality samples can be fabricated with low

concentrations of charged defects, alternative schemes will be needed to improve device performance.

Here we propose a different approach based on the use of metal plasmonic structures to significantly weaken the EPI in polar semiconductors. Below, we present transport and electromagnetic response calculations demonstrating that large increases in mobility and reductions in Joule heating are possible in such structures, with specific examples given for GaAs, GaN, and MoS<sub>2</sub>-based transistor devices.

The idea is to achieve enhanced carrier screening from a two-dimensional array of metallic plasmonic structures embedded in an insulating layer arranged near a region of current flow in a neighboring semiconductor material. The 2D plasmonic structures act as resonators whose resonant frequencies and oscillator strengths can be tuned by the geometry and arrangement of the structures. Engineering the plasmonic resonance frequencies to lie well above those of the phonons minimizes their thermal excitation as well as their coupling to polar phonons and plasmons from the electron gas in the semiconductor layer. Then, tailoring the resonances themselves to be strong gives a large non-resonant tail in the effective dielectric function of the plasmonic structure that provides significantly enhanced dynamic screening of the electron-phonon interaction compared to that from the background dielectric constant of the semiconductor.

## **2. Results**

### **2.1 Effective dielectric function.**

The top left and right diagrams in Figure 1a show schematics of an envisioned integrated circuit and high mobility field-effect transistor, with plasmonic metallic structures (pink) embedded in a dielectric substrate (yellow). A subsequent magnification (Figure 1b)

shows the 2D homogeneity of the interaction region: electrons moving in the planar channel directly above the plasmonic structure experience essentially a constant dielectric environment, apart from the narrow gaps between the metal units. These gap regions can be minimized to increase the plasmonic shielding and improve the overall uniformity of the structure. The in-plane uniformity of the plasmonic structure allows for an effective medium dielectric treatment of the electron-phonon scattering process. The basic physics can be described approximately as follows. The propagating phonon waves in a polar medium scatter electrons in the channel. The scattering process is subject to screening effects as described by a dielectric response [5]. To calculate the dielectric function produced by the plasmonic structure, one could simply consider charges induced on the surface of the plasmonic structure by a propagating phonon wave. Using a Fresnel optics analysis, the field of the reflected wave from these induced interface charges, which can be considered a polarization field produced by the plasmonic structure, has the approximate form at the location of the 2DEG:

$$\vec{P}(\vec{q}, h'; \omega) \approx \vec{E}^{inc}(\vec{q}, \omega) \alpha'(q_z^{ref}) e^{-iq_z^{ref} h'} \approx \vec{E}^{inc}(\vec{q}, \omega) \alpha(Q) e^{-Qh'} \quad (1)$$

where  $\vec{E}^{inc}(\vec{q}, \omega)$  is the field of the incoming phonon wave impinging on the metal surface, and  $q_z^{ref} = \sqrt{\omega^2 n^2 / c^2 - Q^2} \approx iQ$ , where  $n$  is the refractive index of the plasmonic structure, and  $Q$  is the in-plane component of  $\vec{q}^{ref}$ . The distance,  $h' = h + d/2$  is that from the plasmonic structure to the center of the 2DEG of thickness,  $d$ , as shown in Figure 1. With the polarization field given by Eq. 1, the effective dielectric function at the 2D electron gas shows an exponential form (See Methods):

$$\varepsilon_{eff}(Q, \omega) \approx \varepsilon_\infty + \alpha(Q) e^{-Qh} \approx \frac{1}{2} \left\{ \varepsilon_m(Q, \omega) e^{-Qh} + \varepsilon_\infty (2 - e^{-Qh}) \right\} \quad (2)$$

Where  $\varepsilon_m(Q, \omega)$  is the dielectric function of the plasmonic structure and  $\varepsilon_\infty$  that of the semiconductor/insulator dielectric medium. The quantity  $\alpha(Q)$  is chosen so that Eq. 2 satisfies the required  $h \rightarrow 0$  limit of a simple average of polarization contributions from neighboring regions:  $\varepsilon_{eff}(0, \omega) = \frac{1}{2} \{ \varepsilon_m(0, \omega) + \varepsilon_\infty \}$  and it recovers the  $h \rightarrow \infty$  limit i.e.

$\varepsilon_\infty$ . Equation 2 is quite general, and can be derived by a variety of methods. Our Finite Difference Time Domain (FDTD) simulations, described in the Methods section confirm the evanescent nature of the reflected field as given in Equation 1.

For the cases considered in the present work, we approximate the 2D plasmonic structure dielectric function by its long wavelength limit:  $\varepsilon_m(Q, \omega) \approx \varepsilon_m(0, \omega)$ . The justification for this approximation is given in the Methods section and Ref. [6]. Then,  $\varepsilon_m(0, \omega)$  in turn can be extracted from a plane wave analysis and FDTD simulations of the metallic structure in the retarded limit [7-9].

Figure 2 shows an example of the real and imaginary parts of the dielectric function for a square-ring metallic structure made of gold (Fig. 1c) obtained from FDTD simulations using the CST software [7-9]. A GaN dielectric background is taken. There are several features of this 2D plasmonic dielectric function,  $\varepsilon_m(0, \omega)$ , worth noting: (i) Unlike the longitudinal plasmons in a continuous metal, the confined plasmons of the 2D metallic structures have a sharp resonance; (ii) The frequency and strength of this resonance can be tuned by adjusting the shapes and sizes of these structures; (iii) Structure designs for which the plasmonic resonance is strong and with frequency well above the phonon frequency range to minimize plasmon-phonon mode coupling but still close enough to

give a large off-resonance tail in the frequency range of the phonon modes can weaken significantly the EPI, as will be discussed below.

## 2.2 Electron Transport and Carrier Screening.

We consider carrier transport to occur in a thin conducting channel in a semiconductor near the interface with an insulating layer in which the plasmonic structure is embedded, as shown in Figure 1. The total dielectric function can be approximated by

$$\varepsilon_{tot}(Q, \omega) = \varepsilon_{el}(Q, \omega) + \varepsilon_{ph}(Q, \omega) + \varepsilon_{eff}(Q, \omega) \quad (3)$$

The first term on the right-hand side of Eq. 3 is the dielectric function of the electron gas in the semiconductor:  $\varepsilon_{el} = \varepsilon_{\infty} - v_Q P(Q, \omega)$ , where  $v_Q = 2\pi e^2 / Q$  and  $P(Q, \omega)$  is the polarization of the 2D electron gas. We take this screening to be described by a 2D Thomas-Fermi model:  $\varepsilon_{el}(Q) = \varepsilon_{\infty} (1 + Q_{TF} / Q)$ , where  $Q_{TF}$  is the 2D Thomas-Fermi screening wave vector. The second term is for the optic phonons [5]:

$$\varepsilon_{ph} = \varepsilon_{\infty} \left( \frac{\omega_{LO}^2 - \omega^2}{\omega_{TO}^2 - \omega^2} \right).$$

For simplicity, we have assumed dispersionless

longitudinal optic (LO) and transverse optic (TO) phonons having frequencies  $\omega_{LO}$  and  $\omega_{TO}$ , respectively. The third term gives the plasmonic structure contribution from Eq. 2. It can be combined with the first term into an effective electronic dielectric function:

$$\varepsilon_{el}^{eff}(Q, \omega) \equiv \varepsilon_{el}(Q, \omega) + \varepsilon_{eff}(Q, \omega).$$

The plasmonic structure provides dynamic screening of the EPI in the range of frequencies of the phonon field i.e.  $0 < \omega < \omega_{LO}$ . Even though this frequency range is far below the resonant frequency of the plasmonic structure, the electrons on the surface of the metallic plasmonic structure are still highly polarizable, as seen by the significant

enhancement of the real part of the dielectric function,  $\varepsilon_m(0, \omega)$ , for  $\omega < \omega_{LO}$  in Fig. 2 compared to the background dielectric constant of the semiconductor,  $\varepsilon_\infty$ , which normally screens the EPI. The example for GaN in Fig. 2 shows that  $\varepsilon_m(0, \omega)$  is over ten times that of  $\varepsilon_\infty = 5.35$  for bulk GaN.

The electron-phonon scattering probability can be written in the Random Phase approximation (RPA) as [5]:

$$S^{el-ph}(\mathbf{k}, \mathbf{k}') = \frac{2\pi}{\hbar} \frac{|M_{el-ph}(\mathbf{k}, \mathbf{k}')|^2}{|\varepsilon_{el}^{eff}(Q, \omega)|^2} \delta(\varepsilon_{k'} - \varepsilon_k \pm \hbar\omega_\lambda) \quad (4)$$

where  $M_{el-ph}(\mathbf{k}, \mathbf{k}')$  is the matrix element describing the EPI, which is screened by the electronic part of the dielectric function,  $\varepsilon_{el}^{eff}(Q, \omega)$ ;  $\varepsilon_k$  is the electron energy in the semiconductor layer with 2D wave vector  $\mathbf{k}$ ,  $\hbar\omega_\lambda$  is the phonon energy in mode  $\lambda$  and the  $\pm$  signs refer to phonon emission and absorption, respectively (See SI Appendix, Supplementary Note 2). The electron-phonon scattering rates are sums of  $S^{el-ph}(\mathbf{k}, \mathbf{k}')$  across the phonon frequency range. The increase of the  $\varepsilon_m(0, \omega)$  throughout this range reduces electron scattering and gives a corresponding enhancement to mobilities. Since the dielectric function of the plasmonic metallic structure hardly changes in the frequency range of the phonons, to good approximation, we can take it to be a constant in this frequency range. For convenience, we take this constant to be the zero-frequency value, labeling this value as  $\varepsilon'_\infty$ . Then the effective electronic dielectric function can be written:

$$\varepsilon_{el}^{eff}(Q, \chi, h') \approx \varepsilon_{\infty} \left[ \frac{Q_{TF}}{Q} + \frac{1}{2} (2 - e^{-Qh'} + \chi e^{-Qh'}) \right] \quad (5)$$

where  $\chi = \varepsilon'_{\infty} / \varepsilon_{\infty}$  defines a screening enhancement factor. If the 2D plasmonic structure is far from the electron gas ( $h' \rightarrow \infty$ ), the Thomas-Fermi dielectric function is recovered. If the plasmonic structure is sufficiently close to the conducting channel that  $Qh' \ll 1$ , then  $\varepsilon_{el}^{eff}(Q, \chi) = \varepsilon_{\infty} [(1 + \chi) / 2 + Q_{TF} / Q]$ .

This is the central result of the present work. It shows that the screening of the polar interaction between carriers and phonons is controlled by the oscillator strength and resonance frequency of the plasmonic structures and the distance of these structures from the conducting channel. Engineering  $\chi$  to be large and  $Qh'$  to be small can significantly enhance carrier mobilities and reduce joule heating.

### 2.3 Mobility enhancement.

The carrier mobility for 2D electron transport from an applied DC electric field parallel to the layer is calculated by solving the Boltzmann transport equation [10-13]. In the model calculations, carriers in the polar semiconductor are scattered by phonons through deformation potential, piezoelectric and Frölich interactions. [1, 2, 10, 11]. Expressions for the scattering rates have been given in previous publications [14, 15] and they along with the Boltzmann equation solution and mobility expression are included in the SI Appendix, Supplementary Note 2. Using this model, we find room temperature bulk mobilities for low carrier concentration ( $\sim 10^{13} \text{cm}^{-3}$ ) of  $8580 \text{ cm}^2 \text{V}^{-1} \text{s}^{-1}$   $1870 \text{ cm}^2 \text{V}^{-1} \text{s}^{-1}$  for GaAs and GaN, respectively, and 2D mobility of  $450 \text{ cm}^2 \text{V}^{-1} \text{s}^{-1}$ , for an MoS<sub>2</sub> layer, which are in good agreement with previously calculated values [15-17]. Parameters used are given in the SI Appendix, Supplementary Note 3. The measured room temperature GaAs

mobilities [16, 18-20] are close to the one calculated here, while for GaN, the calculated values are about 25% smaller than measured [21] possibly due to impurities and sample defects whose effect is not included in the calculations. Measured mobilities for MoS<sub>2</sub> monolayers are lower than calculated, again possibly because of the strong scattering from interface defects [15, 22].

The calculated room temperature mobilities, for a 1 nm thick quasi-2D GaAs layer near the metallic structures are shown in Figure 3 as a function of the distance from the center of the conducting layer to the metal,  $h'$ , for an electron concentration of  $10^{11} \text{ cm}^{-2}$  and for different values of screening enhancement factor,  $\chi$ . This mobility is scaled by that for the 2D electron gas without the metallic structure, at the same concentration. Scattering by ionized impurities and sample defects is not included. As  $h'$  decreases, remarkably large mobility enhancements are achieved with increasing  $\chi$ . Specifically, mobility enhancements of 5, 14, 28 and 96 are achieved at  $h'=1 \text{ nm}$  for  $\chi=5, 10, 15$  and  $30$ , respectively. These large enhancements reflect the increasingly strong screening from the plasmonic structure as it approaches the GaAs layer. Increasing the carrier density from  $10^{11} \text{ cm}^{-2}$  to  $10^{12} \text{ cm}^{-2}$  reduces the relative enhancement, but this reflects mainly the increase in the mobility of the 2D layer without the plasmonic structure resulting from the free carrier (Thomas-Fermi) screening: The absolute mobilities for small  $h$  and large  $\chi$  are relatively insensitive to the electron density. Also, there is little change in the mobility for the GaAs layer when the temperature is increased above 300K. Similar qualitative behavior is seen for a GaN structure (Figure 4) and for an MoS<sub>2</sub> monolayer (Figure 5), with mobility enhancements of over an order of magnitude found for small  $h$  and large  $\chi$ .

The screening of the EPI decays rapidly as the plasmonic structure is moved away from the 2DEG, with no mobility enhancement beyond 10 nm. Furthermore, the mobility enhancement in GaAs is larger than that in GaN. These features can be understood as follows. The deformation potential and piezoelectric interactions between carriers and acoustic phonons are a nearly elastic process [1, 2]. Then, the in-plane phonon wave vector magnitude,  $Q = \sqrt{2}k(1 - \cos \theta)$  where  $\theta$  is the angle between incident and final electron wave vectors of magnitude  $k = \sqrt{2m^* \varepsilon / \hbar^2}$ , with  $\varepsilon$  being the electron energy. Taking  $\varepsilon \propto k_B T$  as a rough scaling of the average carrier energy, the angle-averaged phonon wave vector  $Q_{ave} = \sqrt{4m^* k_B T / \hbar^2}$ , which gives  $Q_{ave} = 0.3 \text{ nm}^{-1}$  ( $0.5 \text{ nm}^{-1}$ ) for GaAs (GaN). When a plasmonic structure with large  $\chi$  is near the 2DEG, then the effective electronic dielectric function, from Eq. 5, becomes  $\varepsilon_{el}^{eff} \approx \chi \exp(-Q_{ave} h') / 2$ . It is straightforward to show that the mobility including the plasmonic structure will then be scaled by the square of this factor:  $\chi^2 \exp(-2Q_{ave} h') / 4$ . Thus, the decay length of the mobility enhancement from its maximum value of  $\chi^2 / 4$  is  $\sim 1/Q_{ave}$ , which is increased for small effective mass (e.g. GaAs) and for low temperature. We note that the  $Q_{ave}$  calculated for the inelastic scattering for the Frölich interaction has similar values as those calculated above for acoustic phonon scattering. Using this scaling, the room temperature mobility enhancement for GaAs with electron density of  $10^{11} \text{ cm}^{-2}$  and  $\chi=15$  is plotted as the dotted blue curve in Fig. 3, and it shows good agreement with that for the full calculation (solid blue curve) for small distances.

### 3. Discussion

#### 3.1 Reduction of Joule heating and device operating voltage.

The power generated from Joule heating is  $I^2R$ . Resistance,  $R$ , is inversely proportional to the mobility. For a constant current,  $I$ , through an electronic device, the large predicted mobility enhancements shown for GaAs, GaN and MoS<sub>2</sub> translate directly into corresponding reductions in Joule heating. Furthermore, since  $I$  is proportional to mobility, the mobility enhancement assures that a given  $I$  can be achieved for a significantly reduced driving voltage.

### 3.2 Structure design considerations.

To maximize mobility enhancement, structures should be designed with a strong plasmonic resonance to give large off-resonance dielectric response in the phonon frequency range. At the same time, keeping the plasmonic resonance frequency well above the phonon frequency range minimizes plasmon-phonon mode coupling. These considerations and large metal coverage motivated the choice of the specific structure and dimensions shown in Fig. 1c for the case of GaN. The effective background dielectric constant in the energy range of the GaN phonons ( $\omega < 92$  meV) ranges from 65 to 75. The corresponding 2D screening enhancement factors  $\chi$  are between 12 and 14 for background dielectric constant of GaN,  $\epsilon_\infty = 5.35$ , consistent with the middle curves in Figures 3, 4 and 5. We note that since a strong plasmonic resonance is essential to achieve large low frequency dielectric response, the required structures necessarily will have large quality factors. Furthermore, placement of the metallic structures near the semiconductor and strong confinement of the electron gas are also desirable to optimize the screening of the EPI.

To estimate the effect of the coupling of the plasmonic mode at frequency  $\omega_0$  and the LO phonon mode for the GaN example, we have calculated the shifted frequencies of due to

coupling using analytical expressions [23, 24]. These are:  $\omega_+ = \omega_0 + \Delta\omega_+$  and  $\omega_- = \omega_{LO} - \Delta\omega_-$ . We find  $\Delta\omega_+ \approx 3$  meV (i.e. the plasmonic resonance is shifted up by around 1%) while  $\Delta\omega_- \approx 12$  meV (i.e. the LO phonon resonance shifts down by  $\sim 13\%$ ). Incorporating the lower frequency of the coupled LO phonon mode into the transport calculations gives only a slight increase in the calculated mobility ( $\sim 5\%$ ) when the plasmonic structure is close to the electron gas of the semiconductor, confirming the weak coupling. It has been noted previously that scattering between carriers and plasmons should not degrade an electric current [24, 25] since quasi-momentum is conserved in the scattering processes. Therefore, the mobility should not be affected by this scattering. In real devices carriers also scatter from impurities and defects such as occur at interfaces. Minimizing the presence of such defects would optimize the predicted mobility enhancement and corresponding reduction in Joule heating.

The physical size required for the metallic units of the plasmonic structure is dictated by the phonon frequency range. The plasmonic resonance shown in Fig. 2 in the range of hundreds of meV was achieved here using the units in the micron size range. Increasing (decreasing) the sizes of these units will lower (raise) the resonance frequency. Typical channel lengths in electronic devices are a few microns [26] a few times larger than the  $1\mu\text{m}$  size of the 2D plasmonic unit shown in Figure 1c. With shrinking device sizes, the conducting channels could become smaller than  $1\mu\text{m}$ . Placing the 2D plasmonic structure on the opposite side from the gate, source and drain allows reduction of the channel length while still maintaining the strong screening effect and corresponding mobility enhancement. However, fabrication limitations may ultimately require different

placement. An alternative arrangement with metallic units embedded in the spacer layer is shown in Fig. S2 of the SI Appendix, Supplementary Note 4.

### 3.3 Conclusion

From transport and electromagnetic response calculations for GaAs, GaN and MoS<sub>2</sub> systems, we have demonstrated that screening of the electron-phonon interaction in polar semiconductor layers by 2D metallic plasmonic structures can lead to exceptionally large enhancements in carrier mobility and corresponding reduction in Joule heating. Further optimization of the design of the metallic structures beyond that presented here as well as volumetric enhancements such as might be obtained in 1D device geometries could yield even larger mobility increases, with corresponding improvements in device performance.

## 4. Methods

### 4.1 Exponential screening of the plasmonic field and FDTD simulations.

In the scattering calculations we employed Eq. (1) to obtain the effective dielectric function in the 2DEG from the plasmonic structure. The exponential behavior in Eq. 1 is expected from Fresnel optics, which considers any system as a collection of uniform regions, with fields properly matching at each interface. In this spirit, the electric field in the uniform region outside the metal-semiconductor interface has the following spatial dependency  $\vec{E}(\vec{q}, \omega) \sim e^{i\vec{q}\cdot\vec{r} - i\omega t} \sim e^{iq_z z}$ . Since typical values of the wave vectors assure that  $Q^2 \gg \omega^2 n / c$ , the evanescent behavior, as included in Eq. (1) of the main text emerges, since then  $q_z = \sqrt{\omega^2 n / c^2 - Q^2} \approx iQ$ .

We have employed FDTD (finite difference time domain) simulations to confirm this evanescent field decay. The method solves the partial differential Maxwell's equations to

obtain the electromagnetic response to pre-defined boundary conditions. Using the central-difference approximation, the Maxwell's equations are discretized in both space and time [27, 28]. We have employed the commercial FDTD software package made by CST (computer simulation technology) [9]. We simulated a response of the flat metal–dielectric interface to an oscillating dipole placed in the semiconductor (frequency = 10 THz, dipole of length  $l = 50$  nm, and diameter  $d = 11$  nm) a distance  $h = 10$  nm away from the interface (see Figure S1 in the SI Appendix, Supplementary Note 1). The metal (gold) was modeled by the Drude response with conductivity  $\sigma = 4 \times 10^7$  S/m [29], and the permittivity of the semiconductor (GaN) was set to 9.5 [30]. A plot of the absolute amplitudes of the electric fields plotted vs distance is shown in the Supplementary section. In fact, the degree of the decay is exactly as expected. The dipole produces a wave with a wavelength roughly  $2l = 100$  nm, and thus the e-fold reduction of the evanescent field occurs at  $1/Q = l/\pi = 16$  nm, which indeed is roughly the case shown in the (red curve of the semiconductor side). This confirms the form of Eq. (1). The exponential decay is general and holds for the larger  $Q_{\text{ave}}$  values given above.

#### **4.2 Justification for using long wavelength dielectric response for plasmonic structures.**

For the cases considered in the present work, it is helpful to approximate the 2D plasmonic structure dielectric function  $\varepsilon_m(Q, \omega) \approx \varepsilon_m(0, \omega)$ . Then,  $\varepsilon_m(0, \omega)$  in turn can be extracted from a plane wave analysis and FDTD simulations of the metallic structure in the retarded limit [7-9] and fit to a Lorentzian form

$$\varepsilon_m(0, \omega) = \varepsilon_b + \frac{\omega_p^2}{\omega_0^2 - \omega(\omega + i\gamma)} \quad (6)$$

where  $\omega_0$  is the plasmonic structure resonance,  $\omega_p$  is the corresponding strength of that resonance,  $\gamma$  is a broadening parameter, and  $\varepsilon_b$  is the background dielectric constant from the bound electrons metals, all obtained from the fit. In principle,  $\varepsilon_m(0, \omega)$  can be analytically continued into the corresponding non-local form  $\varepsilon_m(Q, \omega)$ .

This analytical continuation can be accomplished [6] by renormalization of  $\omega_0$  as follows

$$\varepsilon_m(q, \omega) = \varepsilon_b + \frac{\omega_p^2}{\omega_0^2 A(q) - \omega(\omega + i\gamma)} \quad (7)$$

where  $A(q) = 1 - aq + bq^2$ , where  $q$  is the isotropic wave vector amplitude. It was shown in Ref. 7, that for most plasmonic metals  $A(q)$  remains of order one, even for  $q$  approaching the Brillouin zone. Thus, to zero<sup>th</sup> order one can ignore the  $Q$ -dependency of  $\varepsilon_m(Q, \omega)$ .

#### **Author Contributions:**

K.K. and D.B. conceived and developed the idea. X.W. performed FDTD simulations, and J.K., under directions of K.K. developed initial model calculations of scattering in the presence of plasmonic structures. D.B. performed transport calculations. D.B. and K.K. wrote the manuscript and supervised the research. All authors provided critical input to this project.

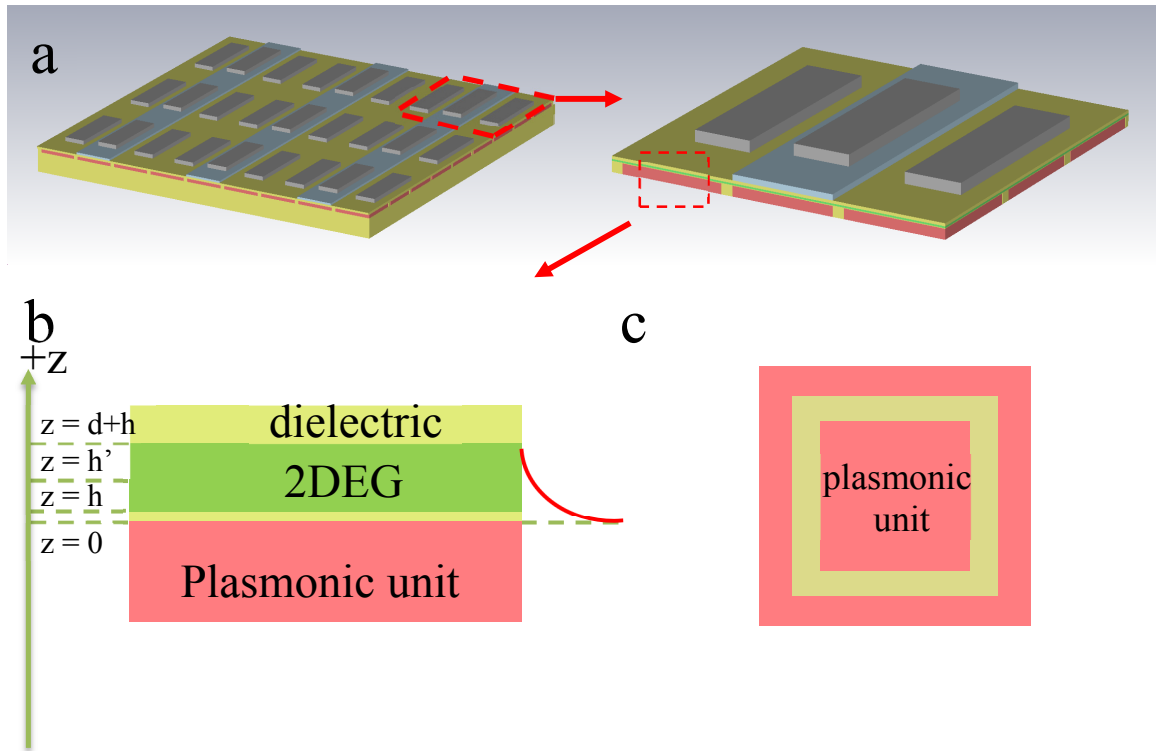


**Fig. 1.** (a) Schematic of a possible integrated circuit (top left) and field effect transistor (top right), with plasmonic metallic structure fragments (pink) shown embedded in the substrate dielectric (yellow), (b) The electron-phonon interaction region, as described in text. Green region represents the 2D electron gas separated from a unit in the plasmonic structure by a distance,  $h$ . Simulated electric field .vs. distance away from the plasmonic unit is indicated by the red curve to the right; (c) A gold plasmonic structure unit with 1 micron square bar unit cell.

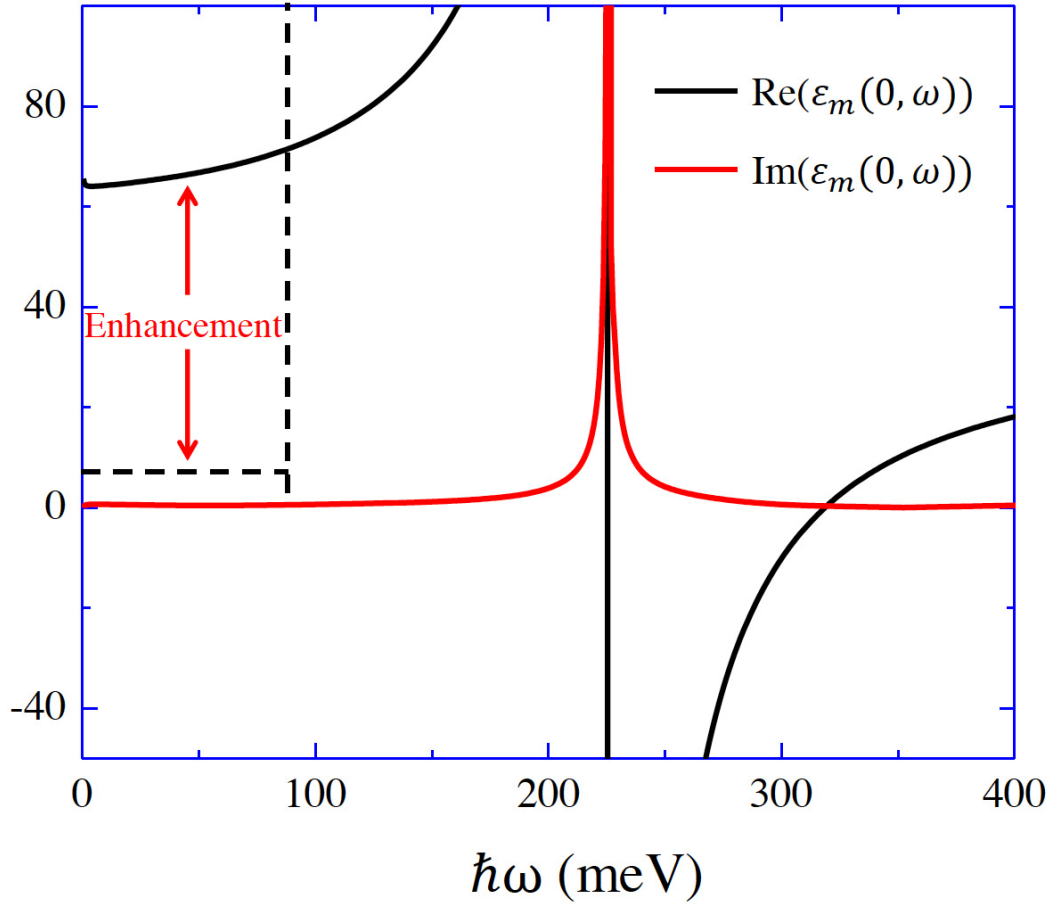


**Fig. 2.** The extracted real and imaginary parts of the dielectric function,  $\varepsilon_m(0, \omega)$ , for a gold plasmonic structure with the  $1\mu\text{m}$  square-bar unit cell shown in Fig. 1c using a GaN dielectric as the background material, modeled in FDTD simulations. Large dielectric enhancement in the frequency range of the GaN phonons (below vertical dashed line) occurs compared to the background dielectric constant of GaN ( $\varepsilon_\infty = 5.35$ , horizontal dashed line).

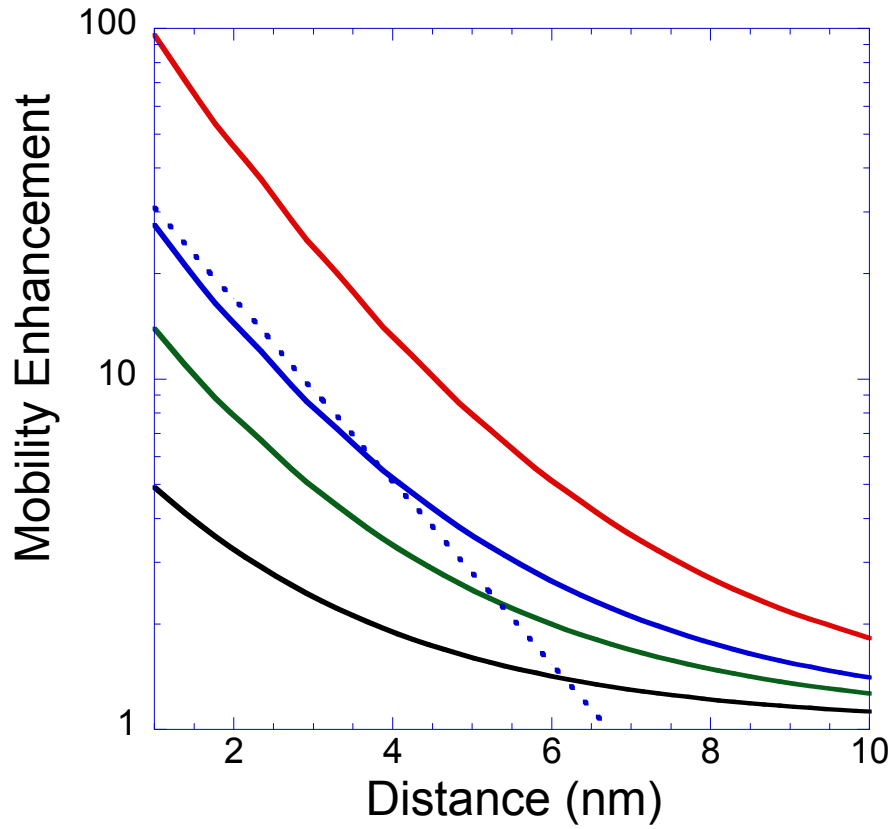


**Fig. 3.** Room temperature mobility of a 1 nm thick GaAs layer near a 2D metallic plasmonic structure as a function the distance from the center of the layer ( $h'=h+d/2$ ). A 2D electron density of  $10^{11} \text{ cm}^{-2}$  is taken. This mobility is scaled by the mobility calculated for the same GaAs layer but without the metallic structure. Results are shown for four different screening enhancement factors,  $\chi=5$  (black curve),  $\chi=10$  (green curve),  $\chi=15$  (blue curve) and  $\chi=30$  (red curve), as defined in the text. Dotted blue curve is for the approximation described in the text with  $\chi=15$ .

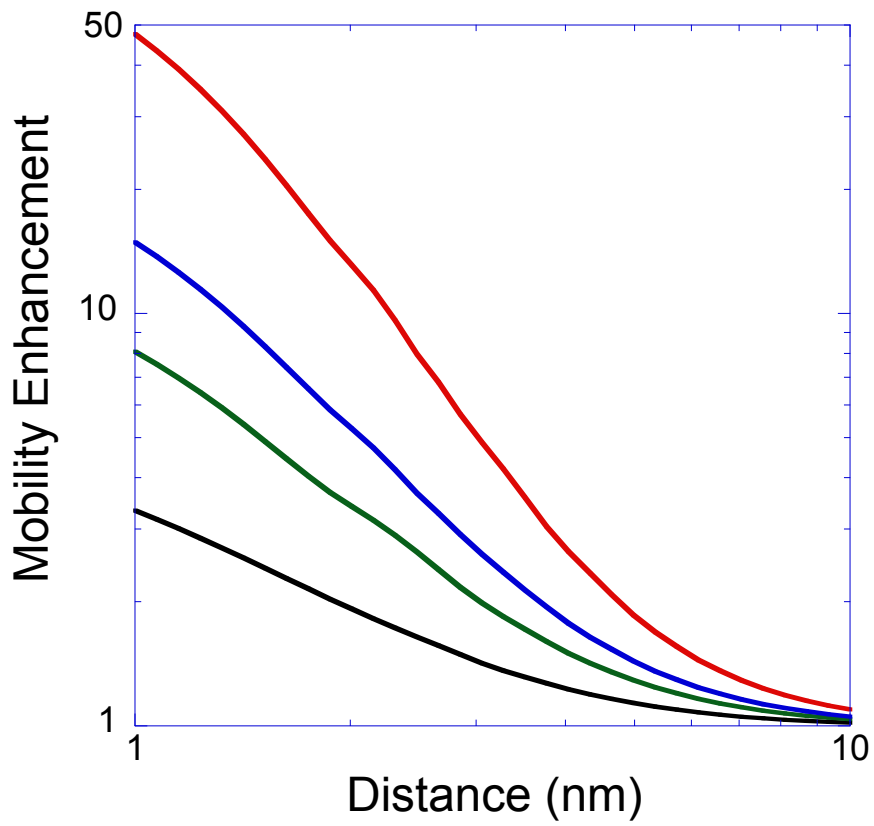


**Fig. 4.** Scaled room temperature mobility of a 1 nm thick GaN 2DEG layer with electron density of  $10^{11} \text{ cm}^{-2}$  as a function of the distance from a 2D periodic metallic structure, as in Figure 3.

Black, green, blue and red curves are for  $\chi=5, 10, 15$  and  $30$ , respectively.

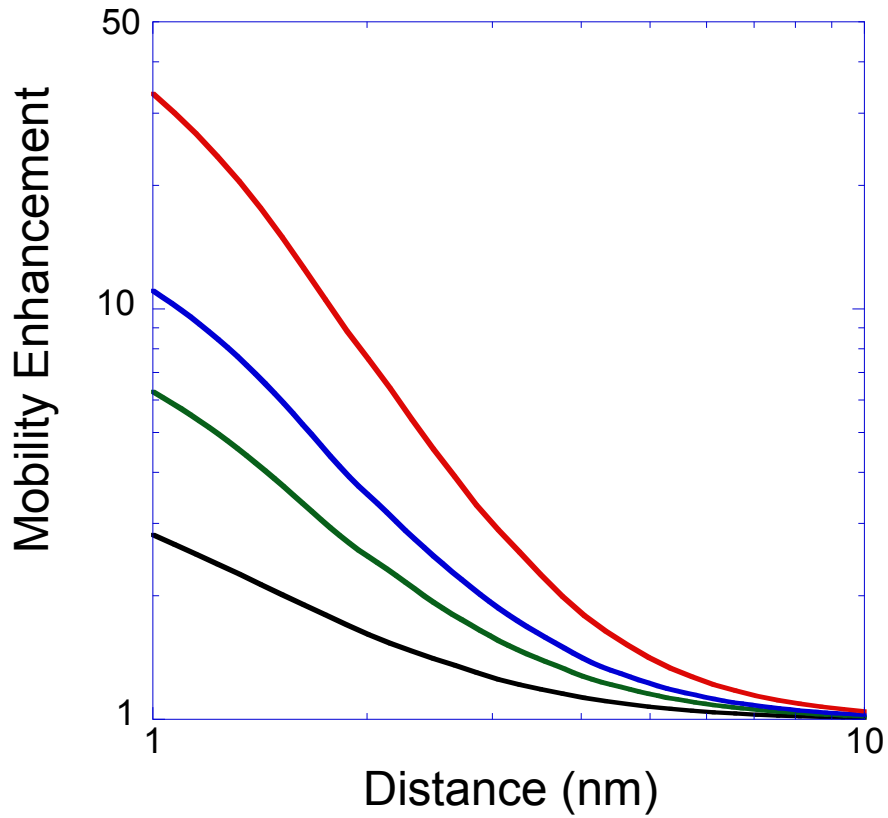


**Fig. 5.** Scaled room temperature mobility of a monolayer of MoS<sub>2</sub> with electron density of  $10^{11} \text{ cm}^{-2}$  as a function of the distance away from the 2D plasmonic structure of Fig. 1c in the main text, as in Figures 2 and 3. Black, green, blue and red curves are for screening enhancement factor (defined in main text),  $\chi=5, 10, 15$  and  $30$ .

## References:

- [1] J. M. Ziman, Principles of the Theory of Solids, 2nd ed., Cambridge University Press, 1972.
- [2] N. W. Ashcroft, N. D. Mermin, ND, Solid State Physics, 1st ed., Holt, Rinehart and Winston, New York, 1976.
- [3] D. Jena, A. Konar, Enhancement of Carrier Mobility in Semiconductor Nanostructures by Dielectric Engineering, Phys. Rev. Lett. 98 (2007) 136805.  
<https://doi.org/10.1103/PhysRevLett.98.136805>.
- [4] N. Ma, D. Jena, Charge Scattering and Mobility in Atomically Thin Semiconductors, Phys. Rev. X 4 (2014) 011043. <https://doi.org/10.1103/PhysRevX.4.011043>.
- [5] G. D. Mahan, Many-Particle Physics, 3rd ed., Springer US, New York, 2000.
- [6] A. J. Shvonski, J. Kong, K. Kempa, Nonlocal extensions of the electromagnetic response of plasmonic and metamaterial structures, Phys. Rev. B 95 (2017) 045149.  
<https://doi.org/10.1103/PhysRevB.95.045149>.
- [7] D. R. Smith, S. Schultz, P. Markoš, C. M. Soukoulis, Determination of effective permittivity and permeability of metamaterials from reflection and transmission coefficients Phys. Rev. B 65 (2002) 195104. <https://doi.org/10.1103/PhysRevB.65.195104>.
- [8] D. R. Smith, B. Pendry, Homogenization of metamaterials by field averaging J. Opt. Soc. Am. B 23 (2006) 391. <https://doi.org/10.1364/JOSAB.23.000391>.
- [9] <https://www.cst.com/>
- [10] B. R. Nag, Electron Transport in Compound Semiconductors, Springer-Verlag, Berlin, 1981.
- [11] D. L. Rode, Semiconductor and Semimetals, Vol. 10, Elsevier, Amsterdam, 1975.
- [12] P. K. Basu, B. R. Nag, Lattice scattering mobility of a two-dimensional electron gas in GaAs Phys. Rev. B 22 (1980) 4849. <https://doi.org/10.1103/PhysRevB.22.4849>.
- [13] T. Kawamura, S. Das Sarma, Phonon-scattering-limited electron mobilities in  $\text{Al}_x\text{Ga}_{1-x}\text{As}/\text{GaAs}$  heterojunctions Phys. Rev. B 45 (1992) 3612.  
<https://doi.org/10.1103/PhysRevB.45.3612>.
- [14] P. J. Price, Two-dimensional electron transport in semiconductor layers. I. Phonon scattering Annals of Physics 133 (1981) 217-239. [https://doi.org/10.1016/0003-4916\(81\)90250-5](https://doi.org/10.1016/0003-4916(81)90250-5).
- [15] K. Kaasbjerg, K. S. Thygesen, K.W. Jacobsen, Phonon-limited mobility in n-type single-layer  $\text{MoS}_2$  from first principles Phys. Rev. B 85 (2012) 115317.  
<https://doi.org/10.1103/PhysRevB.85.115317>.
- [16] D. Rode, S. Knight, Electron Transport in GaAs, Phys. Rev. B 3 (1971) 2534.  
<https://doi.org/10.1103/PhysRevB.3.2534>.
- [17] B. K. Ridley, B. E. Foutz, L. F. Eastman, Mobility of electrons in bulk GaN and  $\text{Al}_x\text{Ga}_{1-x}\text{As}/\text{GaAs}$  heterostructures Phys. Rev. B 61 (2000) 16862.  
<https://doi.org/10.1103/PhysRevB.61.16862>
- [18] H. G. B. Hicks, D. F. Manley, High purity GaAs by liquid phase epitaxy Solid State Commun. 7 (1969) 1463. [https://doi.org/10.1016/0038-1098\(69\)90022-2](https://doi.org/10.1016/0038-1098(69)90022-2).
- [19] G. E. Stillman, C. M. Wolfe, J. Dimmock, Hall coefficient factor for polar mode scattering in n-type GaAs J. Phys. Chem. Solids 31 (1970) 1199. [https://doi.org/10.1016/0022-3697\(70\)90122-8](https://doi.org/10.1016/0022-3697(70)90122-8).
- [20] M. Razeghi, Photoluminescence topography of shallow impurities in GaAs epilayers grown by metalorganic vapor phase epitaxy Appl. Phys. Lett. 55 (1989) 1677.  
<https://doi.org/10.1063/1.107216>.
- [21] U. K. Mishra, P. Parikh, Y. F. Wu, AlGaIn/GaN HEMTs-an overview of device operation and applications IEEE Proceedings 90 (2002) 1022.  
<https://doi.org/10.1109/JPROC.2002.1021567>.
- [22] B. Radisavljevic, A. Radenovic, J. Brivio, V. Giacometti, A. Kis, Single-layer  $\text{MoS}_2$  transistors Nature Nanotech. 6 (2011) 147. <https://doi.org/10.1038/nnano.2010.279>.

- [23] M. E. Kim, A. Das, S. D. Senturia, Electron scattering interaction with coupled plasmon-polar-phonon modes in degenerate semiconductors Phys. Rev. B 18 (1978) 6890. <https://link.aps.org/doi/10.1103/PhysRevB.18.6890>.
- [24] B. A. Sanborn, Electron-electron interactions, coupled plasmon-phonon modes, and mobility in n-type GaAs Phys. Rev. B 51 (1995) 14256. <https://doi.org/10.1103/PhysRevB.51.14256>.
- [25] A. Hauber, S. Fahy, Scattering of carriers by coupled plasmon-phonon modes in bulk polar semiconductors and polar semiconductor heterostructures Phys. Rev. B 95 (2017) 045210. <https://doi.org/10.1103/PhysRevB.95.045210>.
- [26] Q. Hao, H. B. Zhao, Y. Xiao, Multiscale Thermal Transport in Energy Systems, Chapter 3, Nova Science Publisher, Hauppauge, 2016.
- [27] K. Yee, Numerical solution of initial boundary value problems involving Maxwell's equations in isotropic media, IEEE Transactions on Antennas and Propagation 14 (1996) 302-307. <https://doi.org/10.1109/TAP.1966.1138693>.
- [28] A. Taflov, M. E. Brodwin, Numerical solution of steady-state electromagnetic scattering problems using the time-dependent Maxwell's equations, IEEE Transactions on Microwave Theory and Techniques 23 (1975) 623-630. <https://doi.org/10.1109/TMTT.1975.1128640>.
- [29] R. A. Serway, Principles of Physics, 2nd ed., Fort Worth, Texas, 1998.
- [30] D. D. Manchon, A. S. Barker, P. J. Dean, R. B. Zetterstrom, Optical studies of the phonons and electrons in gallium nitride, Solid State Communications 8 (1970) 1227-1231. [https://doi.org/10.1016/0038-1098\(70\)90365-0](https://doi.org/10.1016/0038-1098(70)90365-0).

## Appendix D. Controlling BCS superconductivity with plasmonic metamaterials

### D.1 Dielectric formulation of the BCS theory

In 1973, Kirzhnits et al proposed reformulation of the BCS theory of superconductivity in terms of the effective dielectric response [1]. They demonstrated, that the phonon mediated electron-electron interaction in a BCS superconductor, which controls the Cooper pairing, can be expressed in the form of an effective Coulomb potential:

$$V(\vec{q}, \omega) = \frac{4\pi e^2}{q^2 \epsilon_{\text{eff}}(\vec{q}, \omega)} = \frac{V_c}{\epsilon_{\text{eff}}(\vec{q}, \omega)}, \quad (\text{D-1})$$

where  $V_c \equiv 4\pi e^2/q^2$  is the Fourier-transformed Coulomb potential in vacuum and  $\epsilon_{\text{eff}}(\vec{q}, \omega)$  is the dielectric response function of the superconductor treated as an effective medium. When the superconducting coherence length is at least an order of magnitude larger than the unit cell of the metamaterial, such a macroscopic electrodynamics description is considered valid. As will be demonstrated later, this requirement gives an upper bound of the unit cell size when designing plasmonic metamaterials for this purpose. The critical temperature of a superconductor in the weak coupling limit is given by Kirzhnits et al as:

$$T_c = \theta e^{-1/\lambda_{\text{eff}}}, \quad (\text{D-2})$$

where  $\theta$  is the characteristic temperature for a bosonic mode mediating electron pairing (a constant), and  $\lambda_{\text{eff}}$  is the dimensionless coupling constant directed proportional to  $V(\vec{q}, \omega)$  and density of states  $\nu$ :

$$\lambda_{\text{eff}} = -\frac{2}{\pi} \nu \int_0^\infty \frac{d\omega}{\omega} \left\langle \frac{V_c}{\text{Im}(\epsilon_{\text{eff}}(\vec{q}, \omega))} \right\rangle. \quad (\text{D-3})$$

We can see from Equations D-1 to D-3 that when  $\epsilon_{\text{eff}}$  is reduced, the effective Coulomb potential is increased, thus the coupling constant  $\lambda_{\text{eff}}$  is increased, eventually leading to the increase in the critical temperature  $T_c$ .

In recent years, Smolyaninova et al [2-3] have explored the idea of increasing  $T_c$  by structured superconducting materials to achieve epsilon-near-zero (ENZ) in certain frequency ranges (i.e., setting:  $\epsilon_{\text{eff}} = 0$ ). They have demonstrated an increment of  $T_c$  for Al from 1.2 K to 3.9 K using an Al/Al<sub>2</sub>O<sub>3</sub> core-shell structure to achieve ENZ. They have tried several superconducting systems over the years, but the above mentioned Al/Al<sub>2</sub>O<sub>3</sub> core-shell system gives the largest  $T_c$  increment so far.

## **D.2 Designing structures matching phonon spectra of BCS superconductors**

Using properly designed plasmonic metamaterials, we can engineer on-demand  $\epsilon_{\text{eff}}$ . On the other hand, since the electron-plasmon scattering rate is higher than the plasmon-phonon and plasmon-photon scattering rates, this effect could be used to control phonon scattering in various electron systems, including solar cells or superconductors [4]. The goal of this work thus includes the following two aspects: first, for selected superconductors we would like to design plasmonic metamaterials with optical responses matching the corresponding electron-photon spectra, so as to maximize the steering effect of the phonon scattering; second, in the vicinity of the plasmonic resonances, ensure epsilon-near-zero can be achieved to maximize the effective Coulomb potential (and thus the coupling constant). In the following section, we present several different designs with photon absorption spectra matching the electron-phonon scattering spectra of corresponding BCS superconductors. We will also give some expectations of experimental observations in the end of the next section. Throughout this chapter, CST MW Studio is used for simulating for all plasmonic metamaterial designs.

### **D.2.1 MIM absorber structures for strong field enhancement**

Metal-insulator-metal (MIM) is a well studied structure for achieving localized plasmonic resonances. Liu et al was the first to use such a structure to obtain metamaterial perfect absorbers [5]. Their MIM unit cell contains a cross shaped metal top layer, a continuous metal bottom layer, and a dielectric ( $\text{Al}_2\text{O}_3$ ) middle layer to separate the two metal layers. For chosen cross dimensions with correspondingly fine tuned dielectric layer thickness, near unity absorption is demonstrated at resonance frequency for perpendicularly incident light. At resonance, the plasmonic mode is localized in between the top and bottom metal layers, with electric field strongly enhanced around the top metal layer.

An MIM architecture is used for all the various designs in this section. The reason for choosing MIM as the general architecture is the following: (1) At resonance, a localized surface plasmon is excited tightly around the top metal layer. This can potentially enhance the electron-plasmon coupling efficiency, thus enlarge the electron-plasmon scattering rate. (2) Since localized SPP modes are responsible for single peaks of near-unity absorption, complicated absorption spectrum can be designed by composition of structures with various linear dimensions.

As a first attempt, we have chosen lead (Pb) as the superconductor. The electron-phonon scattering spectrum (the Eliashberg spectrum) of Pb is given in Figure D-2(b) [6]. Since there are two distinct peaks in this target spectrum, we will need to use a structure with composite unit cells to achieve this. We first design an MIM structure with a single resonance peak matching the lower resonance peak of the Eliashberg spectrum (centering at  $\sim 4$  meV). Such a design is shown in Figure D-1 (a)-(c), with all dimensions given in the figure description, and the absorption spectrum given in Figure D-1(d). In the next step we

constructure a composite unit cell including two MIM unit cells with different top resonator sizes, as shown in Figure D-2(a). A simple addition of the two unit cells generates an absorption spectrum with two near-unity peaks (Figure D-2(c), black line) matching exactly the two peaks of the Eliashberg spectrum of Pb. To achieve connectivity of the whole top layer for the ease of measurement, connecting wires are added to the composite unit cell. The addition of wires does not shift the resonance position of the absorption spectrum, but slightly lowers the absorption peak at higher frequency (Figure D-2(c), red line).

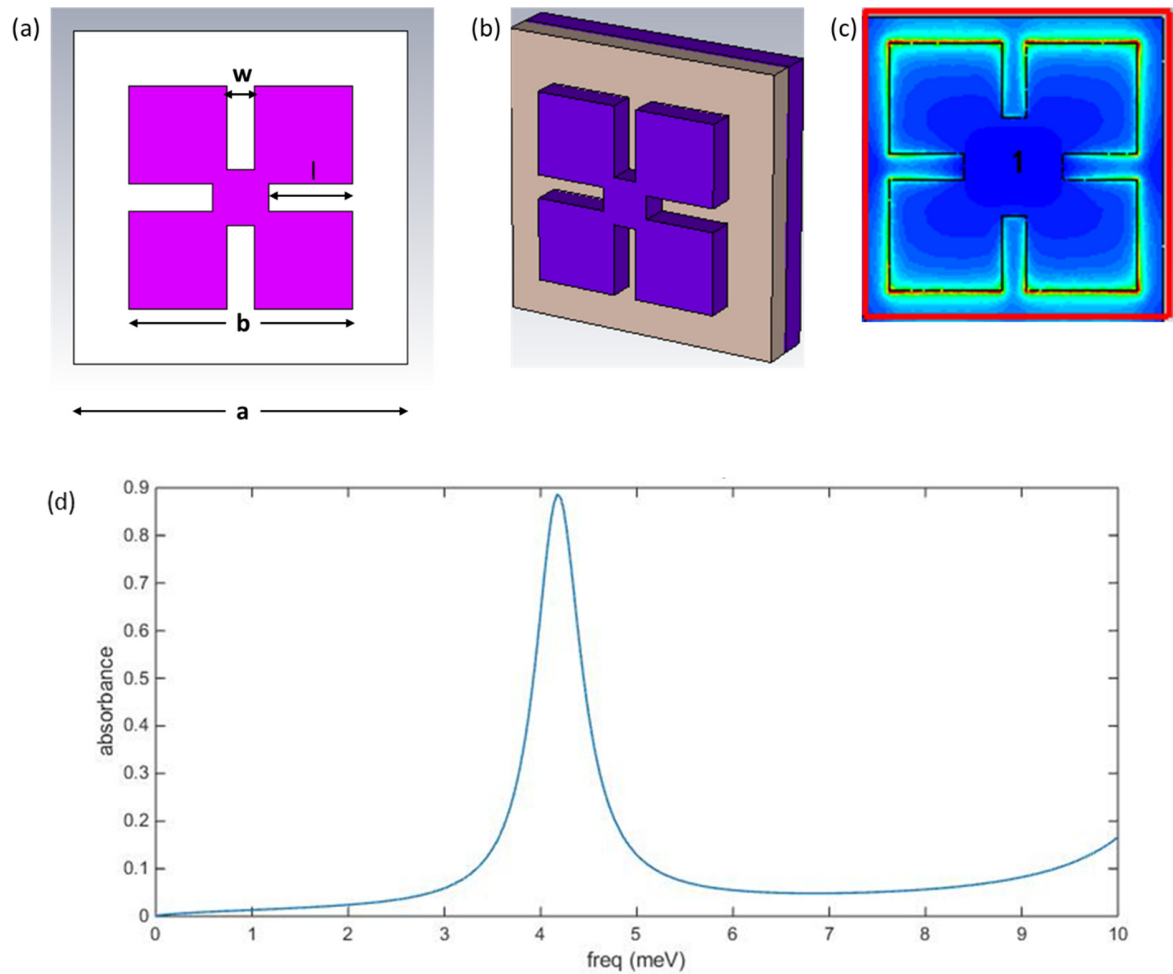


**Figure D-1. Design of an MIM plasmonic metamaterial structure with a well defined local resonance.** (a) Top view of the structure, with (unit:  $\mu\text{m}$ )  $a = 60$ ,  $b = 50$ ,  $l = 15$ ,  $w = 5$ , thickness of both metal (Pb) layers = 1, and thickness of dielectric ( $\text{SiO}_2$ ) layer = 6. (b) Perspective view of the structure. (c)  $|\mathbf{E}|$  field profile of the unitcell at resonance frequency. (d) Absorption spectrum of the designed MIM structure.

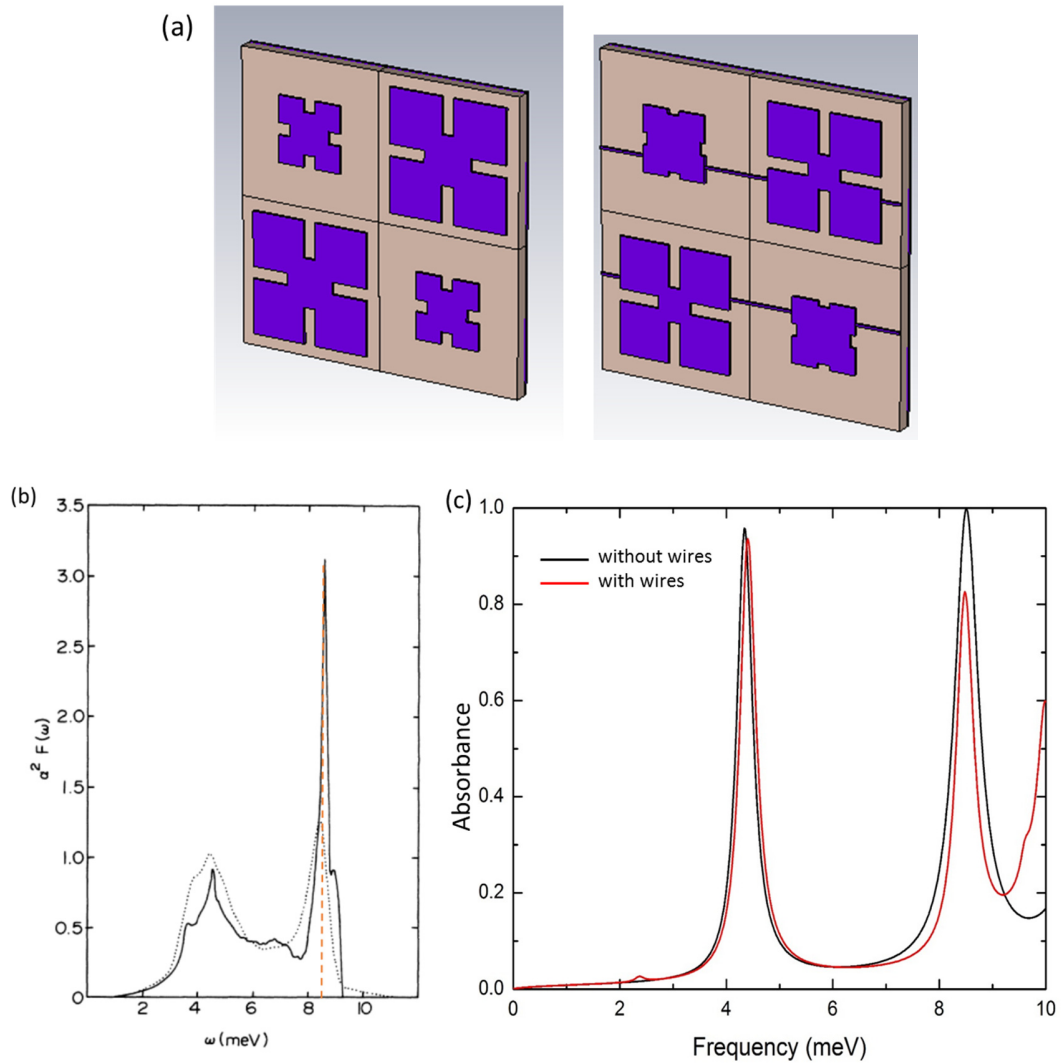


**Figure D-2. MIM plasmonic metamaterial design matching the electron-phonon spectrum of Pb.** (a) The unit cell consisting two copies of resonators with different sizes to achieve two resonances, with (right) and without (left) connecting wires. (b) Electron-phonon scattering spectrum of Pb [10]. (c) Absorption spectra generated by the unit cells shown in (a).

### **D.2.2 Babinet MIM structure designs**

As can be seen from the previous section, although the isolated top element scheme can achieve spectrum match by composite unit cells, it suffers from the connectivity problem which requires additional connecting wires to be added. The additional connecting wires can alter the original absorption spectrum, making the design less predictable. An alternative approach is to start the design with the Babinet structure of the top metal element. The name “Babinet structure“ originates from Babinet’s principle. In 1837, French physicist Jacques Babinet formulated the following principle [7]: the diffraction pattern from an opaque body is identical to that from a hole of the same size and shape except for the overall forward beam intensity. This principle originates from the duality between the electric and magnetic fields. In our case, exchanging the metal and dielectric parts in the top layer gives the Babinet of the original structure. Note that the Babinet structure of the isolated resonator in the top layer is automatically a connected network, which naturally solves the connectivity problem.

With this in mind, we start tuning a structure using the Babinet scheme. Figure D-3 shows such a Babinet structure with its absorption spectrum matching the Eliashberg spectrum of Pb. Each unit cell consists of the Babinet pattern of two opposing split ring resonators in the top metal layer. Note that for this structure, the absorption peak at higher frequency is a higher order mode, and thus has a smaller coupling efficiency (leading to a smaller absorption peak height).

As discussed in earlier section, superconducting coherent length places an upper limit on the linear sizes of the plasmonic metamaterial unit cells. Although the previous two design proposals can generate good matching spectra, they both might suffer from over sized unit

cells. In the following, we discuss the possibility of meeting the coherent length limit. Most superconductors have their Eliashberg spectra peaked in a frequency range of 1 to 100 meV, with their superconducting coherent length in the range of between 100 to 1000 nm. We also know that for an MIM structure at resonance, the electric fields are mainly focused in the vicinity of the top metal pattern. This may indicate that as long as the top metal pattern has one linear dimension smaller than the coherent length, the effective medium approximation can still be treated as valid. Although we cannot design an MIM structure to resonate in the meV frequency range with unit cell size on the order of 100 nm, we can at least design an MIM structure with the top metal pattern composed solely of ultra-thin connected metal wires with their thickness below the superconducting coherent length limit. Figure D-4 shows such a thin-wire Babinet MIM design. The top metal layer is composed of connected metal wires with square cross-sections of  $50 \times 50 \text{ nm}^2$ , well below the 100 nm superconducting coherent length limit. The intermediate dielectric layer is chosen to be SU8 epoxy. We can see that for a unit cell size tuned from 20 to 38  $\mu\text{m}$ , the resonant absorption peak of this MIM structure sweeps from 60 to 80 meV. This range is in good agreement with the Eliashberg spectrum of  $\text{MgB}_2$  superconductor [8-9]. Figure D-4 thus gives a good proposal for potentially enhancing the  $T_c$  of  $\text{MgB}_2$  superconductor.

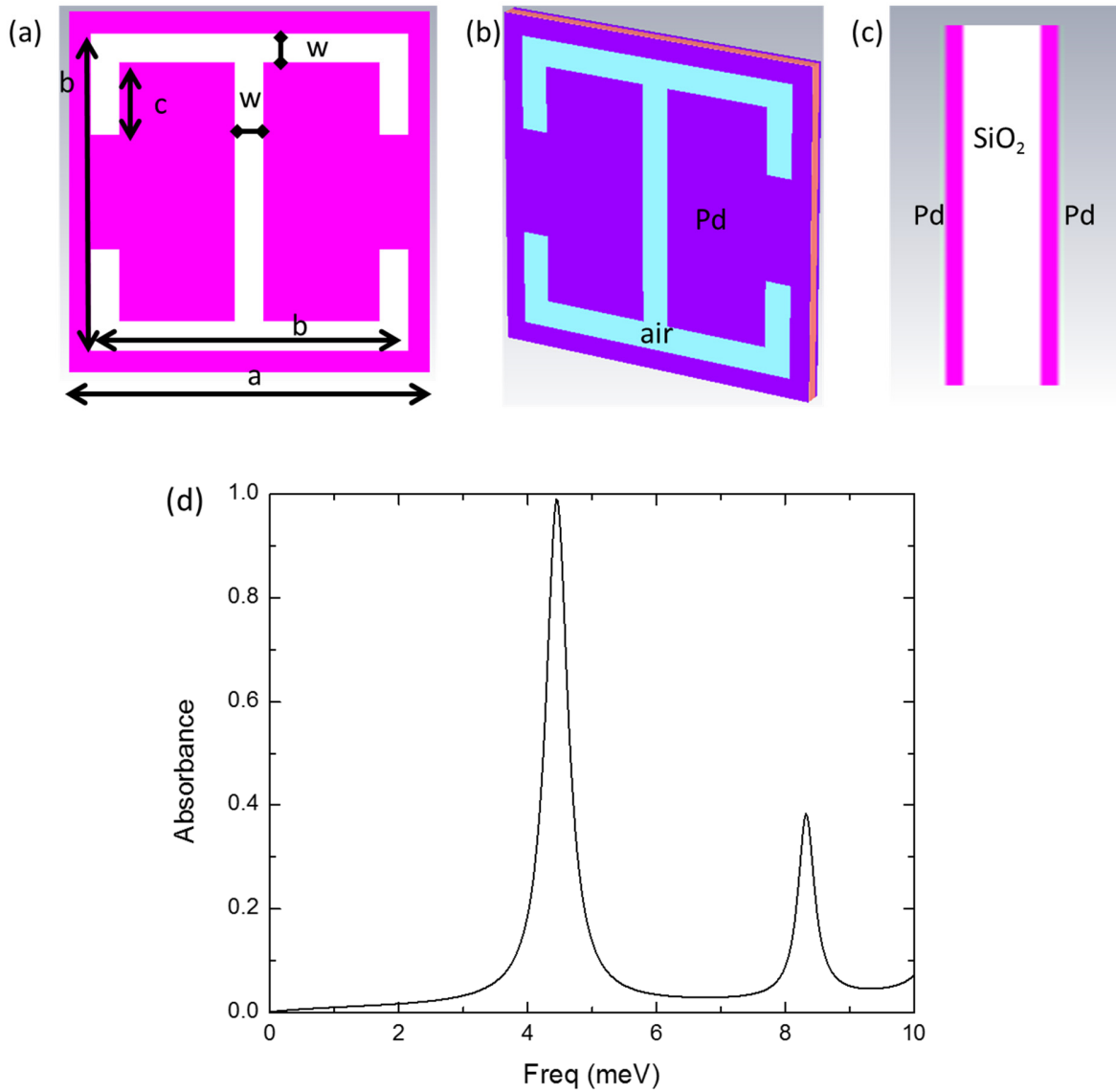


**Figure D-3. Babinet MIM structure for matching Eliashberg spectrum of Pb.** (a-c) Top view (a), perspective view (b) and side view (c) of the Babinet MIM structure. Dimensions (unit:  $\mu\text{m}$ ):  $a = 125$ ,  $b = 90$ ,  $w = 10$ ,  $c = 25$ , metal thickness = 1, dielectric thickness = 5. The structure is the Babinet of a double split ring resonator. (d) Absorption spectrum of the Babinet MIM structure.

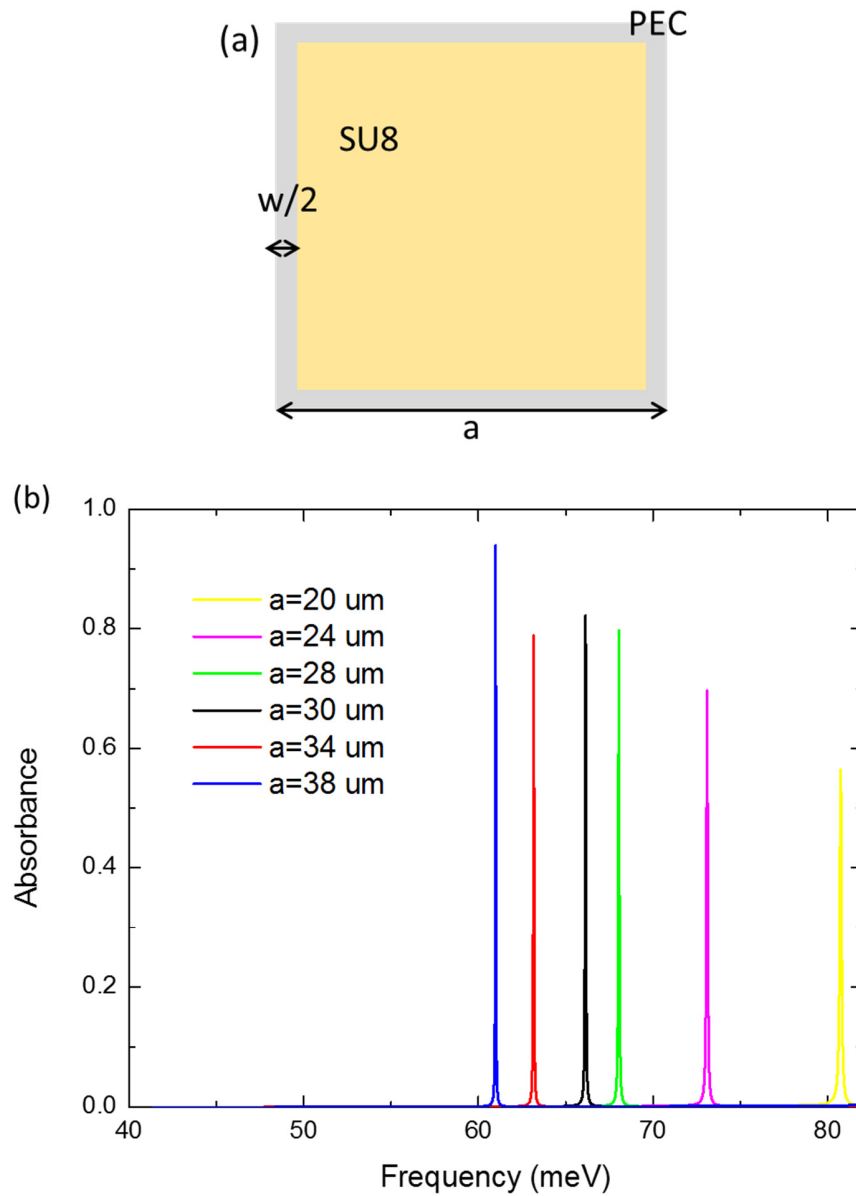


**Figure D-4. Babinet structure of thin connected frame.** (a) Top view of the designed structure. Dimensions (unit:  $\mu\text{m}$ ):  $w = 0.05$ , top metal (PEC) thickness = 0.05, dielectric (SU8) thickness = 1, bottom metal thickness = 0.5. (b) Absorption spectra at tuned unit cell size  $a$ .

### **D.2.3 Experimental expectations**

Experimental setup for measuring the above proposed Babinet MIM structures include the following: (1) Fabrication of an array of the Babinet MIM plasmonic metamaterials using nano-fabrication techniques including e-beam lithography and metal/dielectric evaporations. A larger than 10k by 10k array is desirable to minimize the edge effect. (2) Measure the absorption spectrum in the meV range using instrument such as FTIR with the correct light source. If the measured spectrum matches the designed spectrum, we can go to the next step. Otherwise, design should be adjusted and fabrications should be re-done. (3) Connecting the top layer (the Babinet layer) of the two metal layers with electrodes in a 4-probe scheme to measure the resistance of it. (4) Putting the whole device and measurement setup into a dilution fridge to measure the resistance of the top Babinet layer as the temperature drops continuously below the  $T_c$  of the top metal layer. If the Babinet MIM design worked successfully, we should see an increased  $T_c$  compared to the bulk  $T_c$  of the superconducting metal.

## References:

- [1] D. A. Kirzhnits, E. G. Maksimov, D. I. Khomskii, The description of superconductivity in terms of dielectric response function, *J. Low Temp. Phys.* **10**, 79 (1973).
- [2] V. N. Smolyaninova, K. Zander, T. Gresock, C. Jensen, J. C. Prestigiacomo, M. S. Osofsky, I. I. Smolyaninov, Using metamaterial nanoengineering to triple the superconducting critical temperature of bulk aluminum, *Sci. Rep.* **5**, 15777 (2015).
- [3] V. N. Smolyaninova, C. Jensen<sup>1</sup>, W. Zimmerman<sup>1</sup>, J. C. Prestigiacomo, M. S. Osofsky, H. Kim, N. Bassim, Z. Xing, M. M. Qazilbash, I. I. Smolyaninov, Enhanced superconductivity in aluminum-based hyperbolic metamaterials, *Sci. Rep.* **6**, 34140 (2016).
- [4] K. Kempa, Dielectric function of media based on conductive particles, *Phys. Rev. B* **74**, 033411 (2006).
- [5] X. Liu, T. Starr, A. F. Starr, W. J. Padilla, Infrared spatial and frequency selective metamaterial with near-unity absorbance, *Phys. Rev. Lett.* **104**, 207403 (2010).
- [6] W. L. McMillan, J. M. Rowell, Lead phonon spectrum calculated from superconducting density of states, *Phys. Rev. Lett.* **14**, 108 (1965).
- [7] J. D. Edmunds, M. C. Taylor, A. P. Hibbins, J. R. Sambles, I. J. Youngs, Babinet's principle and the band structure of surface waves on patterned metal arrays, *J. Appl. Phys.* **107**, 103108 (2010).
- [8] C. Buzea, T. Yamashita, Review of superconducting properties of MgB<sub>2</sub>, *Supercond. Sci. Technol.* **14**, R115 (2001).
- [9] W. N. Kang, H. J. Kim, E. M. Choi, C. U. Jung, S. I. Lee, MgB<sub>2</sub> Superconducting Thin Films with a Transition Temperature of 39 Kelvin, *Science* **292**, 1521 (2001).
- [10] W. L. McMillan, J. M. Rowell, Lead phonon spectrum calculated from superconducting density of states, *Phys. Rev. Lett.* **14**, 108 (1965).

## **Appendix E. Other EM response designs using plasmonic metamaterials**

### **E.1 Realization of all optical states via electrical tuning of a two-element metasurface**

A 3-state tunable metasurface is demonstrated at X band (8 to 14 GHz), via electrical modulation of the capacitance of two varactor diodes within each unit cell. At a selected frequency (8.8 GHz), the optical state of the metasurface changes from absorptive to reflective then to transmissive under different applied voltages. The realization of this 3-state tuning is explained by resonance frequency shifting and impedance matching of the metasurface, based on extracted S-parameters from measured reflectance and transmittance. An effective L-C circuit model of the metasurface is developed to verify the capacitive tuning nature of the device. Full wave finite difference time domain simulations show good agreement with the experimental results. This tunable metasurface shows all wave-matter interactions in one device at X-band. Our results expand the flexibility of tunable metasurfaces and suggest a new way to achieve high-speed spatial light modulation.

Generally, when photons encounter a surface, the following processes thoroughly describe their interactions: the photon is absorbed (A) inside, is reflected (R) from, transmits (T) through, and is scattered from the surface, as well as the forming of surface waves along the surface. For homogeneous surfaces with sub-wavelength composite unit cells that do not support surface waves and have ignorable scattering, A, R, T give a complete description of their interactions with photons, as is the case for most surfaces of natural materials. Dynamical control of the response (A, R, T) of a surface to electromagnetic (EM) radiations has been a pursuit of scientists for long, with spatial light modulator (SLM) being a prominent example. SLMs are addressable devices with states of light-matter interactions

(A, R, T) controlled pixel by pixel. Conventional SLMs have been shown the abilities to modulate the amplitude or phase for one state [1-2]. What is yet to come is a device that can modulates among all the three fundamental states of light-matter interactions, *i.e.*, high A, R and T, at the same frequency. This device can be treated as a generalized SLM and has numerous potential advantages in spectroscopic and imaging applications [3], including compressive sensing [4]. Here, based on metamaterials (MMs), we demonstrate a 3-state tunable metasurface working at around 9 GHz.

MMs are artificial materials that can show on-demand EM properties by appropriate designs of composite structures. Since the first realization in the microwave range in year 2000 [5], MMs have been applied to a wide range of fields, including MM perfect lenses [6], MM invisible cloaks [7], and MM perfect absorbers [8]. Recently, gradient-index metasurfaces have been shown to have the ability to arbitrarily manipulate EM wavefronts [9], promising an ultra-compact way to tweak EM waves. MMs are resonant structures that exhibit strong frequency selectivity. Thus, the desired EM functionalities are limited to certain frequencies for specific MM structures, generating a strong demand of MM tuning to expand the function frequency range for practical applications, but it also mean the large modulation depth can be achieved by MM modulators. By introducing active materials such as diodes [10], liquid crystals [11], semiconductors [12] and phase changing dielectric materials [13], recent researches have demonstrated the tuning of the MM resonance frequencies. Mechanical tuning of the MM property is also achieved by combining MM with MEMS structures [14]. Among these strategies, using diodes as the tuning knob for MMs can achieve the highest modulation speed via electrical tuning, and is more stable in fabrication thanks to the maturity in commercially available diodes. Using diodes as the

tuning component for MM is an ideal strategy for RF and microwave frequency below GHz due to the limited response time of diodes. Utilizing the ON and OFF states of diodes, switchable reflector–absorber is realized with diodes mounted inside one unit or between neighboring units [10]. By controlling the capacitance of varactor diodes via reverse bias, tunable MM absorber with high absorption peak tuning from 4.45 to 5.64 GHz is also reported [15]. These tunable metasurfaces are limited to modulate between high R and high A states mainly due to the necessity of a metal ground plane for diode mounting and voltage applying. So an ideal modulator will have expanded functional frequency to GHz such as K band (8 -12 GHz) and all states modulation.

In this work, we demonstrate the achievement of a 3-state tunable metasurface working at around 9 GHz. The tuning design is based on the resonance properties of multiple splitting resonators (SRR). Inserted varactor diodes work as the controller of the capacitances in one unit cell.

## **E.2 Designed structures achieving 3-states modulation**

### **E.2.1 Modulation of responses of metasurfaces with varactor diodes**

The response of the metasurface to the external EM wave can be described by its effective impedance  $z(\omega) = (\varepsilon/\mu)^{1/2}$ . Without any modulation scheme, the resonance property is purely determined by the geometric parameters, which is the usual case of a metasurface, with an effective capacitance  $C_0$ , inductance  $L_0$  and resistance  $R_0$ , leading to resonance

frequency  $f_0 = \frac{1}{2\pi\sqrt{L_0C_0}}$ . With an existing metasurface, if the total capacitance  $C$  or total

inductance  $L$  can be modified by external controlled capacitors or inductors, the resonance

frequency will shift inversely as the increment of them. Varactor diode is a kind of PN junction with varying capacitance. The capacitance of a varactor diode can be controlled by the voltage over it up to GHz frequency range. Taking the model Skyworks SMV2019-079LF as an example: its capacitance can be tuned from 2 to 0.2 pF with reverse voltage increasing from 0 to 20 V. The effective circuit parameters are listed in the datasheet of Skywork Solution Inc. The frequency dependent capacitance of varactor diodes can be written by formula:  $C(V) = \alpha_0 / (\beta + V)^n$ , with  $\alpha_0, \beta, n$  constants.

Each unit cell of our tunable metasurface consists of two SRR elements along the EM wave propagation direction, with one varactor diode mounted in each SRR element. Tuning of the capacitance of the varactor diodes not only changes the effective capacitance in each individual element, but also tunes the interaction between the two elements, and thus further increases the tunability of the device. Applying external voltage will change the capacitance of the diodes and thus the impedance of each unit cell. The resonance frequency will be shifted as a result. By suitably designing the structure to achieve a large enough tuning range, we can get the overlap of high A, R and T at the same frequency (8.8 GHz). We thus call this 3-state tunable metasurface the ART metasurface.

### **E.2.2 Structure of metasurfaces with varactor diodes and simulation results**

Schematic cartoons in Figure E-1a & 1b reveal the design details of our ART metasurface. It is a 2-layer printed circuit board (PCB) structure with FR4 on bottom and structured Cu on top. All relevant parameters are defined in Figure E-1a & b. The thickness of the FR4 and Cu are  $h_{\text{di}} = 1.55$  mm and  $h_{\text{Cu}} = 17$   $\mu\text{m}$ . The unit cell is composed of a double ring resonator (as a single element) and a mirror of it (thus two elements). Varactor diodes are

mounted in the gaps of the double ring resonator. The 2 thick wires on the outer sides of the unit cell work as part of the resonator and the connecting wires for applying voltages to the diodes. The incident electric field is polarized along the thick wire with magnetic field perpendicular to the ring plane, as indicated by the white arrow in Figure E-1b. After the varactor diodes were mounted, great changes take place for the reflection and transmission spectra as shown in Figure E-2. The varactor diodes we used are Skyworks SMV2019-079LF, whose capacitance can be tuned from 2 to 0.2 pF with reverse voltage increasing from 0 to 20 V. As mentioned before, the frequency dependent capacitance of varactor diodes can be written by formula:  $C(V) = \alpha_0/(\beta + V)^n$ . For SMV2019-079LF, the parameters we got from analyzing the experimental data in ref 13 are:  $\alpha_0 = 6.25$ ,  $\beta = 2.53$ ,  $n = 1.07$ . After comparing with the experimental data we will show in the following sections, we find that the modified parameters best fit our measured data:  $\alpha_0 = 6.25$ ,  $\beta = 10.53$ ,  $n = 1.07$ . It's normal that the capacitance we get varies from the data sheet and the existing tuning works, since the frequency we are targeting is much higher than those cases. The effective capacitance of the varactor diode will decrease as the working frequency increases, so as the range of capacitance modulation of the diode itself. It can be predicted that if the working frequency of the varactor diodes is increased to beyond the K band, the modulation will be weaker. The results we get correspond to an 8 V (from the difference of fitted  $\beta$ ) left shift of the results at  $\sim 2.5$  GHz. In the following simulations, the varactor diode is treated as a lumped element with tunable capacitance. To achieve the 3-state tunable metasurface, we optimized structure parameters we get are as the following:  $a = 17.8$  mm,  $b = 10$  mm,  $c = 14$  mm,  $w_1 = 0.25$  mm,  $w_2 = 0.75$  mm,  $w_3 = 2.5$  mm,  $g_1 = 0.25$  mm,  $g_2 = 0.38$  mm,  $L_1 = 2.5$  mm and  $L_2 = 3.5$  mm. The full wave electromagnetic

simulations are done by CST. The conductivity of Cu is taken as  $5.8 \times 10^7$  S/m. The permittivity of FR4 is set as 4.2 with a loss tangent of 0.025. Diodes are set as lumped elements with voltage dependent capacitance as discussed above. The reverse voltage varies in our simulation from 0 V to 21 V. The simulated transmission coefficient ( $S_{21}$ ) shows shift of resonance peak from 7.4 GHz to 9.2 GHz with reverse bias increasing from 0 V to 21 V. The reflectance and absorbance spectra are shifting in an according way. Spectra of  $|S_{21}|$  under various biases are shown in Figure E-2b.

Our goal is to have a unique frequency ( $x$  axis) under which all A, R, T are high at different reverse biases ( $y$  axis). From the simulation results we can see that at  $\sim 8.8$  GHz, they do overlap under different biases, with high reflectance occurring at 0 V, high absorbance at  $\sim 6$  V and high transmittance at 21 V. The corresponding spectra are plotted in Figure E-3e. Figure E-3f is the moving of absorbance, reflectance and transmittance as voltage increases at 8.8 GHz.

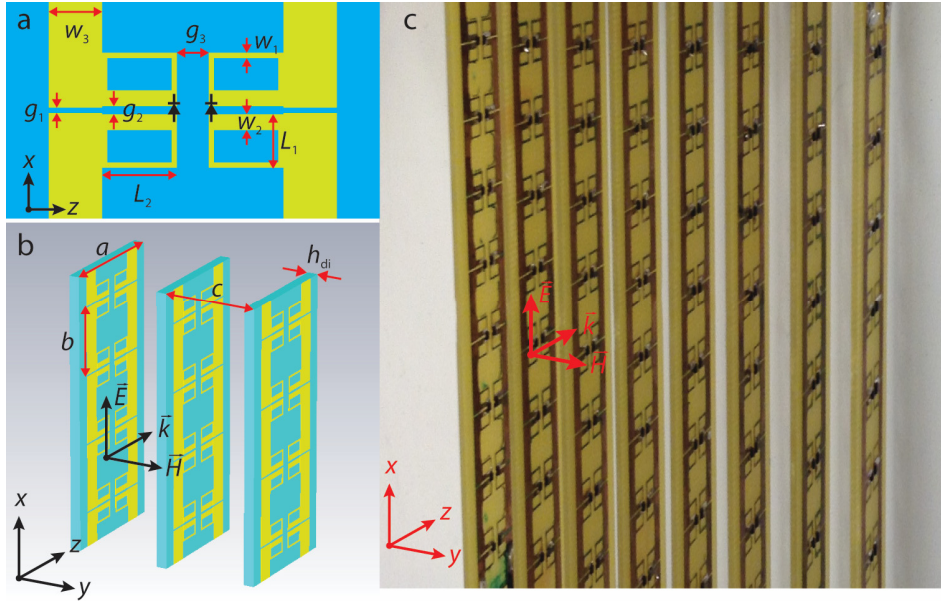


**Figure E-1. Design and fabrication of a tunable metasurface.** (a) Top view of one unit cell of the tunable structure, with yellow corresponding to metal (Cu) and blue to dielectric (FR4). Locations of two mounted varactor diodes (Skyworks SMV 2019-079) are indicated by black diode symbols. (b) Perspective view of a 4x3 array of the tunable metasurface, with polarization of incident light defined by black arrows. All relevant parameters are defined in (a) & (b). (c) Optical image of a fabricated 10x8 array of the tunable metasurface.

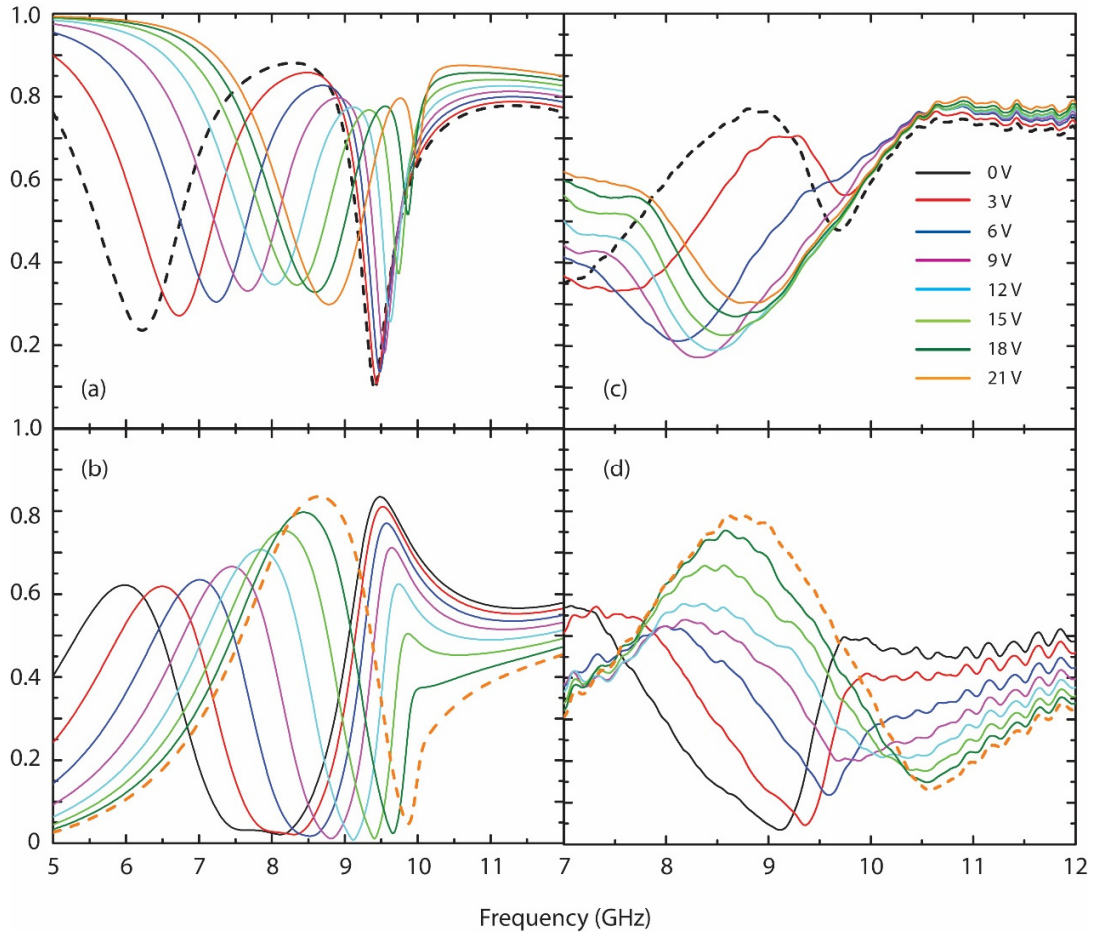


**Figure E-2. Simulations and measurements of a 3-state “ART” tunable metasurface.** (a) simulated  $|S_{21}|$  when tuning reverse bias from 0 to 21 V ( $V_1 = V_2 = V_R$ ). (b) measured  $|S_{21}|$  when tuning reverse bias from 0 to 21 V ( $V_1 = V_2 = V_R$ ). (c) simulated  $|S_{11}|$  when tuning reverse bias from 0 to 21 V ( $V_1 = V_2 = V_R$ ). (d) measured  $|S_{11}|$  when tuning reverse bias from 0 to 21 V ( $V_1 = V_2 = V_R$ ).

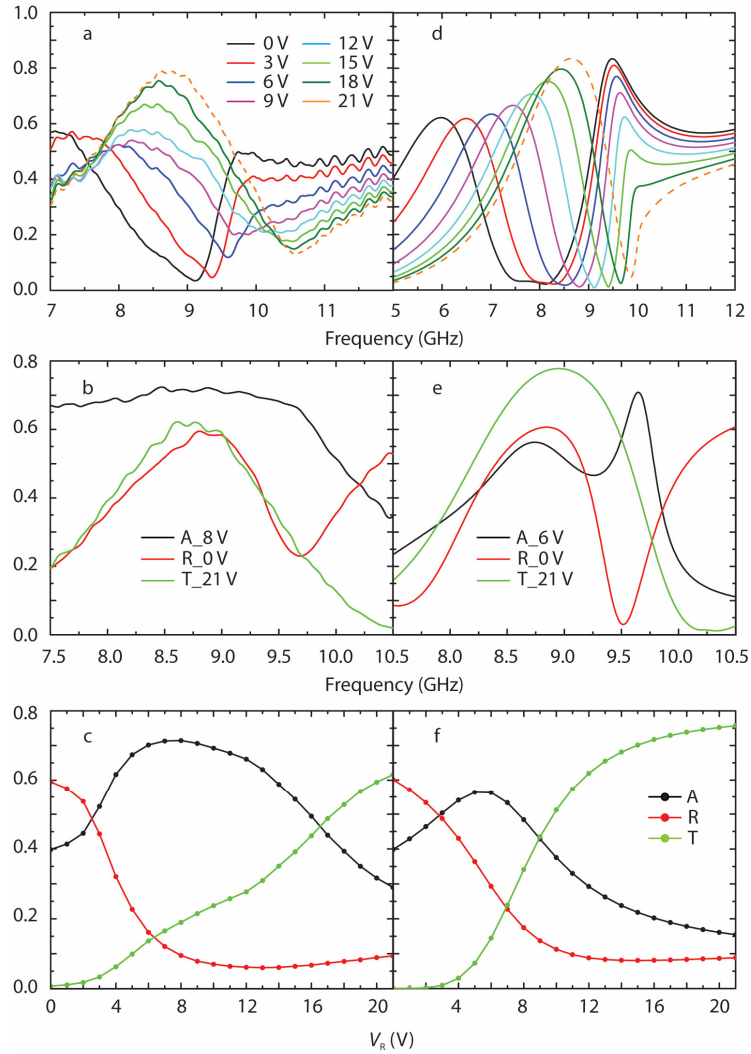


**Figure E-3. Demonstration of achievement of all “ART” states at tuned voltage.** (a) Measured  $|S_{21}|$  when tuning reverse bias from 0 to 21 V ( $V_1 = V_2 = V_R$ ). (b) Measured absorbance at 8 V; reflectance at 0 V; transmittance at 21 V. The spectra show at 8.8 GHz, their peaks coincide. (c) Absorbance, reflectance and transmittance *v.s.* voltage with fixed frequency (8.8 GHz). (d) Simulated  $|S_{21}|$  when tuning reverse bias from 0 to 21 V ( $V_1 = V_2 = V_R$ ). (e) simulated absorbance at 6 V; reflectance at 0 V; transmittance at 21 V. The spectra show at 8.8 GHz, their peaks coincide. (f) Absorbance, reflectance and transmittance *v.s.* voltage with fixed frequency (8.8 GHz).

### E.2.3 Experimental results

Guided by the above simulation results, we fabricated and measured the samples to demonstrate the 3-state tunable metasurface. Fabrication is done on a commercial FR4 board with 35  $\mu\text{m}$  thick Cu layer on single side. The structure on the surface is written by milling machine (LPKF ProtoMat S63). Diodes are mounted inside the gap by hand. We made 10x8 unit cells and the samples are fixed by holders on the two ends to keep the distance between unit cells in y direction fixed. The ends of outer wires are soldered with copper wire for connecting to electrodes of voltage sources. Figure E-1c displays a photo of the fabricated sample. In the measurement, the ART metasurface sample is placed vertically and surrounded by the microwave absorbers. Two horn antennas connected to a vector network analyzer (Agilent N5247A PNA-X) are used as the source and receiver. Transmission coefficient was measured by facing 2 horns towards each other with 4-foot separation according to the focal distance of the horns. The reference spectrum was taken from the transmission of a hole on the microwave absorber with the same size as the sample at normal incidence. For reflection coefficient ( $S_{11}$ ), the incident angle is 15 degrees and we used a metal plate as the normalization reference. The absorbance, reflectance and transmittance were calculated from the measured S parameters.

The measured results are shown in Figure E-3 a-c. When reversed bias increases, the spectrum of  $|S_{21}|$  blue shifts, following the same trend of the simulated result. As the reverse voltage reaches 21 V, the transmission peak moves from 7 GHz to 9 GHz as illustrated in Figure E-3a. The tuning range can be as large as 2 GHz. Compared to the simulations, the calculated absorption spectrum is slightly broadened. We contour plot the A, R, T map

versus reverse bias and frequency for both measurement and simulations in Figure E-4, with a 1 V step for voltages from 0 V to 21 V.

We can observe that they have identical key features: the peaks are blue shifting under higher reverse bias for both simulation and experiment. We achieved simultaneously high absorbance (71% at 8 V), high reflectance (60% at 0 V) and high transmittance (62% at 21 V) at 8.8 GHz as shown in Figure E-3b. Measurement shows broadening and damping of spectrum compared to simulation. This is more obvious for the absorbance spectrum which is calculated by  $A = 1 - R - T$ . This deviation can be caused by not having enough uniformity in sample fabrication, especially the resistance and inductance induced by hand-soldering of diodes; the air layer distance between 2 neighboring metasurfaces is not exactly 14 mm as designed and thus the periodicity is not uniform; and it should also mention that the varactor diodes have a tolerance of about 10%, this will also lead to the broadening of spectrum [15].

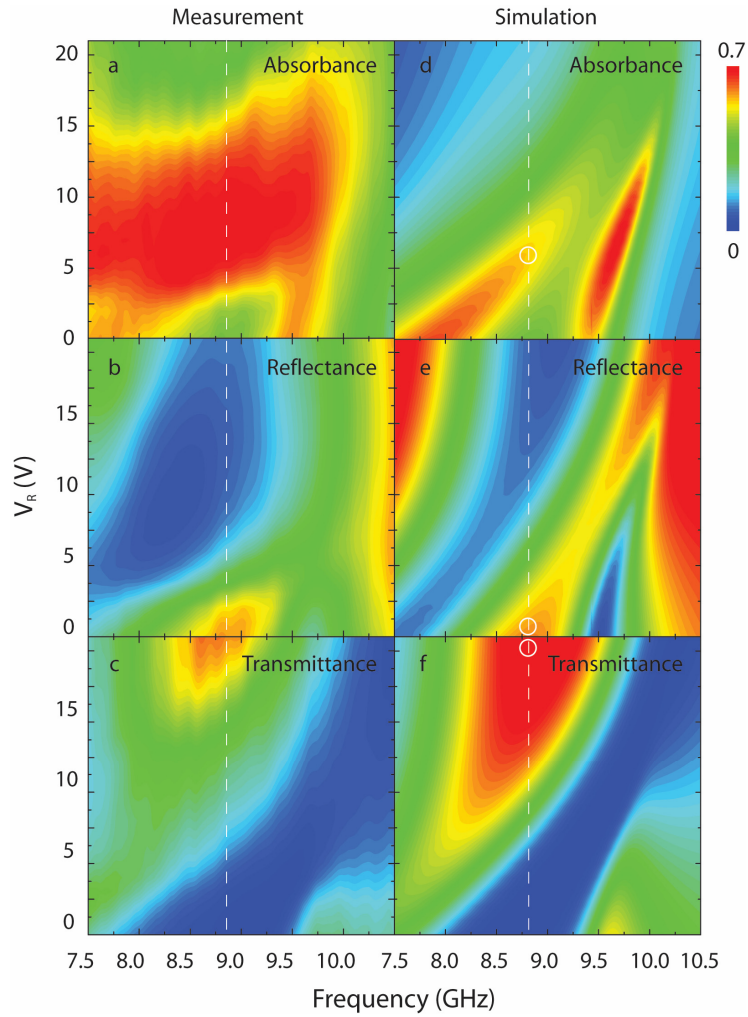


**Figure E-4. Contour plot of the measured and simulated spectra of 3-state “ART” tunable metasurface.** (a)-(c) Measured results for 3-state metasurface working at 8.8 GHz. At 0 V, 8 V and 21 V, we achieved high reflection, absorption and transmission. (d-f) Simulated results for 3-state metasurface working at 8.8 GHz. At 0 V, 6 V and 21 V, we achieved high reflection, absorption and transmission. Color maps plot reverse bias  $V_R$  from 0 to 21 V with  $dV_R = 1$  V. Color scale is the same for (a) – (f), with color bar representing 0 (blue) to 0.7 (red).

### E.3 Discussion

#### E.3.1 Extraction for effective impedance of the metasurface

To deepen our understanding of this tuning process, we extracted the effective permittivity and permeability from the S parameters by the retrieval method from Ref. [16-18]. Since the thickness of our ART metasurface ( $d$ ) is not deep subwavelength, we have to take the effect of spatial dispersion into consideration. The extracted results are shown in Figure E-5 and Figure E-6. According to Ref [18], phase advance  $\theta = 2\pi\omega d\sqrt{\epsilon\mu}$  is used to characterize the influence of spatial dispersion.  $\theta$  is the phase advance of the EM wave as it passes through the ART metasurface. It is a complex number dependent on thickness and frequency.  $\theta$  works as a correction term in the extraction [18]. When  $\theta$  is  $\pi$ , the extracted parameters will give unphysical results such as negative imaginary part and anti-resonance as shown in Figure E-5a and b. The corrected results, after taking into account the spatial dispersion effect, as shown in Figure E-5c and d, differ significantly from the directly extracted results (Figure E-5a and b) in the regions where  $\theta \approx \pi$ .

In Figure E-6a & b we show the corrected permittivity and permeability for various applied voltages. As we increase the voltage, both the fundamental and higher (second) order modes of the permittivity resonance peaks move to higher frequencies. Our ART metasurface is designed to work at the second order mode around 9 GHz. The permittivity values of our ART metasurface shows a Lorentz shape around the resonance frequency, which is the intrinsic line shape of gapped wires [19]. Moving of the resonance peak does not change the shape of the Lorentz resonance. The same line shape and trend of shifting apply for the permeability. Corresponding impedances are shown in Figure E-6c and d. Since the wave matter interaction can be treated as impedance dependant, the strongly

voltage dependent of the impedances in the frequency range 8 ~ 9 GHz directly cause the differences of the spectra as varying voltages. When the voltage goes to 20 V, the impedance of the metasurfaces almost matches that of the air at 8.8 GHz, with  $z' = 0.8$ ,  $z'' = 0$ . At the same time, the extracted permittivity and permeability show low magnetic and electric losses, assuring the realization of high transmission. For the absorption case, with 6 V applied voltage, the main difference lies in that the imaginary part of  $\mu$  has a local maximum, and thus leads to strong absorption at this frequency.

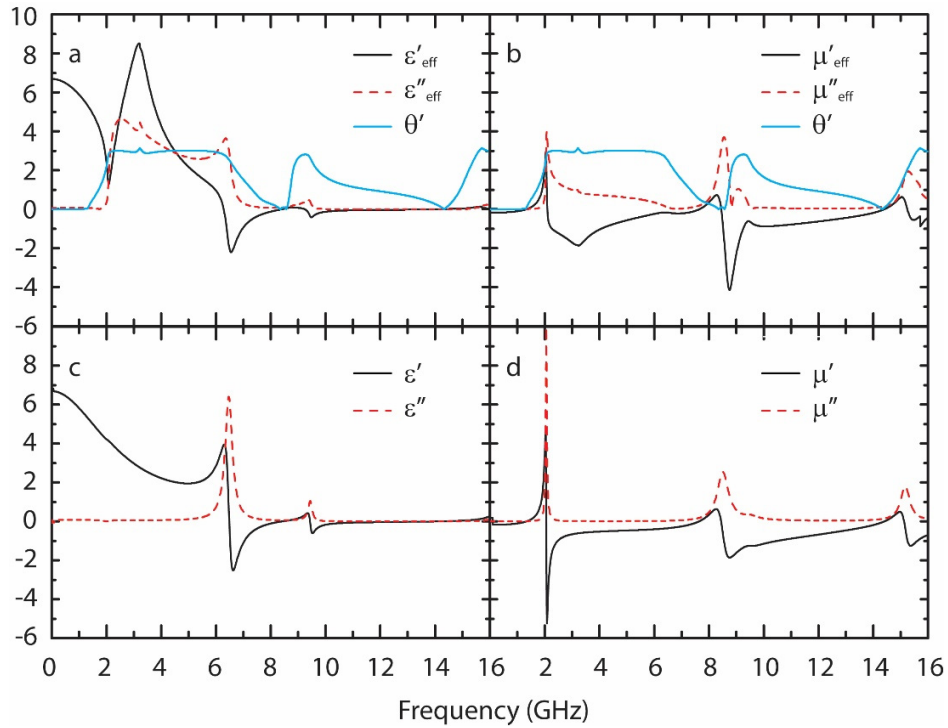


**Figure E-5. Effective permittivity and permeability extractions with spatial dispersion taken into account.** (a) & (b) Directly extracted permittivity (a) and permeability (b) under 0 V bias.  $\theta$  is the phase advance caused by the finite size of the unit cell. (c) & (d) Extracted permittivity (c) and permeability (d) after taken into account the effect of spatial dispersion.

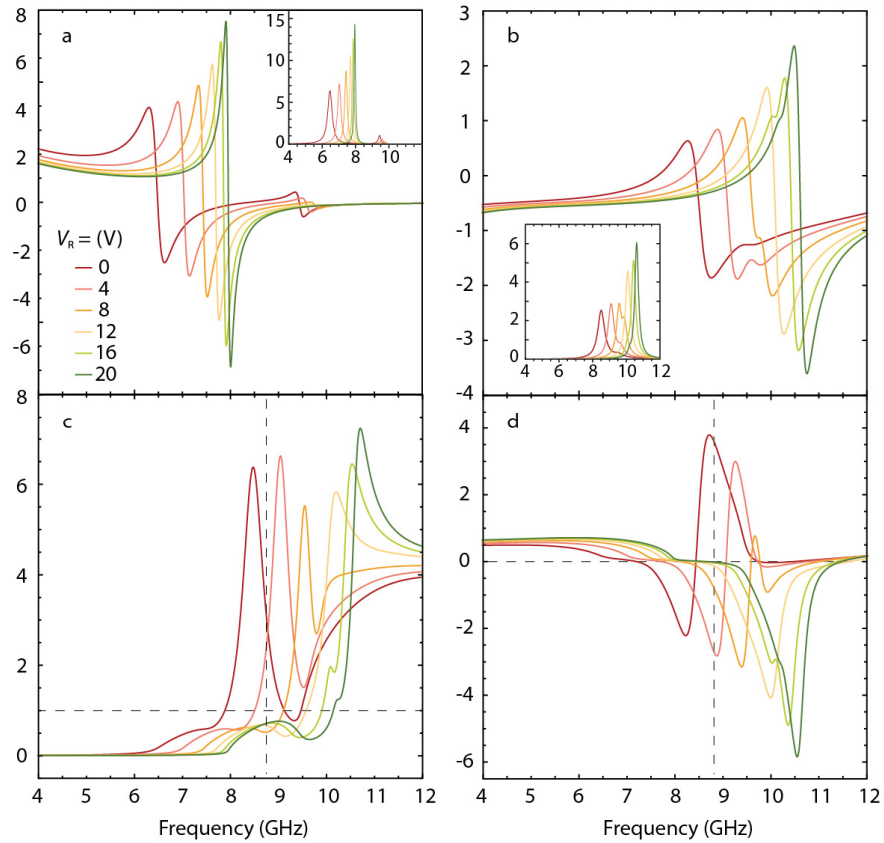


**Figure E-6. Extracted permittivity, permeability and impedance when tuning applied voltage.** (a),(b) Real part of permittivity (a) and permeability (b). Tuning of voltages is depicted as changing of colors. Inserts are imaginary parts for permittivity and permeability. (c),(d) Real part (c) and imaginary part (d) of effective impedance.

### E.3.2 Extraction for intrinsic LC properties of the metasurface

It is pointed out that the resonance of MMs can be understood as a LC resonator with effective capacitance and inductance [19]. Take split ring resonator (SRR) for example, the capacitance is mainly determined by the gap and the inductance comes from the metal wire. It's easy to understand that the shifting of resonance frequency is caused by changing of the added capacitance. However, determining the intrinsic capacitance and inductance of one structure is not trivial. For our design, we can use the LC model to approximate the intrinsic resonance and the tuning process. After mounting the diodes, the capacitance of the system comes mainly from 2 parts: the intrinsic gap capacitance and the added capacitance from the diodes. The inductance of the system comes from the intrinsic inductance and the added inductance from the diodes. For varactor diodes, we treat the inductance to be constant and the capacitance to be voltage dependent. So we can write the approximate expression for resonance frequency with the voltage dependent added capacitance as the only variable. The simplified expression is

$$f = \frac{1}{2\pi\sqrt{(L_0 + L_{add}) \times (C_0 + C_{add})}},$$
 with  $L_0$  and  $C_0$  being the intrinsic values and  $L_{add}$  and

$C_{add}$  the effective values from diodes. We fitted the simulated magnetic resonance peak by the formula above and the fitted parameters are:  $C_0 = 0.373$  pF and  $L_0 + L_{add} = 0.44$  nH. From the fitting result, we estimate the intrinsic structure to have magnetic resonance at a frequency close to 12.5 GHz. The simulation result without diodes mounting illustrated in supplemental information turns out to have magnetic resonance at 13.2 GHz. The simulation verifies our understanding of the tuning process, and furthermore, it can work as a general scheme for determining intrinsic LC of any other complicated structures. The

error also comes from the fact that the capacitances of the varactor diodes in our case are not accurately predicted. For lower frequency resonators, more accurate result can be expected.

### **E.3.3 Two-state switch**

Besides the 3 states tunable metasurface, the structure can also work as a 2-state switch. It can be designed to change between reflection and absorption as normal tunable MM. It can also be designed to be a transmission and absorption switch after optimizing the geometry. Without considering all the 3 states together, the 2 states devices can give better performance in tuning amplitude. As in Figure E-7, a designed “AT” switch with around 90% absorption and transmission at 8.5 GHz is shown. The phase modulation can also be achieved by this kind of scheme as the effective index is controlled by the voltage.

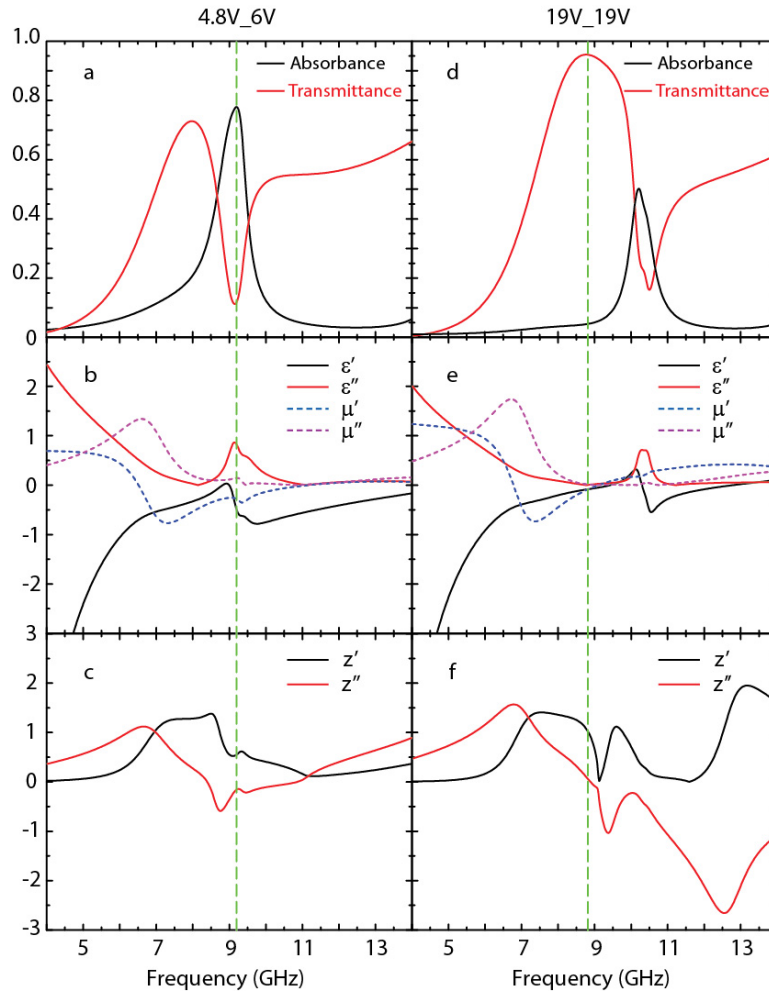


**Figure E-7. Simulations of 2 two-states “ART” tunable metasurface.** (a) AT switch with high absorbance with  $V_1 = 4.8$  V and  $V_2 = 6$  V. (b), (c)  $\epsilon$ ,  $\mu$  and  $z$  of the metasurface at the high absorbance state. (d) AT switch with high transmittance with  $V_1 = 19$  V and  $V_2 = 19$  V. (e), (f)  $\epsilon$ ,  $\mu$  and  $z$  of the metasurface at the high transmittance state.

#### **E.4 Conclusion**

In conclusion, we have designed and experimentally characterized a tunable metasurface tuned by varactor diodes. By changing the capacitance of the varactor diodes, we can change the impedance at one unique frequency and thus modify the absorption, reflection and transmission spectra of the metasurface. We achieved a 3-state (high absorbance, reflectance and transmittance) tunable metasurface which shows all wave-matter interactions in one device at X-band (8 to 14 GHz). The results expand the flexibility of tunable MMs and suggest a new way to achieve spatial light modulation in microwave.

## References:

- [1] S. R. Bowman, W. S. Rabinovich, C. S. Kyono, D. S. Katzer, K. IkossiAnastasiou, Highresolution spatial light modulators using GaAs/AlGaAs multiple quantum wells, *Appl. Phys. Lett.* **65**, 956 (1994).
- [2] M. Choi, J. Choi, Universal phase-only spatial light modulators, *Optics Express*, **25**, 22253 (2017).
- [3] N. Savage, Digital spatial light modulators, *Nature Photonics* **3**, 170 (2009).
- [4] C. Y. Lin, J. H. Chieh, Y. Luo, Multi-focal imaging system by using a programmable spatial light modulator, *Biomedical Imaging and Sensing Conference*, 107111P (2018).
- [5] D. R. Smith, W. J. Padilla, D. C. Vier, S. C. Nemat-Nasser, S. Schultz, Composite medium with simultaneously negative permeability and permittivity, *Phys. Rev. Lett.* **84**, 4184 (2000).
- [6] D. R. Smith, J. B. Pendry, M. C. K. Wiltshire, Metamaterials and Negative Refractive Index, *Science* **305**, 788 (2004).
- [7] P. Alitalo, S. Tretyakov, Electromagnetic cloaking with metamaterials, *Materials Today* **12**, 22 (2009).
- [8] X. Liu, T. Starr, A. F. Starr, W. J. Padilla, Infrared spatial and frequency selective metamaterial with near-unity absorbance, *Phys. Rev. Lett.* **104**, 207403 (2010).
- [9] S. Sun, Q. He, S. Xiao, Q. Xu, X. Li, L. Zhou, Gradient-index meta-surfaces as a bridge linking propagating waves and surface waves, *Nature Materials* **11**, 426 (2012).
- [10] J. Zhao, Q. Cheng, J. Chen, M. Q. Qi, W. X. Jiang, T. Cui, A tunable metamaterial absorber using varactor diodes, *New Journal of Physics* **15**, 043049 (2013).
- [11] F. Zhang, Q. Zhao, W. Zhang, J. Sun, J. Zhou, Voltage tunable short wire-pair type of metamaterial infiltrated by nematic liquid crystal, *Appl. Phys. Lett.* **97**, 134103 (2010).
- [12] P. P. Iyer, N. A. Butakov, J. A. Schuller, Reconfigurable semiconductor phased-array metasurfaces, *ACS Photonics* **2**, 1077 (2015).
- [13] T. T. Lv, Y. X. Li, H. F. Ma, Z. Zhu, Z. P. Li, C. Y. Guan, J. H. Shi, H. Zhang, T. J. Cui, Hybrid metamaterial switching for manipulating chirality based on VO<sub>2</sub> phase transition, *Scientific Reports* **6**, 23186 (2016).
- [14] A. Q. Liu, W. M. Zhu, D. P. Tsai, N. I. Zheludev, Micromachined tunable metamaterials: a Review, *J. Opt.* **14**, 114009 (2012).
- [15] S.A. Kosmopoulos, W.J.R. Hoefler, A. Gagnon, Non-linear tlm modeling of high-frequency varactor multipliers and halvers, *Int. J. Infrared Milli.*, **10**, 343 (1988).
- [16] D. R. Smith, D. C. Vier, Th. Koschny, C. M. Soukoulis, Electromagnetic parameter retrieval from inhomogeneous metamaterials, *Phys. Rev. E*, **71**, 036617 (2005).
- [17] D. R. Smith, Analytic expressions for the constitutive parameters of magnetoelectric metamaterials, *Phys. Rev. E*, **81**, 036605 (2010).
- [18] R. Liu, T. Cui, D. Huang, B. Zhao, D. R. Smith, Description and explanation of electromagnetic behaviors in artificial metamaterials based on effective medium theory, *Phys. Rev. E*, **76**, 026606 (2007).
- [19] J. B. Pendry, A. J. Holden, D. J. Robbins, W. J. Stewart, Magnetism from conductors and enhanced nonlinear phenomena, *IEEE Trans. Microwave Theory Tech.* **47**, 2075 (1999).

### List of publications:

9. J. Kong, X. Wu, X. Wang, M. J. Naughton, K. Kempa, “Plasmonic multiple exciton generation” arXiv:1806.10259 (2018).
8. X. Wu, J. Kong, D. Broido, and K. Kempa, “Tailoring the electron-phonon interaction with metallic plasmonic structures” Under review in *Materials Today Physics* (2018).
7. X. Wu, F. Ye, J. M. Merlo, M. J. Naughton, and K. Kempa, “Topologically Protected Photonic Edge States in the Visible in Plasmo-Gyroelectric Metamaterials,” *Advanced Optical Materials* **6**, 1800119 (2018); DOI: 10.1002/adom.201800119.
6. X. Wu, M.J. Naughton, and K. Kempa, “Engineering Low-Frequency Dielectric Function with Metamaterial Plasmonic Structures,” *physica status solidi rrl* **12**, 1700291 (2018); DOI: 10.1002/pssr.201700291.
5. R. Li, Q. Peng, B. Han, Y. Ke, X. Wang, X. Lu, X. Wu, J. Kong, Z. Ren, E. Akinoglu, M. Giersig, G. Zhou, J. Liu, K. Kempa, and J. Gao, “Plasmonic refraction-induced ultrahigh transparency of highly conducting metallic networks,” *Laser & Photonics Reviews* **3**, 465-472 (2016); DOI: 10.1002/lpor.201500271.
4. K. Fan, J. Suen, X. Wu and Willie J. Padilla, “Graphene metamaterial modulator for free-space thermal radiation,” *Optics Express* **24**, 25189 (2016); DOI: 10.1364/OE.24.025189.
3. B. Han, Q. Peng, R. Li, Q. Rong, Y. Ding, E. M. Akinoglu, X. Wu, X. Wang, X. Lu, Q. Wang, G. Zhou, J. Liu, Z. Ren, M. Giersig, A. Herczynski, K. Kempa and J. Gao, “Optimization of hierarchical structure and nanoscale-enabled plasmonic refraction for window electrodes in photovoltaics,” *Nature Communications* **7**, 12825 (2016); DOI:10.1038/ncomms12825
2. J. Kong, A. H. Rose, C. Yang, X. Wu, J. M. Merlo, M. J. Burns, M. J. Naughton, and K. Kempa, “Hot electron plasmon-protected solar cell,” *Optics Express* **23**, 240893 (2015); DOI: 10.1364/OE.23.0A1087.
1. C. Shemelya, D. DeMeo, N. P. Latham, X. Wu, C. Bingham, W. Padilla, and T. E. Vandervelde, “Stable high temperature metamaterial emitters for thermophotovoltaic applications,” *Applied Physics Letters* **104**, 201113 (2014); DOI: 10.1063/1.4878849.